

Ab Initio Quantum Simulation in Solid State Chemistry

Roberto Dovesi,^{*} Bartolomeo Civalleri,^{*}
Roberto Orlando,[#] Carla Roetti,^{*} and
Victor R. Saunders^{*}

^{*}*Dipartimento di Chimica IFM, Università di Torino, Via Giuria 5, I-10125 Torino, Italy*

[#]*Dipartimento di Scienze e Tecnologie Avanzate, Università del Piemonte Orientale, Corso Borsalino 54, I-15100 Alessandria, Italy*

INTRODUCTION

Molecular quantum chemistry and quantum mechanical simulation of solids have followed substantially independent paths and strategies for many years, with almost no reciprocal influence. In the implementation of computational schemes and formalisms, they started from different elementary models: either the hydrogen or helium atom like, for example, the parameterization of a correlation functional based on accurate He atom calculations by Colle and Salvetti,¹ or the electron gas, which is the reference system of the local density approximation²⁻⁷ (LDA) to density functional theory (DFT). Moreover, if we compare the simplest *real* crystals, like lithium metal or sodium chloride, with the smallest molecule, H₂, the much greater complexity of the solid system is

sufficient to explain the long delay of about 20 years, or more, in the development of *ab initio* simulation strategies in the two directions.

Molecular quantum chemistry evolved to maturity in many respects in the early 1970s, where the *ab initio* calculation of the molecular *total energy* became the key to understanding the chemical behavior of molecules, within a well-established, proper methodology, including the use of Gaussian functions as a basis set,^{8,9} sophisticated approximations to the wave function,^{10–14} and analytical gradients for geometry optimization.^{15,16} Computer programs, such as IBMOL¹⁷ and GAUSSIAN70,¹⁸ were already available to the scientific community, at that time or even before, and many molecular properties could be predicted with excellent accuracy, although at the beginning severe limitations, involving the algorithm efficiency and scaling with the system size, restricted the applicability of *ab initio* quantum-chemical methods to small molecules with relatively poor basis sets.

The approach to solving problems in the solid state was completely different and coincided essentially with developments in solid state physics, which at the time focused on comprehending fundamental properties such as the band structure, the effective mass, the Fermi surface shape, and their relationship to the electrical behavior of materials or to the interpretation of excitation spectra. The popular textbooks by Bassani¹⁹ and Moruzzi et al.²⁰ document well the state-of-the-art in solid state simulation during that period. Computer programs were mainly based on semi-empirical methods using “muffin-tin” potentials and the analytical simplicity of plane-wave (PW) basis sets. In late 1970s, *ab initio* pseudopotentials (PP), determined with reference to atomic calculations with the same Hamiltonian (see, for example, references 21–24), replaced previous empirical and semi-empirical PPs. Regarding the Hamiltonian, in the same years, the popular $X\text{-}\alpha$ ²⁵ method was replaced by the parameter-free LDA.^{3–5,7} As a matter of fact, the combination PP-PW-LDA became, and remains, the most popular “recipe” for the calculation of the electronic structure of crystalline compounds, although other schemes were also largely adopted, such as Korringa–Kohn–Rostoker (KKR),^{26,27} orthogonalized plane waves (OPW),²⁸ augmented plane waves (APW),^{29,30} linearized augmented plane waves (LAPW),³¹ spherical cellular schemes,³² and diophantine integration schemes.³³

Conversely, structural and elastic properties of ionic and semi-ionic solids were studied successfully in a completely different context with semi-classical methods,³⁴ based on force-field model potentials.

Preliminary attempts at introducing the quantum-chemical viewpoint into solid state modeling date to the late 1960s through the generalization of the Hartree–Fock (HF) equations for crystalline systems with a local basis set.^{35–41} These were, however, in most cases, only formal equations or partial solutions to some of the many computational problems implicit in these equations. Only at the beginning of the 1970s were Ewema^{42,43} and collaborators able to run a fully *ab initio* all-electron calculation for a crystalline compound

in a local basis, with reasonably good results for binding energies and lattice parameters of diamond,⁴² boron nitride,⁴³ and a few other systems. Unfortunately, this research project was abandoned and the related experience was lost for a while. Reliable *ab initio* algorithms, capable of computing not only the band structure but also relatively accurate binding energies, equilibrium geometries, and elastic properties were implemented shortly before 1980. Most of them were based on LDA with PW combined with PP. CRYSTAL⁴⁴ was the only periodic *ab initio* all-electron program based on the HF Hamiltonian and the use of Gaussian functions at that time.

In all cases, the access to programs for solid state simulation was exclusive to the research groups developing them. For this reason and because of the differences in the computational programs and their implementation, a comparison of the methods by performance was difficult. CRYSTAL was the first periodic *ab initio* code to be distributed to the scientific community beginning in 1989.⁴⁵ Afterward, the evolution in the field was rapid, and now several *ab initio* codes are available to users (see Appendix 1 for a list of some of these codes, with short indication of their main features).

Nowadays, simulation of infinite systems relies on an ensemble of strategies and methods differing in many respects. By simply looking at the list of solid state programs reported in Appendix 1, one has an idea of the large variety of approaches available. Illustrating the features of the various codes, or their merits and limits, is not the aim of this chapter. Instead, we provide here only a brief summary of the main “ingredients” in the “recipe” of a code for solid state simulation that includes:

1. The model. Many different models can be proposed for the simulation of a single physical or chemical phenomenon. For example, a point defect in a crystalline system can be simulated either with a finite cluster with a defect at the center of the cluster and by assuming that the cluster is big enough and border effects are small, or with a periodic supercell approach, with the defects repeated periodically in such a way that the defect–defect interaction is small, if the supercell is big enough.
2. The Hamiltonian. Although most of the periodic calculations are performed with reference to DFT, the debate is still open about the most appropriate functional to use for different systems and properties, ranging from LDA (that is still popular in solid state physics) to various generalized gradient approximation (GGA) formulations and hybrid schemes like B3LYP. In a few cases, HF is still preferred.
3. The basis set. Codes based on plane waves, local functions, and mixed (local functions in atomic spheres, plane waves in the interstices) or numeric basis sets are available.
4. The overall computational scheme, in all its features, such as direct or reciprocal space representation, all-electron versus pseudo-potential

formulation, and analytical versus numerical calculation of matrix elements and relevant integrals.

A reader is probably interested in finding answers to the following questions: What additional basic information is needed for proper use of periodic codes by a scientist with a molecular quantum chemistry background? Are there features peculiar to the solid state, with no analogy to the gas phase? In this chapter, we shall provide answers to these questions as well as provide a tutorial for the nonspecialist wanting to learn about solid state calculations.

The solid under study with a periodic program is infinite and translation invariant; it is a perfect crystal. Despite that no real crystal is a perfect crystal, this model is suitable in most cases, and indeed, experimental evidence of crystal periodicity exists in x-ray, neutron, and electron diffraction patterns, which are hardly affected by the presence of the surface, unless the experiment is done in special conditions. Translation invariance has a series of interesting properties with important consequences on simplification of the problem and the implementation of efficient algorithms.

Even in those cases where the model of a perfect crystal appears as inappropriate does one try to simulate partially nonperiodic systems with some nearly equivalent, formally periodic structure, whenever possible, as happens in the descriptions of local defects with the supercell approximation (see the section on defects) or in the treatment of substitutionally disordered systems.^{46,47} Therefore, the use of a periodic program by a scientist requires basic knowledge of crystallography, such as the definitions of lattice, direct and reciprocal space, unit cell, Brillouin zone, and the main concepts of the solid state language. These ideas are described briefly in the next section. Other more specific points will be mentioned with almost no discussion, because comprehension of their details is beyond the scope of this chapter. For example, the evaluation of electrostatic interactions in a solid⁴⁸⁻⁵¹ is more complicated than would appear at first sight and it represents one of the more crucial aspects of the computational problem. The formulation of a convenient method to compute the electrostatic potential generated by a three-dimensional array of charge distributions^{41,52-55} required more than 50 years' work; coverage of this topic is thus ill-advised.

Apart from the methodological aspects, solid state systems possess many interesting properties that are immaterial for single molecules. In single molecules, point symmetry usually decreases as the size of the molecule increases. Molecules with more than, say, 20 atoms often lack symmetry. Crystalline systems, contrarily, usually maintain high point symmetry, even in the case of large unit cell systems, like zeolites and garnets.

Another important difference between nonamorphous solids and single molecules is anisotropy (different space directions are not equivalent). No anisotropic effect is observed in the gas phase with no applied field because of the averaging process caused by the random orientation of molecules. In contrast,

crystals are macroscopic objects that can be oriented with respect to a reference frame and their properties generally depend on orientation. All properties related to crystal anisotropy are then described by tensors of various rank. For example, the relationship between stress and strain (second-order tensors each) cannot be expressed with a single constant, but it can be expressed as a fourth-order tensor, whereas piezoelectricity is described by a third-order tensor. In most cases, the physical and technological interest in materials science is focused on the possibility of increasing or reducing anisotropy in materials.

Throughout this chapter, we will illustrate some of the possibilities offered by *ab initio* simulation in the area of solid state chemistry, physics, materials science, surface science, and catalysis. The examples are mainly focused on simple properties like energy and its derivatives, band structure, and charge density, to give the reader who is not acquainted with solid state simulation an introductory overview. For consistency of the data and their representations, all examples have been generated with the CRYSTAL code,⁵⁶ implemented by the present authors and collaborators. All cases reported here refer to the static limit, and temperature effects are not discussed. Temperature effects can be taken into account by calculating thermodynamic functions from the vibration spectrum following a methodology common to most molecular codes (see, for example, reference 57 for a recent review). Alternatively, in solid state physics, the Car–Parrinello⁵⁸ methodology is popular, because it is an efficient way of finding equilibrium electron and nuclear coordinates at once.

Many important and interesting systems and properties could not be considered in this presentation either for conciseness, as they would require some preliminary long explanation, or because they are not yet available in CRYSTAL, although they have been implemented in other codes. The calculation of NMR tensors,⁵⁹ Raman intensity tensors,⁶⁰ and electro-optic tensors⁶¹ are only a few examples from this long list of omissions.

Two relevant topics have been ignored completely in this short chapter: the treatment of electron correlation with more sophisticated methods than DFT (that remains unsatisfactory from many points of view) and the related subject of excited states. Wave function-based methods for the calculation of electron correlation, like the perturbative Møller–Plesset (MP) expansion or the coupled cluster approximation, have registered an impressive advancement in the molecular context. The computational cost increases with the molecular size (as the fifth power in the most favorable cases), especially for molecules with low symmetry. That increase was the main disadvantage of these electron correlation methods, and it limited their application to tiny molecules. This scaling problem has been improved dramatically by modern reformulation of the theory by localized molecular orbitals, and now a much more favorable scaling is possible with the appropriate approximations. Linear scaling with such low prefactors has been achieved^{62,63} with MP schemes that the

feasibility of this kind of calculation has been extended to molecules of medium and large size.

In principle, this electron correlation strategy is transferable from single molecules to solids, after the crystalline orbitals have been transformed to an equivalent set of well-localized functions (Wannier functions). Procedures for orbital localization have been proposed and implemented only recently,^{64,65} and the first MP2 calculations are becoming possible in the case of simple crystalline compounds.⁶⁶

Alternative strategies have also been proposed for estimating correlation energies, including quantum Monte Carlo methods (see reference 67 and references therein), MP2 schemes, either canonical^{68,69} or based on the Laplace transform algorithm,⁷⁰ and the molecular-like incremental method applied by Stoll.⁷¹⁻⁷⁵ However, none of these methods seems to have arrived at a sufficiently advanced stage of development to be of general use to the scientist at the moment.

Regarding excited states, time-dependent density functional theory⁷⁶⁻⁷⁸ (TDDFT) is considered a relatively accurate method (see, for example, reference 79) for the study of the low-lying excited states, with results by far superior to the simple virtual-occupied DFT energy difference. The most recent formulations of the GW formalism, originally proposed about 20 years ago,⁸⁰ seem to provide good band gaps, optical spectra, and electron-hole excitations⁸¹⁻⁸⁴ (the GW acronym arises from the name of the two matrices the method is based on: the Green function matrix, G, and the screened Coulomb matrix, W).

TRANSLATION INVARIANCE PROPERTIES IN A CRYSTAL

Because a crystal can be regarded as a huge molecule consisting of about as many as Avogadro's number of atoms or ions, calculation of the crystalline electronic structure and properties may appear as an unattainable problem. Fortunately, however, crystals exhibit a very important symmetry property: They are translation invariant by definition. In fact, a perfect crystal consists of a three-dimensional array of atoms, ions, or molecules, a few of which form a spatial pattern that is repeated identically throughout the crystal. Clever exploitation of this symmetry property makes the computational problem solvable, and the theory, on which the solution is based, is known as band theory. The application of band theory to the study of periodic systems requires the knowledge of a specific language and some understanding of the properties of translation symmetry. In this section, a few basic concepts of crystallography and band theory will be introduced with reference to some elementary definitions as well as the discussion of a few simple examples, which are aimed to show how band structure and properties originate and to provide a little

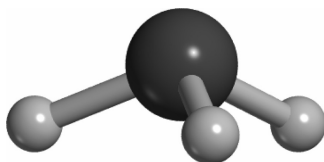


Figure 1 Ammonia molecule.

insight into the methods applied in the calculation of the electronic structure of matter in the condensed phase.

What is the main difference between studying the electronic structure of a molecule in the gas phase and in condensed phase? In the gas phase, because of the low density and large kinetic energies, molecules interact only during collisions, which may promote them to an excited state. However, either before or after such a brief collision, a molecule is essentially not influenced by the other molecules. Thus, as far as we are not interested in molecular dynamics and thermodynamic properties, the electronic structure in the ground or in any excited state can be studied for only one isolated molecule.

For example, if we are interested in studying ammonia in the gas phase, we can consider only one ammonia molecule, like in Figure 1. The positions of the nitrogen and hydrogen atoms, defined in the Cartesian coordinates or through a set of internal coordinates, are the only information necessary to compute the molecular wave function by *ab initio* methods.

On the contrary, at very high pressure or low temperature, ammonia molecules interact with each other and pack together to form a crystalline phase, known as phase I,⁸⁵ where the number of molecules involved is indeed large. Even the definition of the composition and geometry of a crystal is not as simple as for molecules. However, the arrangement of the molecules in a crystal must satisfy the condition of maximizing intermolecular attractive interactions, which imposes some severe constraints on their mutual orientations. In fact, observing an ammonia crystal carefully (Figure 2), it is possible to identify a set of four molecules that, when translated along each side of the cube by a multiple of the entire length, overlap with another set of four identical molecules exactly, because of translation invariance. Crystallography provides a mathematical description of this kind of object along with the tools for managing such complex systems.

The Direct Lattice

The crystallographer's view of a crystal⁸⁶ starts from the definition of a lattice: A *lattice* is a collection of points repeated at intervals of length a_1 , a_2 and a_3 along three non-coplanar directions, indefinitely. The three constants a_1 , a_2 , and a_3 are called *lattice parameters*, and the vectors \mathbf{a}_1 , \mathbf{a}_2 , and \mathbf{a}_3 , oriented in the same three non-coplanar directions with the lattice parameters

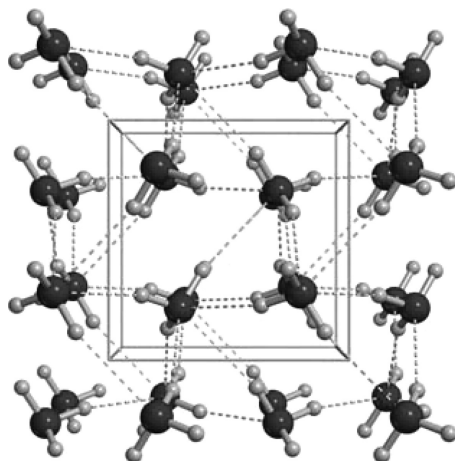


Figure 2 Crystal packing for phase I of solid ammonia.

as norms, are the *basis vectors*. Lattice parameters and angles between the lattice vectors are collectively called *cell parameters*.

A vector \mathbf{g} joining any two lattice points is a *lattice vector*. Every lattice vector can always be expressed by the basis vectors and three integer coefficients n_1 , n_2 , and n_3 :

$$\mathbf{g} = n_1\mathbf{a}_1 + n_2\mathbf{a}_2 + n_3\mathbf{a}_3 \quad [1]$$

Basis vectors \mathbf{a}_1 , \mathbf{a}_2 , and \mathbf{a}_3 define a parallelepiped called the *unit cell*, which is *primitive*, because it contains one lattice point. All cells that are obtained by translation of this unit cell, the origin cell, through the application of all vectors \mathbf{g} in Eq. [1], fill the space completely. Then, the entire lattice can be subdivided into cells and every vector \mathbf{g} can be used to label a cell with respect to the origin cell, or 0-cell. Actually, the definition of a unit cell is arbitrary, and many (an infinite number) different possible choices exist, because all cells containing the same number of lattice points are equivalent. The actual shape of a unit cell depends on the lattice type.

Primitive three-dimensional lattices have been classified into seven crystalline systems: *triclinic*, *monoclinic*, *orthorhombic*, *tetragonal*, *cubic*, *trigonal*, and *hexagonal*. They are different in the relative lengths of the basis vectors as well as in the angles they form. An additional seven nonprimitive lattices, belonging to the same crystalline systems, are added to the seven primitive lattices, which thus completes the set of all conceivable lattices in ordinary space. These 14 different types of lattices are known as Bravais lattices (Figure 3).

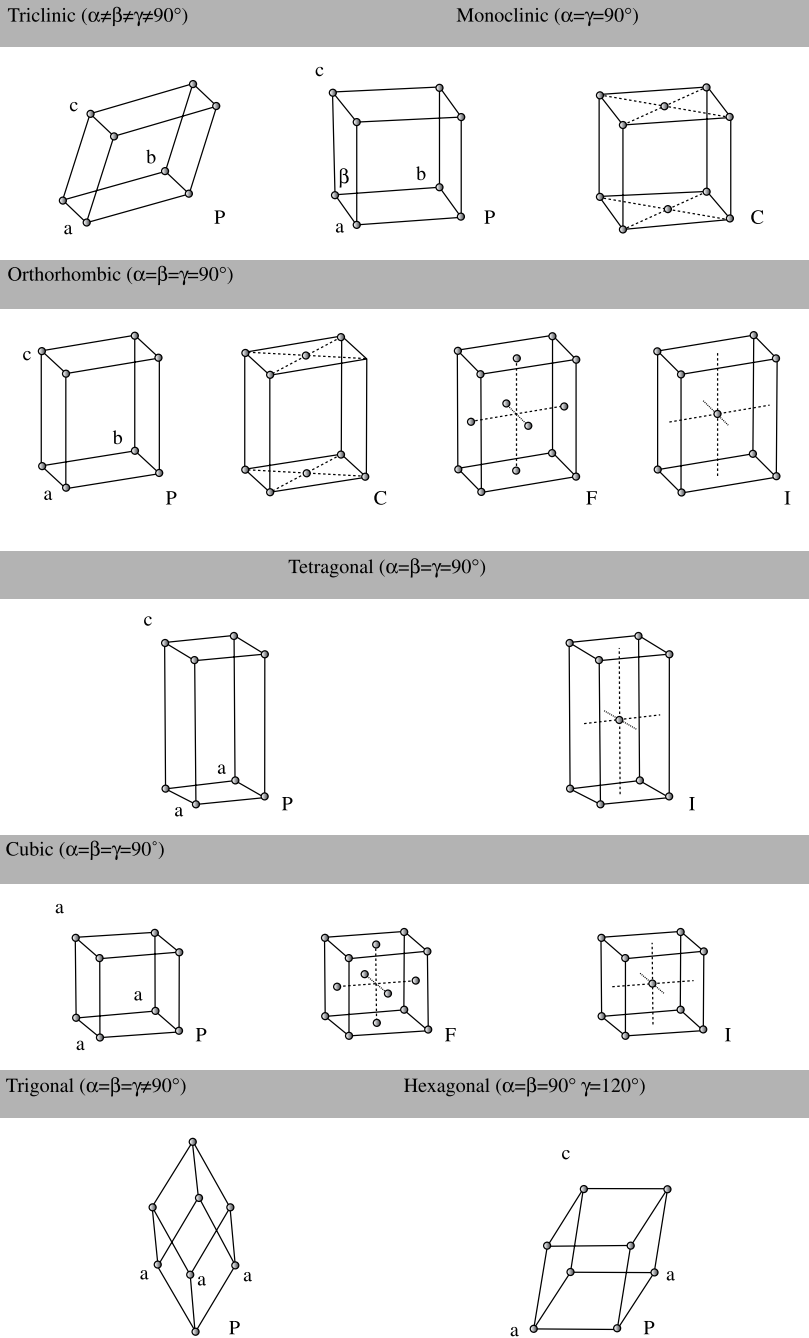


Figure 3 Bravais lattices. Symbols *P*, *F*, and *I* denote primitive, face-centered, and body-centered lattices, respectively. α , β , and γ are the angles between the **b** and **c**, **a** and **c**, and **a** and **b** basis vectors.

Filling the unit cell of a lattice with matter in a well-defined geometrical arrangement and applying the translation pattern permits the creation of an ideal crystal. Crystals usually exhibit point symmetry in addition to the set of translations. Point and translation symmetries combine to form a *space group*. It has been demonstrated that in ordinary space, only 230 of these different possible combinations exist and every space group refers to only one particular Bravais lattice. Space groups are fully characterized in the International Tables of Crystallography.⁸⁷ Every group is identified by a symbol (Hermann–Mauguin) that specifies it completely (the Schönflies notation, which is more frequently used for molecules, is also available, but it is less adequate to describe translational properties). Some points in the cell are invariant to one or more symmetry operations of the space group. In those cases, the number of symmetry equivalent points in a cell, or *multiplicity*, is smaller than the total number of symmetry operations. Such a point is called a *special position*, whereas every other point is referred to as a *general position*. The minimal set of atoms, either in special or general positions, which generates the complete unit cell after application of all space group symmetry operations, is referred to as the *asymmetric unit*. In summary, specifying the geometry of a crystal requires the following information:

- Space group
- Cell parameters
- Type and position of the atoms in the asymmetric unit

The position \mathbf{r} of an atom in the unit cell is usually not expressed in terms of Cartesian coordinates, but in terms of *fractional coordinates* x_1, x_2, x_3 such that

$$\mathbf{r} = x_1\mathbf{a}_1 + x_2\mathbf{a}_2 + x_3\mathbf{a}_3 \quad [2]$$

$x_1, x_2,$ and x_3 are pure numbers, as coefficients of the lattice basis vectors. Atoms with fractional coordinates all in the range between 0 and 1 belong to the 0-cell.

The parallelepiped in Figure 2 is the unit cell of the ammonia crystal phase I. Thus, the ammonia crystal can be regarded as the combination of a pattern of four ammonia molecules (16 atoms) in the unit cell with all possible translations in a cubic primitive lattice. Considerations about crystalline symmetry lead to the conclusion that ammonia in phase I crystallizes according to space group $P2_13$. Letter P in the symbol stands for primitive lattice, and the other symbols denote the main symmetry operations. The last element in the symbol, 3, indicates the presence of a three-fold axis not aligned with the principal rotation axis (if it was, it would follow letter P), which further indicates that the lattice is cubic. A cubic unit cell is completely specified by just one

lattice parameter, with the basis vectors all at right angles having the same norm. Because of the symmetry, only two atoms are in the asymmetric unit: one N and one H atom, so that only six fractional coordinates need to be specified. N is in a special position (along a three-fold axis) with multiplicity 4, whereas H is in a general position and has multiplicity 12, i.e., the number of point symmetry operations in the group.

When modeling a polymer or a surface, translation invariance is restricted to only one or two independent directions, instead of three. Space groups cannot characterize the symmetry of one-dimensional and two-dimensional periodic systems, and we need to refer to special subgroups of the space groups, the 75 *rod groups* and the 80 *layer groups*, respectively, which include the symmetry of all possible arrangements of three-dimensional objects (molecules or sets of atoms) in one-dimensional and two-dimensional lattices. Most of the considerations about the space groups are still valid for the rod and layer groups, with the exception of the classification of lattices, which is intimately related to the type of periodicity.

From here on, we will refer to ordinary space as the *direct space*, in order to contrast it to the *reciprocal space*, which is introduced in the next paragraph.

The Reciprocal Lattice

Every direct lattice admits a geometric construction, the *reciprocal lattice*, by the prescription that the reciprocal lattice basis vectors ($\mathbf{b}_1, \mathbf{b}_2, \mathbf{b}_3$) obey the following important orthogonality rules relative to the direct lattice basis vectors ($\mathbf{a}_1, \mathbf{a}_2, \mathbf{a}_3$):

$$\mathbf{a}_i \cdot \mathbf{b}_j = 2\pi \delta_{ij} \quad [3]$$

which implies that every reciprocal lattice basis vector (normalization to 2π) is orthogonal to the plane of the corresponding direct lattice basis vectors with unequal indices (δ_{ij} is 1 if i equals j and 0 when i is different from j).

Like in direct space, any reciprocal lattice vector can be expressed as a linear combination of the basis vectors with integer coefficients such as

$$\mathbf{K} = K_1\mathbf{b}_1 + K_2\mathbf{b}_2 + K_3\mathbf{b}_3 \quad [4]$$

Among all possible equivalent choices of a unit cell in the reciprocal lattice, one is particularly useful. It can be obtained by connecting one reciprocal lattice point to all its nearest neighbors and letting orthogonal planes pass through their midpoints. The volume within these planes is known as the *first Brillouin zone*. It includes all points that are closer to that reciprocal lattice point than to any other lattice point.

Bloch Theorem and the Periodic Boundary Conditions

A real crystal is a finite macroscopic object made of a finite, although extremely large, number of atoms. However, the ratio of the number of atoms at the surface to the total number of atoms in the crystal, N , is very small, and proportional to $N^{-1/3}$. When N is large and the surface is neutral, the perturbation caused by the presence of the boundary is limited to only a few surface layers and, therefore, has no influence on the bulk properties. For this reason, a macroscopic crystal mostly exhibits properties and features of the bulk material, and unless attention is deliberately focused onto the crystal boundary, surface effects can be thoroughly neglected. If this is the case, the crystallographic model of an infinite and translation-invariant crystal fits in the aim of studying bulk properties.

The potential energy of such a crystal must be a periodic function with the same periodicity as the lattice, so that for a translation by any direct lattice vector \mathbf{g} , the potential energy does not change

$$V(\mathbf{r} - \mathbf{g}) = V(\mathbf{r}) \quad [5]$$

Because of symmetry requirements, the Schrödinger equation

$$\hat{H}(\mathbf{r})\Psi(\mathbf{r}) = E\Psi(\mathbf{r}) \quad [6]$$

must also be translation invariant, which is equivalent to the requirement that, after a translation of the entire crystal by \mathbf{g} , the solutions of equation

$$\hat{H}(\mathbf{r} - \mathbf{g})\Psi(\mathbf{r} - \mathbf{g}) = E\Psi(\mathbf{r} - \mathbf{g}) \quad [7]$$

coincide with those of Eq. [6]. It has been demonstrated⁸⁸ that eigenfunctions with the correct symmetry relative to a potential of the form of Eq. [5] must obey the Bloch theorem, stating that

$$\Phi(\mathbf{r} + \mathbf{g}; \mathbf{k}) = e^{i\mathbf{k}\cdot\mathbf{g}} \Phi(\mathbf{r}; \mathbf{k}) \quad [8]$$

and providing a relation between the values of an eigenfunction at equivalent points in the lattice, which indicates that its periodicity is generally different from that of the lattice. As Φ verifies the Bloch theorem, it is called the *Bloch function* and is a function of the position in space \mathbf{r} and the *wave vector* \mathbf{k} . Parameter \mathbf{k} labels the different solutions to Eq. [6].

The equivalence of Eq. [6] and Eq. [7] can be verified easily, by supposing that the Bloch function $\Phi(\mathbf{r}; \mathbf{k})$ be an eigenfunction of the Hamiltonian in Eq. [6]. In this case, Eq. [7] can be rewritten as

$$\hat{H}(\mathbf{r} - \mathbf{g})\Phi(\mathbf{r} - \mathbf{g}; \mathbf{k}) = E(\mathbf{k})\Phi(\mathbf{r} - \mathbf{g}; \mathbf{k}) \quad [9]$$

However, by using the Bloch theorem and considering that $\hat{H}(\mathbf{r} - \mathbf{g})$ is equivalent to $\hat{H}(\mathbf{r})$ as an obvious consequence of the form of the crystalline potential (Eq. [5]), we obtain Eq. [6] again

$$\hat{H}(\mathbf{r})e^{-i\mathbf{k}\cdot\mathbf{g}}\Phi(\mathbf{r}; \mathbf{k}) = E(\mathbf{k})e^{-i\mathbf{k}\cdot\mathbf{g}}\Phi(\mathbf{r}; \mathbf{k}) \quad [10]$$

where $e^{-i\mathbf{k}\cdot\mathbf{g}}$ is simply a constant factor with unitary module (the eigenfunctions of an operator can always be multiplied by any arbitrary constant factor).

What is the form of Bloch functions? Equation [8] implies that a Bloch function can be written as the product of a plane wave and a periodic function $u(\mathbf{r}; \mathbf{k})$ with the same periodicity of the lattice:

$$\Phi(\mathbf{r}; \mathbf{k}) = e^{i\mathbf{k}\cdot\mathbf{r}} u(\mathbf{r}; \mathbf{k}) \quad [11]$$

In fact, Eq. [8] is immediately verified in this case:

$$\Phi(\mathbf{r} + \mathbf{g}; \mathbf{k}) = e^{i\mathbf{k}\cdot(\mathbf{r}+\mathbf{g})} u(\mathbf{r} + \mathbf{g}; \mathbf{k}) = e^{i\mathbf{k}\cdot\mathbf{g}} e^{i\mathbf{k}\cdot\mathbf{r}} u(\mathbf{r}; \mathbf{k}) = e^{i\mathbf{k}\cdot\mathbf{g}} \Phi(\mathbf{r}; \mathbf{k}) \quad [12]$$

Bloch functions span an infinite crystal and do not decay to zero at infinity. To circumvent the problem of normalizing a wave function with infinite extent, it is easier to consider a finite crystal consisting of $N = N_1 \times N_2 \times N_3$ cells and then let N grow to infinity. To preserve periodicity, *periodic boundary conditions* are imposed, which can be stated in the following form: If N_j cells exist along the j -th direction ($j = 1, 2, 3$) in the macroscopic crystal, it must happen that for any integer m and every j

$$\Phi(\mathbf{r} + m N_j \mathbf{a}_j; \mathbf{k}) = \Phi(\mathbf{r}; \mathbf{k}) \quad [13]$$

as if the crystal was a three-dimensional infinite array of identical and contiguous finite crystals with the shape of a parallelepiped, each consisting of N primitive cells. However, according to the Bloch theorem (Eq. [8])

$$\Phi(\mathbf{r} + m N_j \mathbf{a}_j; \mathbf{k}) = e^{im N_j \mathbf{k} \cdot \mathbf{a}_j} \Phi(\mathbf{r}; \mathbf{k}) \quad [14]$$

and, on comparing these two expressions, it is evident that the phase factor must be equal to one

$$e^{im N_j \mathbf{k} \cdot \mathbf{a}_j} = e^{im N_j \mathbf{k}_j \cdot \mathbf{a}_j} = 1 \quad [15]$$

But, if the component \mathbf{k}_j of the wave vector is defined as

$$\mathbf{k}_j = \frac{n_j}{N_j} \mathbf{b}_j \quad [16]$$

with n_j being an integer, by Eq. [3], \mathbf{k} can be interpreted as a point in the reciprocal lattice. Therefore, N of \mathbf{k} points exist in every reciprocal lattice cell, each of which can be written by the reciprocal lattice basis vectors as

$$\mathbf{k} = \left(\frac{n_1}{N_1} \mathbf{b}_1 + \frac{n_2}{N_2} \mathbf{b}_2 + \frac{n_3}{N_3} \mathbf{b}_3 \right) \quad [17]$$

If n_j is such that $\phi \leq n_j < N_j$ for every j \mathbf{k} belongs to the origin cell of the reciprocal lattice.

When N_1, N_2, N_3 are allowed to approach infinity, the number of \mathbf{k} points in every reciprocal lattice cell also tends to infinity until they completely fill the space, so that \mathbf{k} can be considered as a continuous variable.

Bloch functions also have interesting translational properties in the reciprocal space, which can be investigated by considering a new point $\mathbf{h} = \mathbf{k} + \mathbf{K}$, obtained by a translation of the wave vector \mathbf{k} by any reciprocal lattice vector \mathbf{K} (Eq. [4]), and then applying Eq. [8] to the corresponding Bloch function $\Phi(\mathbf{r}; \mathbf{h})$. By comparison with Eq. [8] and with Eq. [3], it is evident that $\Phi(\mathbf{r}; \mathbf{h})$ exhibits the same translational properties as $\Phi(\mathbf{r}; \mathbf{k})$

$$\Phi(\mathbf{r} + \mathbf{g}; \mathbf{h}) = e^{i(\mathbf{k} + \mathbf{K}) \cdot \mathbf{g}} \Phi(\mathbf{r}; \mathbf{k} + \mathbf{K}) = e^{i\mathbf{k} \cdot \mathbf{g}} \Phi(\mathbf{r}; \mathbf{h}) \quad [18]$$

so that both $\Phi(\mathbf{r}; \mathbf{h})$ and $\Phi(\mathbf{r}; \mathbf{k})$ can be referred to the same \mathbf{k} and are acceptable eigenfunctions for that \mathbf{k} in Eq. [6]. This behavior of Bloch functions in reciprocal space has the important consequence that the analysis can be restricted to the first Brillouin zone.

Another very important property of Bloch functions is related to the evaluation of the following integral extended to the entire space, which involves a function $f(\mathbf{r})$ with the same periodicity of the lattice:

$$f(\mathbf{k}, \mathbf{k}') = \int [\Phi(\mathbf{r}; \mathbf{k}')]^* f(\mathbf{r}) \Phi(\mathbf{r}; \mathbf{k}) d\mathbf{r} \quad [19]$$

with \mathbf{k} and \mathbf{k}' being points in the first Brillouin zone. In accordance with the property of Bloch functions in the reciprocal space just shown, the periodic component of a Bloch function referred to as \mathbf{k} (Eq. [11]) can be expanded into a linear combination of those plane waves for which the wave vector is obtained by addition of all reciprocal lattice vectors to the corresponding \mathbf{k} :

$$\begin{aligned} u(\mathbf{r}; \mathbf{k}) &= \sum_{\mathbf{K}} c_{\mathbf{K}} e^{i(\mathbf{k} + \mathbf{K}) \cdot \mathbf{r}} \\ u(\mathbf{r}; \mathbf{k}') &= \sum_{\mathbf{K}'} c_{\mathbf{K}'} e^{i(\mathbf{k}' + \mathbf{K}') \cdot \mathbf{r}} \end{aligned} \quad [20]$$

where $c_{\mathbf{K}}$ and $c_{\mathbf{K}'}$ are the expansion coefficients. Similarly, also $f(\mathbf{r})$, having the same periodicity as $u(\mathbf{r}; \mathbf{k})$ and $u(\mathbf{r}; \mathbf{k}')$, can be expanded in terms of plane waves, with $\mathbf{k} = 0$

$$f(\mathbf{r}) = \sum_{\mathbf{K}''} d_{\mathbf{K}''} e^{i\mathbf{K}'' \cdot \mathbf{r}} \tag{21}$$

Now the integral can be calculated through the evaluation of the following three infinite sums of integrals involving plane waves only:

$$f(\mathbf{k}, \mathbf{k}') = \sum_{\mathbf{K}} c_{\mathbf{K}} \sum_{\mathbf{K}'} c_{\mathbf{K}'} \sum_{\mathbf{K}''} d_{\mathbf{K}''} \int e^{i(\mathbf{k} + \mathbf{K} + \mathbf{K}'') \cdot \mathbf{r}} e^{i(\mathbf{k}' + \mathbf{K}') \cdot \mathbf{r}} d\mathbf{r} \tag{22}$$

and for the orthogonality of plane waves, these terms are zero unless $\mathbf{k} + \mathbf{K} + \mathbf{K}'' = \mathbf{k}' + \mathbf{K}'$. By Eq. [4] and Eq. [17], it is clear that this condition is fulfilled only if $\mathbf{k} = \mathbf{k}'$.

All integrals that need to be calculated in Eq. [6] are of this kind, as the potential energy term is a periodic function of the lattice, like $f(\mathbf{r})$, and the kinetic energy term involves second derivatives of $u(\mathbf{r}; \mathbf{k})$ with respect to \mathbf{r} , which have the same periodicity as $u(\mathbf{r}; \mathbf{k})$.

We could also arrive at the same conclusion in a different way by observing that Bloch functions are the eigenfunctions of translation operators and of all operators commuting with translation operators, like the Hamiltonian for a periodic system. Then, Bloch functions are bases for the irreducible representations for the group of the lattice translations, each one corresponding to one wave vector \mathbf{k} , and it is known from group theory that basis functions belonging to different irreducible representations are mutually orthogonal.

Therefore, great advantage exists in representing the Hamiltonian of a periodic system, where the potential energy operator has the form of Eq. [5], in Bloch functions. In fact, in this basis, the Hamiltonian matrix is block-diagonal (Figure 4), with each block referring to one particular point \mathbf{k} in the reciprocal space.

Suppose we have a finite basis set of n_f Bloch functions. The Hamiltonian matrix represented in this basis, then, consists of diagonal blocks of

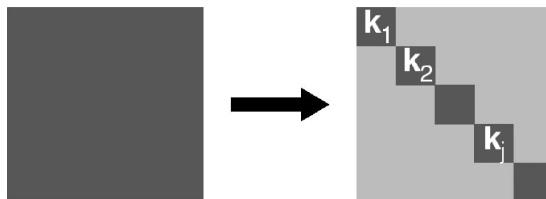


Figure 4 Transformation of the infinite Hamiltonian matrix when expressed in the basis of Bloch functions.

$n_f \times n_f$ elements, with each block referring to an individual \mathbf{k} point and being completely independent of all the others, such that the elements of a block do not interact with those of others blocks and can, therefore, be treated separately. Unfortunately, an infinite number of such factorized finite-sized blocks exists. In other words, Bloch functions as a basis set allows us to transform a problem of infinite size into an infinite number of problems of finite size. Nevertheless, what may appear as a poor advantage actually represents a great improvement, owing to the usually smooth change of the eigenvalues and the eigenvectors with \mathbf{k} . Therefore, it is generally possible to sample matrix \mathbf{H} at a finite number of points and solve the Schrödinger equation for a periodic system at different points in the first Brillouin zone:

$$\hat{H} \Psi_n(\mathbf{r}; \mathbf{k}) = E_n(\mathbf{k}) \Psi_n(\mathbf{r}; \mathbf{k}) \quad [23]$$

If sampling is convenient, the number of \mathbf{k} points to be considered is usually relatively small and solving the Schrödinger equation in the reciprocal space is a feasible method.

One-Electron Electrostatic Hamiltonian

If \hat{H} is the one-electron electrostatic Hamiltonian, based on the Born-Oppenheimer approximation, the solutions to Eq. [23] are called crystalline orbitals (CO). They are linear combinations of one-electron Bloch functions (Eq. [8])

$$\Psi_n(\mathbf{r}; \mathbf{k}) = \sum_j c_{jn}(\mathbf{k}) \Phi_j(\mathbf{r}; \mathbf{k}) \quad [24]$$

with coefficients c_{jn} to be determined. In the basis of Bloch functions, Eq. [23] can be written in the form of a matrix equation:

$$\mathbf{H}(\mathbf{k}) \mathbf{C}(\mathbf{k}) = \mathbf{S}(\mathbf{k}) \mathbf{C}(\mathbf{k}) \mathbf{E}(\mathbf{k}) \quad [25]$$

where the size of all matrices is equal to the number of Bloch functions in the basis and $\mathbf{S}(\mathbf{k})$ is the overlap matrix, which accounts for nonorthogonal basis sets. $\mathbf{C}(\mathbf{k})$, the matrix of coefficients, is constrained by the following orthonormalization condition (\mathbf{I} is the identity matrix):

$$\mathbf{C}(\mathbf{k}) \mathbf{S}(\mathbf{k}) \mathbf{C}^\dagger(\mathbf{k}) = \mathbf{I} \quad [26]$$

Atomic orbitals (AO) and plane waves are common choices to represent Bloch functions. Both choices would be equivalent, in principle, if an infinite basis set was considered, but they are not equivalent in the practical case of a finite

basis set. The use of AOs is better linked to the chemical experience of molecular codes and is particularly suitable to the description of crystals with chemical bonds. On the contrary, the description of free or nearly free electrons in conductors is hard to achieve in local functions and the addition of new functions to the AO basis set rapidly leads to saturation, which causes numerical instability because of quasi-linear dependence problems. Plane waves are more suitable to the case of metals and, in general, to the description of delocalized electrons. Another advantage of using plane waves is that the mathematics involved in the use of plane waves is usually much easier.

Any method of solution of Eq. [25] is specific of the kind of basis set used. In the remaining part of this chapter, we will always refer to the use of one-electron local basis sets within the linear combination of atomic orbitals (LCAO) method. Accordingly, n_f AOs in the 0-cell are chosen and replicated in the other cells of the crystal to form the periodic component $u(\mathbf{r}; \mathbf{k})$ of n_f Bloch functions. In particular, by denoting the μ -th AO, with the origin at \mathbf{r}_μ in the 0-cell, as $\chi_\mu(\mathbf{r} - \mathbf{r}_\mu)$ and the corresponding AO in a different cell, the \mathbf{g} -cell, as $\chi_\mu(\mathbf{r} - \mathbf{r}_\mu - \mathbf{g})$ or, equivalently, $\chi_\mu^{\mathbf{g}}(\mathbf{r} - \mathbf{r}_\mu)$, the expression used for $u_\mu(\mathbf{r}; \mathbf{k})$ consists of a linear combination of the equivalent AOs in all N cells of the crystal:

$$u_\mu(\mathbf{r}; \mathbf{k}) = \frac{1}{\sqrt{N}} e^{-i\mathbf{k}\cdot\mathbf{r}} \sum_{\mathbf{g}} e^{i\mathbf{k}\cdot\mathbf{g}} \chi_\mu^{\mathbf{g}}(\mathbf{r} - \mathbf{r}_\mu) \quad [27]$$

The translation invariance of $u_\mu(\mathbf{r}; \mathbf{k})$ is obvious because the sum is extended to all cells in the crystal. In fact, if a translation by lattice vector \mathbf{l} is applied

$$\begin{aligned} u_\mu(\mathbf{r} - \mathbf{l}; \mathbf{k}) &= \frac{1}{\sqrt{N}} e^{-i\mathbf{k}\cdot\mathbf{r}} \sum_{\mathbf{g}} e^{i\mathbf{k}\cdot(\mathbf{g}+\mathbf{l})} \chi_\mu^{\mathbf{g}+\mathbf{l}}(\mathbf{r} - \mathbf{r}_\mu) = \frac{1}{\sqrt{N}} e^{-i\mathbf{k}\cdot\mathbf{r}} \sum_{\mathbf{m}} e^{i\mathbf{k}\cdot\mathbf{m}} \chi_\mu^{\mathbf{m}}(\mathbf{r} - \mathbf{r}_\mu) \\ &= u_\mu(\mathbf{r}; \mathbf{k}) \end{aligned} \quad [28]$$

$u_\mu(\mathbf{r}; \mathbf{k})$ is verified to be periodic throughout the direct lattice (the equivalence of the sum over lattice vectors $\mathbf{m} = \mathbf{g} + \mathbf{l}$ and the sum over \mathbf{g} originates from translation invariance and the periodic boundary conditions).

The corresponding Bloch function is immediately obtained from Eq. [11] after substitution of $u_\mu(\mathbf{r}; \mathbf{k})$:

$$\Phi_\mu(\mathbf{r}; \mathbf{k}) = \frac{1}{\sqrt{N}} \sum_{\mathbf{g}} e^{i\mathbf{k}\cdot\mathbf{g}} \chi_\mu^{\mathbf{g}}(\mathbf{r} - \mathbf{r}_\mu) \quad [29]$$

Apart from a few starting elementary examples, all results that will be presented in this chapter have been obtained with the approximations presently available in the CRYSTAL code.⁵⁶ The method⁸⁹ of solving the Schrödinger

equation in CRYSTAL is similar in many respects to that used in molecular codes based on the usage of Gaussian basis sets. For example, finding Hartree–Fock eigenvalues and eigenvectors for a molecule requires the following steps:

1. Forming the basis of the AOs from contractions of Gaussian functions (linear combinations of a set of functions with constant coefficients) times angular functions followed by evaluating the overlap matrix S in this basis set.
2. Evaluating Fock matrix elements ($F_{\mu\nu}$) for all pairs of AOs in the local basis set, consisting of a sum of the following contributions: kinetic energy (T) terms, electron–nuclear (Z) interactions, and electron–electron Coulomb (C) and exchange (X) interactions

$$F_{\mu\nu} = T_{\mu\nu} + Z_{\mu\nu} + C_{\mu\nu} + X_{\mu\nu} \quad [30]$$

3. Solving Roothaan equations, $FC = SCE$, for E and C with the normalization condition

$$C^\dagger SC = I \quad [31]$$

4. Forming the density matrix from the eigenvectors of the occupied states with generic element

$$P_{\mu\nu} = \sum_n^{\text{occ.}} C_{\mu n}^* C_{\nu n} \quad [32]$$

5. Calculating the total energy according to the formula

$$E_t = N + \frac{1}{2} \sum_{\mu,\nu} P_{\mu\nu} (T_{\mu\nu} + Z_{\mu\nu} + F_{\mu\nu}) \quad [33]$$

which contains the internuclear repulsion energy N and a double sum over the AOs of one-electron terms.

Because the calculation of the electron–electron contributions to F in step 2 involves knowledge of the density matrix, the Roothaan equations are solved iteratively by repeating steps 2–4 to self-consistency.

It is now possible to compare the molecular scheme with the main steps of the CRYSTAL program:

1. Forming the basis of Bloch functions as linear combinations of the local basis of the AOs (Eq. [29]), in turn expressed as contractions of Gaussian

functions times angular functions, followed by evaluating the overlap matrix in the local basis set.

2. Evaluating Fock ($F_{\mu\nu}^g$) matrix elements in direct space in the local basis set; the average value of the Fock operator with respect to the AOs $\chi_\mu(\mathbf{r} - \mathbf{r}_\mu)$ in the 0-cell and $\chi_\nu^g(\mathbf{r} - \mathbf{r}_\nu)$ in the \mathbf{g} -cell is calculated as a sum of the following contributions:

$$F_{\mu\nu}^g = \langle \chi_\mu | \hat{F} | \chi_\nu^g \rangle = T_{\mu\nu}^g + Z_{\mu\nu}^g + C_{\mu\nu}^g + X_{\mu\nu}^g \quad [34]$$

Every matrix element is properly identified by the three indices μ , ν , and \mathbf{g} , which specify the two AOs and the direct lattice vector \mathbf{g} labeling the cell where the ν -th AO is centered because, in principle, the origin of $\chi_\nu^g(\mathbf{r} - \mathbf{r}_\nu)$ can be anywhere in the crystal. The possibility of always referring χ_μ to the 0-cell is because of translation invariance of the integrals in the local basis, for example:

$$\langle \chi_\mu^{g'} | \hat{F} | \chi_\nu^g \rangle = \langle \chi_\mu^0 | \hat{F} | \chi_\nu^{g-g'} \rangle = \langle \chi_\mu^0 | \hat{F} | \chi_\nu^m \rangle \quad [35]$$

with $\mathbf{m} = \mathbf{g} - \mathbf{g}'$ being a direct lattice vector.

3. Representing \mathbf{S} and \mathbf{F} matrices in the Bloch function basis set at every \mathbf{k} point of the sampling set. In this basis, the expression of the matrix elements contains a double sum over the direct lattice vectors. For example, a generic element of the Fock matrix represented in the reciprocal space is given by

$$F_{\mu\nu}(\mathbf{k}) = \langle \Phi_\mu(\mathbf{k}) | \hat{F} | \Phi_\nu(\mathbf{k}) \rangle = \frac{1}{N} \sum_{g'} \sum_g e^{i\mathbf{k} \cdot (\mathbf{g} - \mathbf{g}')} \langle \chi_\mu^{g'} | \hat{F} | \chi_\nu^g \rangle$$

Nevertheless, by taking Eq. [35] into account, the double sum reduces to N times a single sum and the expression can be simplified to

$$F_{\mu\nu}(\mathbf{k}) = \sum_{\mathbf{m}} e^{i\mathbf{k} \cdot \mathbf{m}} \langle \chi_\mu^0 | \hat{F} | \chi_\nu^m \rangle \quad [36]$$

This last equation can be interpreted as a Fourier transform of the Fock matrix from direct to reciprocal space.

4. Solving the Schrödinger equation with the orthonormality condition [26] at every \mathbf{k}

$$\mathbf{F}(\mathbf{k}) \mathbf{C}(\mathbf{k}) = \mathbf{S}(\mathbf{k}) \mathbf{C}(\mathbf{k}) \mathbf{E}(\mathbf{k}) \quad [37]$$

5. Determining the Fermi energy, E_F , which is the highest energy value of an occupied state in the system inside the first Brillouin zone.

6. Forming the density matrix \mathbf{P} and Fourier anti-transforming it to direct space

$$P_{\mu\nu}^{\mathbf{g}} = \frac{1}{V_{BZ}} \sum_n \int_{BZ} e^{i\mathbf{k}\cdot\mathbf{g}} C_{\mu n}^*(\mathbf{k}) C_{\nu n}(\mathbf{k}) \theta(E_F - E_n(\mathbf{k})) d\mathbf{k} \quad [38]$$

Here the sum over \mathbf{k} points has become an integral over the first Brillouin zone (with volume V_{BZ}), because it has already been shown that \mathbf{k} can be considered as a continuous variable. By limiting the integration to states with energy below E_F , a Heaviside step function θ permits us to exclude the eigenvectors relative to empty states from the sum. The reason why this cannot be achieved by simply truncating the sum over the eigenvectors, like in the molecular case, will be clear when the main features of band structure are illustrated later on in this chapter.

7. Calculating the total energy per cell as

$$E_t = N + \frac{1}{2} \sum_{\mu,\nu} \sum_{\mathbf{g}} P_{\mu\nu}^{\mathbf{g}} (T_{\mu\nu}^{\mathbf{g}} + Z_{\mu\nu}^{\mathbf{g}} + F_{\mu\nu}^{\mathbf{g}}) \quad [39]$$

The total energy of an infinite crystal is obviously infinite and has no physical meaning, but the total energy per cell, which includes the interaction of the nuclei and electrons in the 0-cell with all nuclei and electrons in the crystal, is finite. In this expression, a new sum over the infinite direct lattice vectors appears.

Again, steps 2–6 are iterated to self-consistency. Basically, two aspects are specific for the application of this method to solids: the calculation of matrices in direct space, which involve multiple sums over all the infinite direct lattice vectors, and the integration in reciprocal space. This latter aspect will be discussed with reference to a few specific examples in the next sections.

As an example of the problems involved in the evaluation of matrix elements for a periodic system, we consider the explicit form of the Coulomb electron–electron repulsion term in Eq. [34]

$$C_{\mu\nu}^{\mathbf{g}} = \sum_{\lambda} \sum_1 \sum_{\rho} \sum_{\mathbf{m}} P_{\lambda\rho}^{\mathbf{m}-1} \left\langle \chi_{\mu}^1 \chi_{\lambda}^1 \left| \frac{1}{r_{12}} \right| \chi_{\nu}^{\mathbf{g}} \chi_{\rho}^{\mathbf{m}} \right\rangle \quad [40]$$

where the three-index notation can be used for the density matrix elements, as a consequence of translation invariance, and χ_{μ}^1 and $\chi_{\nu}^{\mathbf{g}}$ in the two-electron integrals refer to electron 1, whereas χ_{λ}^1 and $\chi_{\rho}^{\mathbf{m}}$ refer to electron 2, with r_{12} being the mutual distance between electrons. The presence of the two infinite sums over the direct lattice vectors in Eq. [40] complicates the calculation of these terms dramatically. Thus, it is really the system size and the amount of

long-range interactions involved that make high accuracy and numerical stability important and more demanding targets than in molecular cases. Finding a solution to this problem has required a deep analysis of the convergence properties^{48-50,54,55} of the series to be evaluated. This analysis has resulted both in the formulation of convenient truncation criteria and in the application of Ewald's⁵² method to the calculation of long-range interactions in the slowly convergent Coulomb series. Fortunately, a local basis set is suitable to the definition of series truncation schemes, because an estimate of the importance of interparticle interactions is relatively easy in direct space.

DISCUSSION OF BAND STRUCTURE THROUGH A FEW SIMPLE EXAMPLES

A Monoatomic Linear Chain

The simplest case of a periodic model that one can imagine is a polymer with an atom per cell and one electron per atom, as depicted in Figure 5.

All atoms are equivalent by translation a . Although this is only a simplified ideal situation, it is used as a first example in many introductory textbooks on physical chemistry and solid state physics, because it is a problem simple enough to be treated analytically, especially if an easy approximation such as Hückel's model Hamiltonian is applied. Several important simplifications in Hückel's model make the calculation very easy, while preserving the main topological characteristics of the system. In this simple model, only one p_z AO is considered for each atom. The different orbitals will be identified by the \mathbf{g} lattice vector of the cell in which they are centered and denoted as $p_z^{\mathbf{g}}$. Hückel's approximation prescribes simple rules for the determination of the overlap and the Hamiltonian matrices with two parameters, α and β :

$$\langle p_z^{\mathbf{g}} | p_z^{\mathbf{l}} \rangle = \delta_{\mathbf{gl}} \quad \langle p_z^{\mathbf{g}} | \hat{H} | p_z^{\mathbf{l}} \rangle = \begin{cases} \alpha & \mathbf{g} = \mathbf{l} \\ \beta & |\mathbf{l} - \mathbf{g}| = a \\ 0 & |\mathbf{l} - \mathbf{g}| > a \end{cases} \quad [41]$$

Before evaluating $\mathbf{H}(\mathbf{k})$ and $\mathbf{S}(\mathbf{k})$ following Hückel's prescriptions, a basis set of Bloch functions must be defined in the local basis of the p_z AOs in the polymer

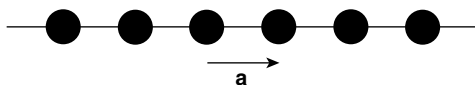


Figure 5 Schematic representation of a Bloch function for a monoatomic linear chain. A black circle represents a p_z AO.

according to Eq. [29]. However, this case is particularly simple, because there is only one atom in each cell and we are considering only one AO per atom (Figure 5). Therefore, only one Bloch function can be generated

$$\Phi(\mathbf{r}; \mathbf{k}) = \frac{1}{\sqrt{N}} \sum_{\mathbf{g}} e^{i\mathbf{k}\cdot\mathbf{g}} p_z^{\mathbf{g}}(\mathbf{r}) \quad [42]$$

and all matrices are one-dimensional, i.e., all terms in Eq. [25] are actually single-variable functions of \mathbf{k} .

Because the basis set is minimal (only one Bloch function per \mathbf{k} point), this Bloch function is itself an eigenfunction of the Hamiltonian. With this basis set, \mathbf{S} takes the form:

$$\mathbf{S}(\mathbf{k}) = \langle \Phi(\mathbf{k}) | \Phi(\mathbf{k}) \rangle = \frac{1}{N} \sum_{\mathbf{g}, \mathbf{l}} e^{i\mathbf{k}\cdot(\mathbf{l}-\mathbf{g})} \langle p_z^{\mathbf{g}} | p_z^{\mathbf{l}} \rangle \quad [43]$$

but, because of translation invariance, the overlap depends only on the distance between the AOs, so that any integral can be translated into the reference cell and any linear combination of lattice vectors is, again, a lattice vector, say $\mathbf{m} = \mathbf{l} - \mathbf{g}$. For these reasons, the double sum in the expression of $\mathbf{S}(\mathbf{k})$ reduces to N times a single sum (like in Eq. [36]), and on the basis of Hückel's rules, $\mathbf{S}(\mathbf{k})$ results to be constant in \mathbf{k}

$$\mathbf{S}(\mathbf{k}) = \frac{1}{N} \sum_{\mathbf{g}, \mathbf{l}} e^{i\mathbf{k}\cdot(\mathbf{l}-\mathbf{g})} \langle p_z^0 | p_z^{\mathbf{l}-\mathbf{g}} \rangle = \sum_{\mathbf{m}} e^{i\mathbf{k}\cdot\mathbf{m}} \langle p_z^0 | p_z^{\mathbf{m}} \rangle = \sum_{\mathbf{m}} e^{i\mathbf{k}\cdot\mathbf{m}} \delta_{\mathbf{m}0} = 1 \quad [44]$$

Function $\mathbf{H}(\mathbf{k})$ is obtained in a similar way

$$\begin{aligned} \mathbf{H}(\mathbf{k}) &= \langle \Phi(\mathbf{k}) | \hat{H} | \Phi(\mathbf{k}) \rangle = \frac{1}{N} \sum_{\mathbf{g}, \mathbf{l}} e^{i\mathbf{k}\cdot(\mathbf{l}-\mathbf{g})} \langle p_z^{\mathbf{g}} | \hat{H} | p_z^{\mathbf{l}} \rangle = \\ &= e^{i\mathbf{k}\cdot 0} \alpha + e^{i\mathbf{k}\cdot \mathbf{a}} \beta + e^{-i\mathbf{k}\cdot \mathbf{a}} \beta = \alpha + 2\beta \cos(ka) \end{aligned} \quad [45]$$

In this simple case, both $\mathbf{C}(\mathbf{k})$ and $\mathbf{S}(\mathbf{k})$ are constant and equal to 1; thus, the eigenvalue $\mathbf{E}(\mathbf{k})$ coincides with $\mathbf{H}(\mathbf{k})$. It is apparent that the eigenvalue spectrum of a periodic system like this polymer does not consist of discrete energy levels as occurring in the case of an atom or a molecule (it would consist of a single level for one atom of this polymer). Instead, the eigenvalue spectrum includes all possible energy values within a definite range (between $\alpha + 2\beta$ and $\alpha - 2\beta$), forming a band, as represented in Figure 6 (parameters α and β are both negative).

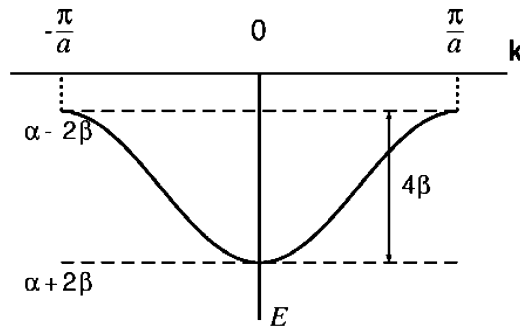


Figure 6 Hückel π -band of a monoatomic linear chain in the first Brillouin zone.

A Two-Dimensional Periodic Example: Graphite

As a second example, we consider graphite. Although graphite in a pencil consists of a large number of layers of the type represented in Figure 7, it is well known that we can use a pencil for writing or drawing because the inter-layer interactions are weak, much weaker than the intralayer interactions, and difficult to render computationally if we are not using sophisticated methods. For this reason, a single layer of graphite is a good model, which will be used in this example.

A layer of graphite can be considered as infinite and periodic in two dimensions. Graphite has a planar hexagonal structure. It belongs to a layer group that is derivable from the $P6/mmm$ space group, containing 24 symmetry operations.

The unit cell has the shape of a rhomb with angles of 60° and 120° (Figure 7). The point symmetry elements (six-fold axis normal to the plane, six two-fold rotation axes in the plane, six mirrors normal to the plane, and one in the plane, inversion) pass through the unit cell origin, at the center of the hexagons. There are two symmetry-related carbon atoms in the unit cell, labeled as A and B in Figures 7 and 9, with fractional coordinates $(1/3, 2/3)$ and

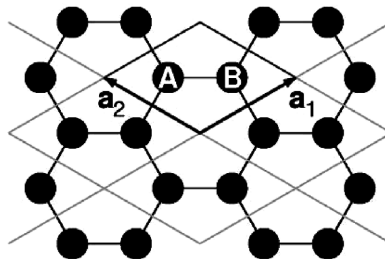


Figure 7 Graphite layer.

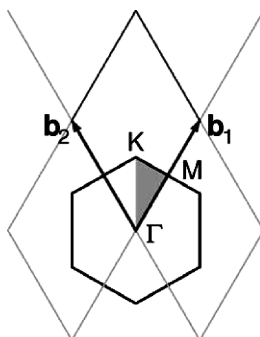
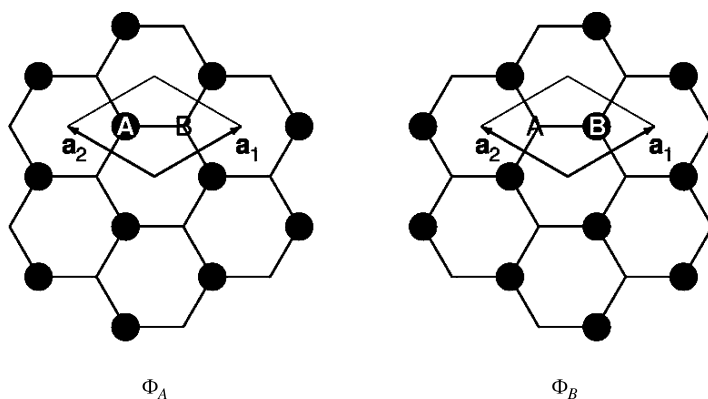


Figure 8 Graphite reciprocal lattice.

$(2/3, 1/3)$, respectively. Each atom of type A is surrounded by three atoms of type B, and vice versa.

The reciprocal lattice is again hexagonal, as an obvious consequence of the basis vectors \mathbf{b}_1 and \mathbf{b}_2 being orthogonal to \mathbf{a}_1 and \mathbf{a}_2 , according to Eq. [3]. The first Brillouin zone has the shape of a hexagon as in Figure 8, with its center at the lattice origin, where $\mathbf{k} = \mathbf{0}$. The shaded triangle in the picture represents the asymmetric unit in the Brillouin zone. Special symbols have been assigned to the points at the vertices of the triangle, which correspond to special positions in the reciprocal lattice. Denoting \mathbf{k} points by their components along \mathbf{b}_1 and \mathbf{b}_2 as (b_1, b_2) , M identifies the point at the top of the triangle with components $(\frac{1}{2}, 0)$, K denotes point $(1/3, 1/3)$, and Γ is the lattice origin $(0, 0)$. Actually, Γ identifies the origin in any reciprocal lattice.

Also in this case, π electron bands can be studied with Hückel's approximation by representing all matrices in a basis set of two Bloch functions from

Figure 9 Representation of Bloch functions for graphite. A circle represents a p_z AO.

p_{zA} and p_{zB} AOs according to Eq. [29]

$$\Phi_A(\mathbf{r}; \mathbf{k}) = \frac{1}{\sqrt{N}} \sum_{\mathbf{g}} e^{i\mathbf{k}\cdot\mathbf{g}} p_{zA}^{\mathbf{g}}(\mathbf{r}) \quad \Phi_B(\mathbf{r}; \mathbf{k}) = \frac{1}{\sqrt{N}} \sum_{\mathbf{g}} e^{i\mathbf{k}\cdot\mathbf{g}} p_{zB}^{\mathbf{g}}(\mathbf{r}) \quad [46]$$

At each \mathbf{k} point, \mathbf{H} , \mathbf{S} , \mathbf{C} , and \mathbf{E} in Eq. [25] are 2×2 matrices in the basis of Φ_A and Φ_B . Again, \mathbf{H} and \mathbf{S} must be computed to find the unknown matrices \mathbf{C} and \mathbf{E} . For symmetry reasons, only the asymmetric part of the Brillouin zone needs to be explored instead of the entire zone, and because the full representation of a π -type band structure for graphite would be three-dimensional, we can start by exploring a representative monodimensional path (as is usually done for three-dimensional structures). The most obvious choice is the triangle perimeter, and in particular, the special positions Γ , M , and K are expected to be topologically interesting for their symmetry properties.

During the calculation of \mathbf{S} and \mathbf{H} , it must be taken into account that, because of the symmetry equivalence of the carbon atoms, $S_{AA}(\mathbf{k}) = S_{BB}(\mathbf{k})$ and $H_{AA}(\mathbf{k}) = H_{BB}(\mathbf{k})$, whereas $H_{AB}(\mathbf{k}) = H_{BA}^{\dagger}(\mathbf{k})$ for hermiticity. Moreover, Hückel's rules imply that $\mathbf{S}(\mathbf{k})$ is the identity matrix of order 2, completely independent of \mathbf{k} . In fact, diagonal elements can be computed in exactly the same way as for the linear chain, even though the geometry is different in this case, and the off-diagonal elements are zero because of Hückel's orthogonality assumption. Consequently, Eq. [25] becomes

$$\mathbf{H}(\mathbf{k})\mathbf{C}(\mathbf{k}) = \mathbf{C}(\mathbf{k})\mathbf{E}(\mathbf{k}) \quad [47]$$

We start by computing matrix \mathbf{H} at Γ . This is a peculiar point because each of the two Bloch functions in Eq. [46] reduces to a simple sum of all AOs of that type (A or B) in the lattice (all factor phases are 1 when $\mathbf{k} = \mathbf{0}$).

H_{AA} can be calculated in a similar way as for the linear chain, because a carbon atom does not have any nearest neighbor of the same type, as can be easily seen in Figure 9. Applying Hückel's rules, we find:

$$\begin{aligned} H_{AA}(\mathbf{0}) &= \langle \Phi_A(\mathbf{0}) | \hat{H} | \Phi_A(\mathbf{0}) \rangle = \frac{1}{N} \sum_{\mathbf{g}, \mathbf{l}} \langle p_{zA}^{\mathbf{g}} | \hat{H} | p_{zA}^{\mathbf{l}} \rangle = \sum_{\mathbf{m}} \langle p_{zA}^{\mathbf{0}} | \hat{H} | p_{zA}^{\mathbf{m}} \rangle \\ &= \langle p_{zA}^{\mathbf{0}} | \hat{H} | p_{zA}^{\mathbf{0}} \rangle = \alpha \end{aligned} \quad [48]$$

This result is actually unrelated to the choice of Γ , but it comes from the fact that all three nearest neighbours of atom A are type-B atoms. Therefore, the same value of H_{AA} is to be expected at any \mathbf{k} point. For this reason, the calculation of this element will not be repeated in the following cases.

The value of $H_{AB}(\mathbf{0})$ is, again, determined by the number of neighboring atoms of carbon A. In fact, only the p_{zB} AOs in the $\mathbf{0}$, $-\mathbf{a}_1$, and \mathbf{a}_2 cells can

contribute a nonzero interaction with p_{zA} in the 0-cell:

$$H_{AB}(0) = \langle \Phi_A(0) | \hat{H} | \Phi_B(0) \rangle = \sum_{\mathbf{m}} \langle p_{zA}^0 | \hat{H} | p_{zB}^{\mathbf{m}} \rangle = 3\beta \quad [49]$$

Equation [25] at Γ can now be solved by imposing the condition that the following determinant annihilates:

$$|\mathbf{H}(0) - E^\Gamma \mathbf{I}| = \begin{vmatrix} \alpha - E^\Gamma & 3\beta \\ 3\beta & \alpha - E^\Gamma \end{vmatrix} = 0 \quad [50]$$

which implies that two possible energy values exist at Γ

$$E_{\pm}^\Gamma = \alpha \pm 3\beta \quad [51]$$

The corresponding eigenfunctions are obtained by replacing each of the two values of E^Γ in Eq. [47] in turn (E_+ and E_- to obtain Ψ_+ and Ψ_- , respectively) and imposing the normalization condition of

$$c_A^2 + c_B^2 = 1 \quad [52]$$

The solution of this two-equation system with two unknown coefficients is a fully constrained algebraic problem, which leads to a symmetric and an anti-symmetric linear combination of Bloch functions, as a consequence of the equivalence of carbon atoms of types A and B. These solutions correspond to π -bonding and π -antibonding COs having the following form:

$$\Psi_+^\Gamma(\mathbf{r}) = \frac{1}{\sqrt{2}} [\Phi_A(\mathbf{r}; \mathbf{0}) + \Phi_B(\mathbf{r}; \mathbf{0})] \quad \Psi_-^\Gamma(\mathbf{r}) = \frac{1}{\sqrt{2}} [\Phi_A(\mathbf{r}; \mathbf{0}) - \Phi_B(\mathbf{r}; \mathbf{0})] \quad [53]$$

which are represented schematically in Figure 10. The AOs in Ψ_+^Γ are all in phase and define a totally symmetric combination, which is known to correspond to the most stable state. Contrarily, the antibonding CO represents the most unstable state, where the number of nodal planes is maximum.

At point M, taking Eq. [3] into account, Bloch functions can be written as

$$\Phi_A(\mathbf{r}; \mathbf{M}) = \frac{1}{\sqrt{N}} \sum_{n_1, n_2} e^{i\mathbf{b}_1 \cdot (n_1 \mathbf{a}_1 + n_2 \mathbf{a}_2)} p_{zA}^{n_1 \mathbf{a}_1 + n_2 \mathbf{a}_2}(\mathbf{r}) = \frac{1}{\sqrt{N}} \sum_{n_1, n_2} e^{in_1 \pi} p_{zA}^{n_1 \mathbf{a}_1 + n_2 \mathbf{a}_2}(\mathbf{r}) \quad [54]$$

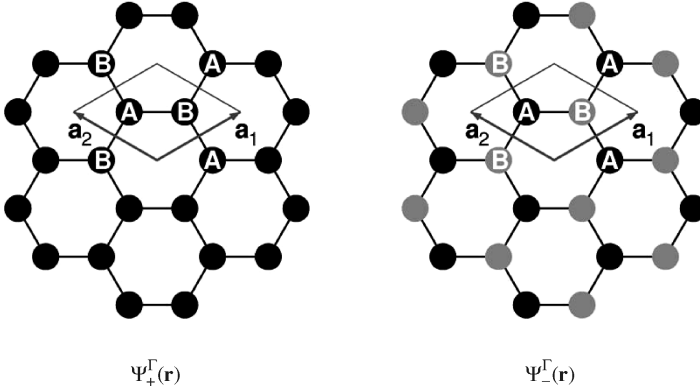


Figure 10 Representations of bonding $\Psi_+^\Gamma(\mathbf{r})$ and antibonding $\Psi_-^\Gamma(\mathbf{r})$ π -crystalline orbitals at Γ in graphite. Black and gray circles represent the positive and negative signs of each p_z AO in the linear combination, respectively.

Because n_1 and n_2 are integers, the phase factor can be evaluated straightforwardly, as

$$\Phi_A(\mathbf{r}; \mathbf{M}) = \frac{1}{\sqrt{N}} \sum_{n_1, n_2} (-1)^{n_1} p_{zA}^{n_1 \mathbf{a}_1 + n_2 \mathbf{a}_2}(\mathbf{r}) \quad [55]$$

and similarly for Φ_B . The form of Φ_A implies an inversion of the sign of the AOs at \mathbf{M} when n_1 is odd, so that the AOs change their signs every time n_1 is incremented by 1. This change corresponds to the alternation of the rows of the AOs with positive and negative signs along the direction of \mathbf{a}_1 , like a wave, as shown in the left picture in Figure 11, where Φ_A and Φ_B are combined in phase.

In this basis set and considering that two of the nearest neighbors of atom A (see Figure 11) are associated with a phase factor with the same sign, whereas the third nearest neighbor has opposite sign:

$$\begin{aligned} H_{AB}(\mathbf{M}) &= \langle \Phi_A(\mathbf{M}) | \hat{H} | \Phi_B(\mathbf{M}) \rangle = \sum_{m_1, m_2} (-1)^{m_1} \langle p_{zA}^0 | \hat{H} | p_{zB}^{m_1 \mathbf{a}_1 + m_2 \mathbf{a}_2} \rangle \\ &= (2 - 1)\beta = \beta \end{aligned} \quad [56]$$

In this case, the solution of Eq. [47] implies the fulfilment of the following condition:

$$\begin{vmatrix} \alpha - E^M & \beta \\ \beta & \alpha - E^M \end{vmatrix} = 0 \quad [57]$$

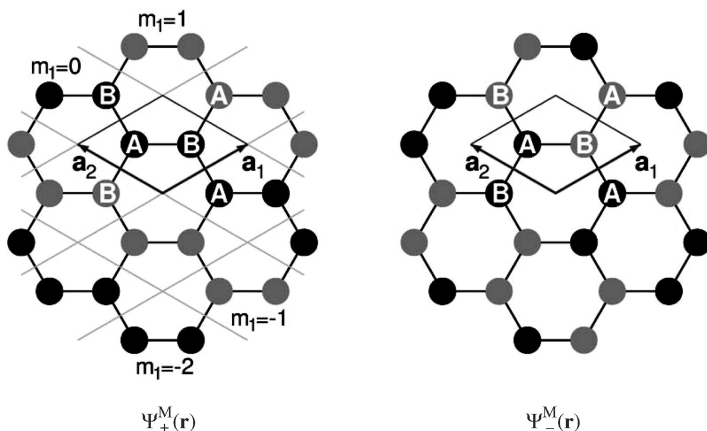


Figure 11 Representation of bonding and antibonding π -crystalline orbitals at M in graphite.

leading to the following eigenvalues at point M:

$$E_{\pm}^M = \alpha \pm \beta \quad [58]$$

The corresponding bonding and antibonding eigenfunctions are, again, a symmetric and an antisymmetric combination of Φ_A and Φ_B , depicted schematically in Figure 11. The in-phase interactions among AOs of chains along the direction of a_2 confer stability to the bonding CO, although not as large as the completely in-phase combination in Γ . Conversely, the antibonding CO is less destabilized at M than at Γ , which owes to one in-phase interaction between p_{zA} and p_{zB} in the former.

The third highly symmetric point is K. In this case

$$\begin{aligned} \Phi_A(\mathbf{r}; \mathbf{K}) &= \frac{1}{\sqrt{N}} \sum_{n_1, n_2} e^{i\frac{2\pi}{3}(\mathbf{b}_1 + \mathbf{b}_2) \cdot (n_1 \mathbf{a}_1 + n_2 \mathbf{a}_2)} p_{zA}^{n_1 \mathbf{a}_1 + n_2 \mathbf{a}_2}(\mathbf{r}) \\ &= \frac{1}{\sqrt{N}} \sum_{n_1} e^{i\frac{2\pi}{3}n_1(n_1 + n_2)} p_{zA}^{n_1 \mathbf{a}_1 + n_2 \mathbf{a}_2}(\mathbf{r}) \end{aligned} \quad [59]$$

The phase factor in this expression can only have three possible values, depending on the sum of the two integers n_1 and n_2 . In fact, for any integer m ,

$$e^{i\frac{2\pi}{3}(n_1 + n_2)} = \begin{cases} 1 & n_1 + n_2 = 3m \\ -\frac{1}{2} + i\frac{\sqrt{3}}{2} & n_1 + n_2 = 3m + 1 \\ -\frac{1}{2} - i\frac{\sqrt{3}}{2} & n_1 + n_2 = 3m + 2 \end{cases} \quad [60]$$

At point K, the Bloch function basis also contains an imaginary part, in addition to the real part, which is not the case at Γ or M. The evaluation of the H_{AB} interaction element of the Hamiltonian matrix leads to the following result:

$$\begin{aligned} H_{AB}(\mathbf{K}) &= \langle \Phi_A(\mathbf{K}) | \hat{H} | \Phi_B(\mathbf{K}) \rangle = \sum_{m_1, m_2} e^{i\frac{2\pi}{3}(m_1+m_2)} \langle p_{zA}^0 | \hat{H} | p_{zB}^{m_1\mathbf{a}_1+m_2\mathbf{a}_2} \rangle = \\ &= \left[-\frac{1}{2} - \frac{1}{2} + 1 + i \left(\frac{\sqrt{3}}{2} - \frac{\sqrt{3}}{2} \right) \right] \beta = 0 \end{aligned} \quad [61]$$

and the Hamiltonian is already in the diagonal form. The equation to be solved is

$$\begin{vmatrix} \alpha - E^K & 0 \\ 0 & \alpha - E^K \end{vmatrix} = 0 \quad [62]$$

Thus, clearly a degeneracy of the bonding and the antibonding states at K occurs

$$E_{\pm}^K = \alpha \quad [63]$$

The real and imaginary parts of the corresponding COs are represented in Figure 12.

So far, the energy of bonding and antibonding π -COs are degenerate at K and split at Γ and M, with the splitting being larger at Γ .

What happens at other points, for instance, at $\mathbf{k} = (\frac{1}{4}, 0)$, midway the Γ -M path? In this case, it is easily seen that

$$\Phi_A\left(\mathbf{r}; \frac{1}{4}\mathbf{b}_1\right) = \frac{1}{\sqrt{N}} \sum_{n_1, n_2} i^{n_1} p_{zA}^{n_1\mathbf{a}_1+n_2\mathbf{a}_2}(\mathbf{r}) \quad [64]$$

and

$$H_{AB}\left(\frac{1}{4}\mathbf{b}_1\right) = \sum_{m_1, m_2} i^{m_1} \langle p_{zA}^0 | \hat{H} | p_{zB}^{m_1\mathbf{a}_1+m_2\mathbf{a}_2} \rangle = (2 - i)\beta \quad [65]$$

The eigenvalues can then be found by solving the following equation:

$$\begin{vmatrix} \alpha - E^{(\frac{1}{4}, 0)} & (2 - i)\beta \\ (2 + i)\beta & \alpha - E^{(\frac{1}{4}, 0)} \end{vmatrix} = 0 \quad [66]$$

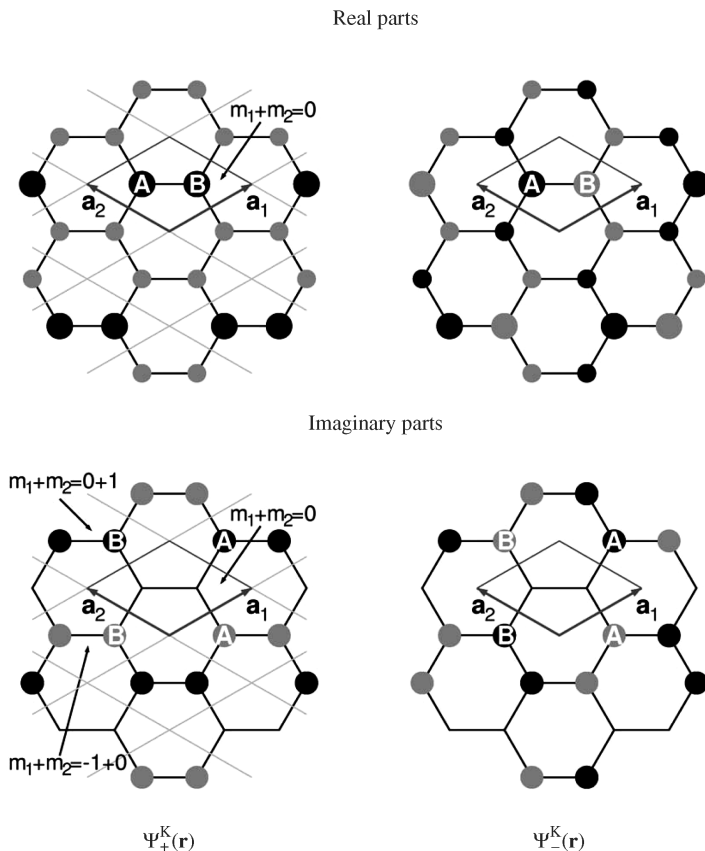


Figure 12 Representation of bonding and antibonding π -crystalline orbitals at K in graphite.

The two possible energy values at this point

$$E^{\left(\frac{\pi}{3}, 0\right)} = \alpha \pm \sqrt{5}\beta \quad [67]$$

are intermediate between the corresponding bonding and antibonding E^M and E^Γ , in fact $|\beta| < \sqrt{5}|\beta| < 3|\beta|$. The topology of the wave function at this point (see Figure 13) resembles that in M, with the main differences being that in this case, an imaginary component exists, as well, and that the period of the wave doubles, when \mathbf{k} is midway to the Γ -M path.

The values of E_\pm found at special \mathbf{k} points in the reciprocal lattice are actually special forms of a general expression for E_\pm , which is a simple function of $\mathbf{k} = k_1\mathbf{b}_1 + k_2\mathbf{b}_2$ also in this case:

$$E_\pm^{\mathbf{k}} = \alpha \pm \beta \sqrt{[1 + \cos(2k_1\pi) + \cos(2k_2\pi)]^2 + [\sin(2k_2\pi) - \sin(2k_1\pi)]^2} \quad [68]$$

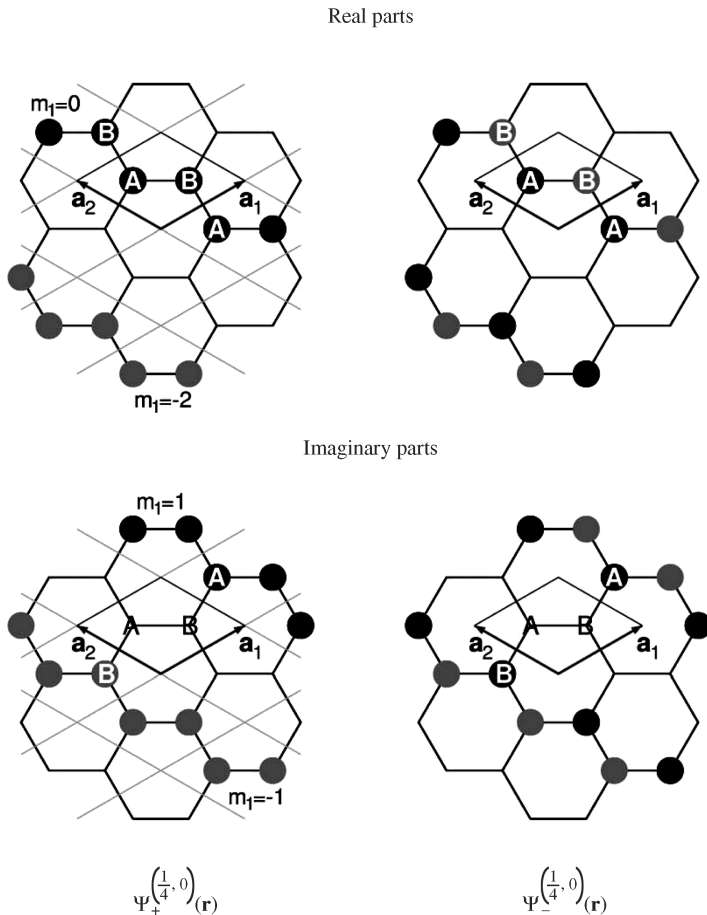


Figure 13 Representation of bonding and antibonding π -crystalline orbitals at $(\frac{1}{4}, 0)$ in graphite.

The graphical representation of Eq. [68] along the contour of the triangle ΓKM (Figure 14) clearly shows that the energy of the π bonding and antibonding COs is a continuous and smooth function of \mathbf{k} , with K being the only point with degeneracy and Γ being the point with maximum energy splitting, where E_+ is the minimum and E_- is the maximum energy. For these characteristics, graphite is reported to be a zero-gap semiconductor, because in fact bands do not cross but are tangent in K . Equation [68] allows us to compute E_{\pm} at any other point in the triangle, which confirms that all these values vary continuously within the range between E^{K} and E^{Γ} . Thus, the chosen path is really representative of the band structure, as expected. The shape of these bands is qualitatively preserved, even when we abandon the crude parametric Hückel's approximation and study the graphite band structure ab initio. The

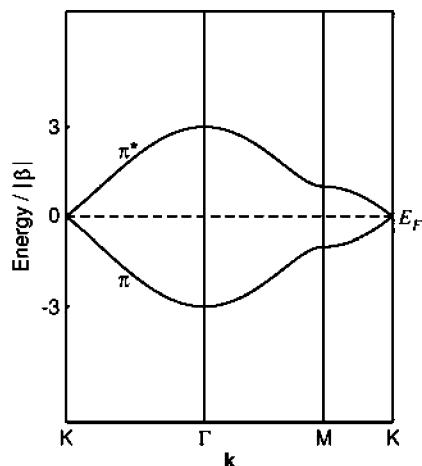


Figure 14 Hückel π -bands of graphite along the K- Γ -M-K path in reciprocal space. Energy is measured in units of β (absolute value) and referred to as α . E_F stands for the Fermi energy.

band structure of graphite in Figure 15 has been obtained with the HF approximation and an extended, all-electron basis set. Direct comparison with bands in Figure 14 is possible because of the one-electron character of the HF approximation, which permits the assignment of each band to a well-defined one-electronic state. The corresponding π and π^* bands compare fairly well,

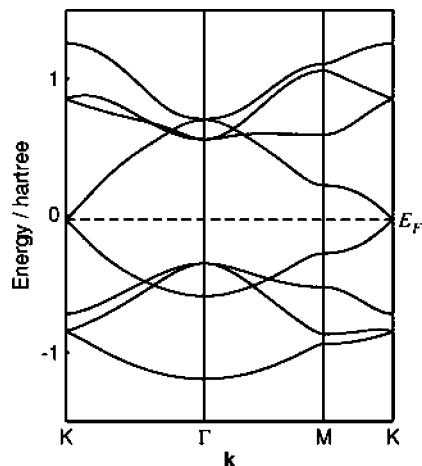


Figure 15 Hartree-Fock valence and conduction band structure of graphite along the K- Γ -M-K path.

although it must be noted that the energy scales used in Figures 14 and 15 are arbitrarily different. The reason why this correspondence happens is that the shape of bands is largely determined by topological features; here, where symmetry is high, a poor approximation of the interactions affects only the energy range and the bandwidth. For example, an extended basis set removes the artifact of complete symmetry between π and π^* bands in Figure 14. However, qualitative aspects, such as band maxima and minima or points of degeneracy, are essentially determined by the symmetry properties of the system. Another remarkable point is that the *bandwidth*, which is a measure of *dispersion* in k -space, clearly depends on the magnitude and the range of the interactions within the crystal (corresponding to the value of β and the number of interactions among the nearest neighbors in Hückel's theory).

The band structure reported in Figure 15 has been obtained by considering all electrons in graphite. Core bands are not represented in the plot because they are separated by a large energy gap from valence bands. However, they are completely flat, which implies that core electrons are effectively screened by valence electrons and do not couple to the rest of the crystal. The four lowest bands in the figure are valence bands, and above them are the first virtual (or *conduction*) bands. The highest energy associated with a populated state of the crystal in its fundamental state is called the *Fermi energy*, the analogue of the highest occupied molecular orbital (HOMO) energy level in molecular cases. The separation between the top of the valence band and the bottom of the conduction band is known as the *conduction-valence gap* (it is zero in this case). Obviously, transitions from the valence to the conduction band are not restricted to this energy, but they can also occur, for example, from the valence band bottom to the conduction band top, so that electron excitation spectra also exhibit bands of possible electronic transitions.

A comparison of graphite with hexagonal boron nitride illustrates more clearly how significant topology is in determining the band structure of a compound and in affecting its properties. Planar BN is isostructural and isoelectronic to graphite, with the obvious exception that some symmetry operations are lost because atoms A and B in the unit cell are no longer equivalent. It belongs to group $P\bar{6}m2$, consisting of 12 symmetry operations. The great similarity of the band structure of BN (Figure 16) to that of graphite (Figure 15) is remarkable: The only important difference is the appearance of a gap between the valence and conduction bands, because degeneracy is lost at K.

This behavior of π and π^* bands can easily be interpreted in terms of simple Hückel's model. In fact, in this case, two different α parameters would appear in Eq. [62], α_B and α_N , and the two solutions would necessarily be distinct:

$$E_+ = \alpha_N \quad E_- = \alpha_B \quad [69]$$

generating a band gap and making BN a semiconductor with more usual characteristics.

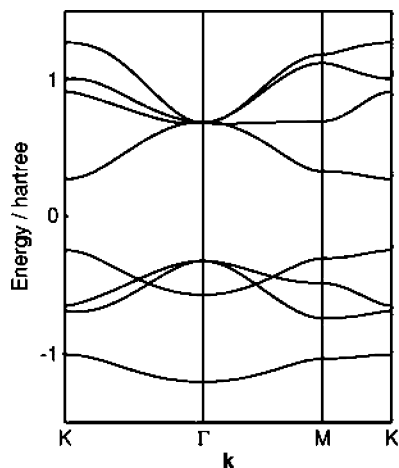


Figure 16 Hartree-Fock upper valence and lower conduction band structure of BN along the K- Γ -M-K path.

Three-Dimensional Periodic Examples

Three-dimensional periodicity makes real crystals more complex structures than polymers and layers, owing to the larger number of the interactions and geometric arrangements involved. Nevertheless, the basic ideas underlying the way band structures originate are essentially the same as those previously mentioned. As it was pointed out, crystals exhibit different properties depending on the different characteristics of their band structure, and in particular, one major classification is based on the extension of the gap between the valence and the conduction bands. Three examples that are representative of different behaviors from this point of view have been included in Figure 17.

Magnesium oxide is a cubic, almost fully ionic oxide with a large band gap, and for this reason, it is classified as an insulator because, even if the real extension of the gap is not as large as is predicted by the HF approximation, the amount of energy that is required by electrons to undergo a transition to virtual states is far beyond the thermal energy at room temperature. Also silicon, which is a covalent crystal, exhibits a band gap. However, this conduction-valence gap is smaller than in the case of MgO, so that silicon is a semiconductor, where virtual states are more easily accessible to electrons. Conversely, no gap is detectable in beryllium, because valence and conduction bands intercross each other. Fermi level passes across them, and a large amount of available empty states are accessible to valence electrons, so that the conduction phenomenon can be easily induced by applying some potential difference through the crystal. For this peculiarity, beryllium is a conductor.

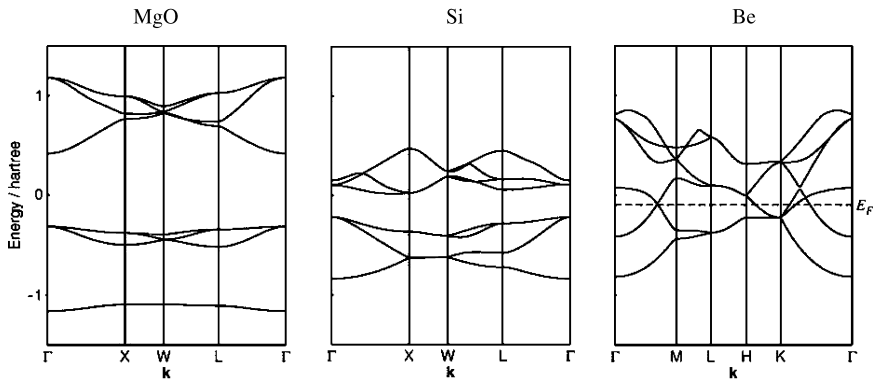


Figure 17 Hartree-Fock upper valence and lower conduction band structure of magnesium oxide, silicon, and beryllium.

The role of crystal symmetry properties in determining the shape of the bands has been emphasized, but the few examples reported have also shown that the existence of a gap and the energy range of bands depend on the mutual interactions of all particles, electrons, and nuclei, in the lattice. Therefore, the correctness of a calculation is largely dependent on the kind of approximation used in the evaluation of such interactions. In fact, different approximations of the Hamiltonian can produce a variety of results and, in particular, band structures that are not only quantitatively but also qualitatively different in some cases. In Figure 18, the HF band structure of silicon is compared with that obtained with DFT methods, both in the LDA, in the form of Slater-Vosko-Wilk-Nusair^{6,90} functional, and with the Becke 3 (B3) parameter-Lee-Yang-Parr (LYP) approximation,⁹¹ which incorporates a part of the exact exchange

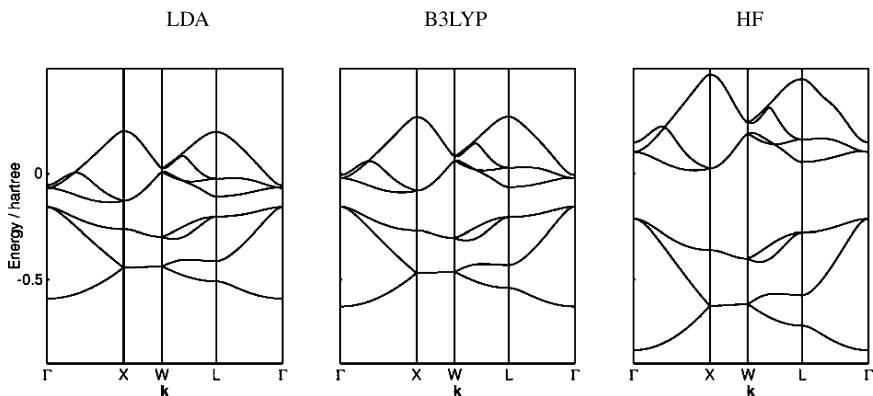


Figure 18 LDA, B3LYP and HF upper valence and lower conduction band structure of silicon.

into the exchange-correlation functional based on the generalized gradient approximation. In spite of the similarity of DFT and HF bands in regard to their shape, the difference between these band structures concerns the basic physical properties of the system. Silicon is predicted to be nearly a conductor by LDA, whereas stimulating conductivity in the HF silicon would be harder. The band gap predicted by LDA for silicon is extremely narrow (0.59 eV), but it is much larger (6.25 eV) according to the HF approximation. The experimental⁹² value is 1.17 eV. Also, bandwidths scale differently in HF and DFT. B3LYP bandwidths are close to LDA, but the inclusion of the exact exchange and gradient corrections increases the gap (1.81 eV).

Please note at this point that the HF and Kohn–Sham (KS) eigenvalues (and the resulting band structure) can be related to the excitation spectrum and the conducting properties of a system only in a loose and qualitative way. In HF theory, Koopmans theorem⁹³ identifies ionization energy I_m with the m -th eigenvalue (with negative sign) of the Hamiltonian, under the assumption that relaxation effects can be neglected, which is a rough approximation. In KS theory, only the eigenvalue corresponding to the highest occupied pseudo-orbital has a rigorous physical meaning, in the limit of an “exact” exchange-correlation functional: It is $-I_m$.^{94,95} Virtual “exact” KS pseudo-orbitals have been shown^{94,95} to represent good approximations of the excitation energies in finite systems in some cases, but unfortunately none of the exchange-correlation functionals currently available can reproduce the real potentials equally well.

More accurate techniques exist for the calculation of excitation energies, which apply the HF and KS solutions just as the starting point in the calculation. They are usually indicated as time-dependent DFT^{76–78} and density functional perturbation theory.^{96,97} As was already mentioned in the Introduction, this matter falls beyond the scope of the present chapter.

The overestimation of bandwidths and gaps obtained with HF compared with the underestimation with LDA is well known. Correct evaluation of the exchange interactions appears as important in band structure calculations, when well-localized electrons are involved. An interesting example is nickel oxide, a compound exhibiting magnetic properties, because of the d -type unpaired electrons in the configuration of the transition metal ions. The different number of spin-up (α) and spin-down (β) electrons per unit cell causes a polarization in the band structure of NiO. The band structures reported in Figure 19 account for the effect of incorporating different percentages of exact exchange into the Becke–Lee–Yang–Parr exchange-correlation potential.^{98,99} B3LYP parameterization corresponds to the inclusion of 20% exact exchange. The edge cases correspond to a pure GGA approximation (on the right end) and to HF corrected by the inclusion of the LYP correlation potential. The width of the gap is clearly proportional to the amount of exact exchange in the exchange-correlation potential, and this term is particularly important in this case to get a correct characterization of NiO as an insulator.

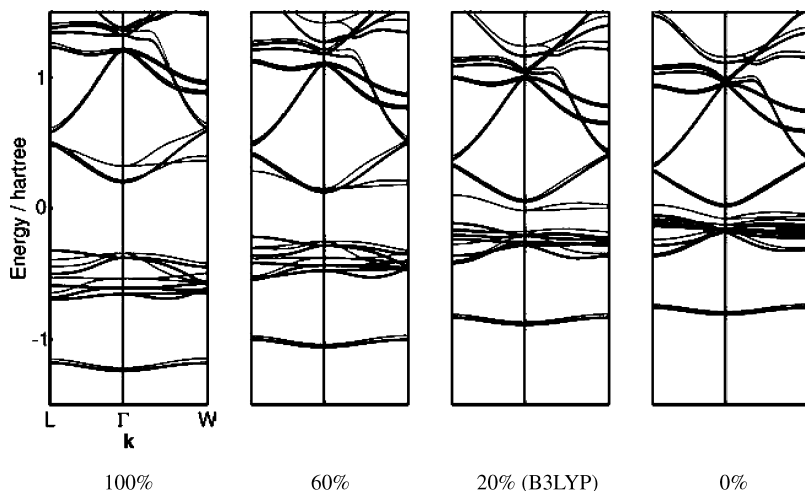


Figure 19 Upper valence and lower conduction band structure of nickel oxide corresponding to different percentages of exact exchange in Becke–Lee–Yang–Parr exchange–correlation functional. Black and gray lines correspond to spin-up and spin-down states, respectively.

These behaviors and the different performance of the different approximations in this respect are well known. Nevertheless, research over the last 20 years has shown that, despite these large errors in the determination of gaps and bandwidths, these methods perform well in predicting a large variety of observables within an error bar that is in most cases acceptable and helping to draw conclusions about interesting physical and chemical properties of matter in the solid state.

From the Band Structure to the Total Energy

Solving the HF or KS equations in the present (CRYSTAL) scheme requires numerical integration over the first Brillouin zone because, in general, we do not possess an analytic expression for the eigenvalues and eigenvectors, as is the case of Hückel’s approximation. The question then becomes: How many points need to be sampled, that is, in how many points must Eq. [25] be solved to get sufficiently accurate values of the observables of interest?

The total energy is important and useful to us for answering this question. As discussed, the total energy of an infinite crystal, like in our model, is infinite. Therefore, the total energy per cell is definitely a preferable choice, for it is a finite well-defined property, because of translation invariance. For the sake of clarity, we remind the reader that, although the total energy per cell is defined within the direct lattice context (Eq. [39]), its calculation depends on knowing the density matrix, which in our scheme is obtained from Eq. [38].

Pack and Monkhorst¹⁰⁰ have suggested that a commensurate grid of points is a suitable option for this purpose. In their method, the grid size depends on a parameter, the shrinking factor s , that specifies how many equidistant \mathbf{k} points must be taken along each direction of \mathbf{b}_1 , \mathbf{b}_2 , and \mathbf{b}_3 inside one reciprocal lattice unit cell so that the total number of points in the grid, n_s , is equal to s^n , with n denoting the order of periodicity ($n = 3$ for three-dimensional crystals).

Magnesium oxide, silicon, and beryllium are three simple and convenient cases for analyzing the accuracy of ab initio periodic calculations in connection with the density of points in the grid. Analyzing their band structures, we can take these systems as representative examples of insulators (MgO), semiconductors (Si), and metals (Be) that are expected to show differences in convergence of various properties as a function of the number of \mathbf{k} points in the Brillouin zone.

The values of the total energy per cell reported in Table 1 as a function of the shrinking factor show that the size of the Pack–Monkhorst grid is related to the extent of the conduction–valence band gap (16.02, 6.25, 0 eV for the three cases considered, respectively).

By recalling that 1 mhartree (~ 2.6 kJ/mol) is less than the amount of energy involved in weak hydrogen-bonding, it is clear that a coarse grid in reciprocal space is sufficient to compute the total energy (and wave function) of an insulator, such as MgO, with high accuracy.

When the gap is smaller, like in silicon, a finer grid is needed to obtain comparable accuracy in the estimate of total energy. For example, uncertainty in the determination of the total energy in the order of 10^{-5} hartree is obtained

Table 1 Total Energy (hartree) per Cell of Magnesium Oxide, Silicon, and Beryllium as a Function of the Shrinking Factor s

s	MgO		Si		Be	
	n_s	E	n_s	E	n_s	E
4	8	-274.67867182	8	-577.87453872	12	-29.28470884
5	10	-274.67995386	10	-577.87691374	15	-29.27944675
6	16	-274.67996773	16	-577.87760126	28	-29.26513569
7	20	-274.67996874	20	-577.87777915	32	-29.27586234
8	29	-274.67996884	29	-577.87782962	50	-29.27312660
9	35	-274.67996884	35	-577.87784429	60	-29.27158322
10			47	-577.87784847	84	-29.27088006
12			72	-577.87785017	133	-29.27244875
16			145	-577.87785036	270	-29.27240692
20			256	-577.87785036	484	-29.27264824
24					793	-29.27278307
28					1200	-29.27276667
32					1734	-29.27279225

Bold digits reflect the level of inaccuracy in the calculated energy values.

with $s = 8$ for silicon and $s = 5$ for magnesium oxide, whereas s is 16 versus 8 for accuracy below 10^{-7} hartree.

When no gap exists, as in the case of beryllium, convergence of the total energy with respect to the grid size is much slower. Data in the last column of the table show that a gain of one order of magnitude in the total energy accuracy implies approximately a factor 3 in s . An additional difficulty in dealing with conducting systems is related to the determination of the Fermi energy, which needs to be known accurately enough for the integration over all populated states, as in the reconstruction of the density matrix (see Eq. [38]). In these cases, band energy is interpolated at points of a finer grid (Gilat's grid^{101,102}) and the new approximated values are used to integrate the number of electrons per cell. In spite of the grid size, this calculation is still easily manageable from the computational point of view because Be is a light atom and the unit cell is small and symmetric. However, a more complicated case could become excessively time consuming. A technique of smearing¹⁰³ the Fermi surface can be helpful in making convergence faster in these cases, where the sharp cutoff in occupancy at E_F would otherwise cause unphysical oscillations in the charge density.

No data are reported for $s < 4$ in Table 1 for a reason. This reason is connected with the tight correlation of the sets of \mathbf{g} direct lattice vectors and \mathbf{k} reciprocal space points selected in the calculation, when using a local basis set. Iterative Fourier transforms of matrices from direct to reciprocal space, like in Eq. [36], and vice versa (Eq. [38]), are the price to be paid for the already mentioned advantage of determining the extent of the interparticle interactions to be evaluated in direct space on the basis of simple criteria of distance. Consequently, the sets of the selected \mathbf{g} vectors and \mathbf{k} points must be well balanced. The energy values reported in Table 1 were all obtained for a particular set of \mathbf{g} vectors, corresponding to the selection of those AOs in the lattice with an overlap of at least 10^{-6} with the AOs in the $\mathbf{0}$ -cell. This process determines the \mathbf{g} vectors for which $F^{\mathbf{g}}$, $S^{\mathbf{g}}$, and the $P^{\mathbf{g}}$ matrices (Eqs. [34] and [38]) need to be calculated, and if the number of \mathbf{k} points included in the calculation is too small compared with the number of the direct lattice vectors, the determination of the matrix elements is poor and numerical instabilities occur.

The number of \mathbf{k} points required to reach a given accuracy for total energy decreases when the unit cell is larger than the ones considered so far. In fact, the adjective "reciprocal" before "space" qualifies the relation of inverse proportionality between direct and reciprocal space (Eq. [3]), so that the bigger a unit cell in real space, the smaller the volume of the corresponding cell in reciprocal space. In those cases where the volume of the first Brillouin zone is small, it is sufficient to solve Schrödinger's equation only at a few \mathbf{k} points. To illustrate this point, we consider what happens when we repeat the calculation for magnesium oxide with nonprimitive cells. In particular, we refer to unit cells with volumes of 4, 16, and 64 times the primitive cell

Table 2 Magnesium Oxide Total Energy per Pair of Mg and O Ions as Determined with Unit Cells Containing n_{MgO} Ion Pairs Corresponding to Grids with Different Values of the Shrinking Factor s

n_s	$n_{\text{MgO}} = 1$	$n_{\text{MgO}} = 4$	$n_{\text{MgO}} = 16$	$n_{\text{MgO}} = 64$
1	—	—	—	-274.67867185
2	—	—	-274.67996667	-274.67996887
4	-274.67867182	-274.67996888	-274.67996886	-274.67996887
8	-274.67996884	-274.67996885	-274.67996886	-274.67996887

volume. Although only one pair of ions exists in the MgO primitive cell, whereas 64 of these pairs (128 ions) are in the biggest unit cell considered in Table 2, we are modeling the same crystal in all cases and the total energy per MgO pair is invariant to the size of the unit cell, provided the method used is numerically stable and accurate. It is apparent that similar levels of accuracy in the total energy value can be obtained with increasingly poorer grids as the direct lattice unit cell volume increases. In particular, when $n_{\text{MgO}} = 64$, using one \mathbf{k} point (the Γ point) is acceptable.

Artificially increasing the unit cell volume to profit from the reduced number of necessary diagonalizations involved in solving Eq. [25] is not a good strategy because of the many more interactions and, consequently, more one- and two-electron integrals to be computed. Nevertheless, this point is indeed relevant in those cases where the size of the primitive cell of a crystal is considerable and the legitimacy for considering a rare grid is a real advantage. For example, in the case of faujasite, a zeolite mineral containing 144 atoms in the primitive cell, 3 \mathbf{k} points in the first Brillouin zone are sufficient to get a total energy value affected by an error of $3 \cdot 10^{-9}$ *hartree* (the error is just one order of magnitude higher when considering the Γ point alone).

Use of Symmetry in Reciprocal Space

The relative cost of ab initio calculations depends on many variables, such as the Hamiltonian, basis set, accuracy requirement, size, and density of the system (see Appendix 2). The Fock or KS matrix diagonalization step during the solution of Eq. [25] can become the calculation bottleneck with a large basis set, when, for example, more than 1000 basis functions are used. Such a number of functions may correspond to about 100 atoms per cell, when a local basis set is used, but this is the usual size of plane wave calculations, even with a small unit cell. As many crystalline systems are highly symmetric, taking advantage of symmetry is, therefore, important for reducing computational time.

Symmetry properties can be used both in the direct and in the reciprocal space, for example, to form matrices in direct space, such as $\mathbf{F}^{\mathbf{g}}$ and $\mathbf{P}^{\mathbf{g}}$, or to diagonalize $\mathbf{F}(\mathbf{k})$ more efficiently. The application of symmetry to direct space

matrices is discussed, for example, in Dovesi¹⁰⁴ and will not be reconsidered here. Instead, we briefly illustrate the use of symmetry properties in reciprocal space, because it is less widely known.

The application of a point symmetry operator of the space group to a given point \mathbf{k} in reciprocal space has two possible consequences:

1. \mathbf{k} is moved to another equivalent point \mathbf{k}' .
2. \mathbf{k} is not moved.

By accounting for the totally symmetric character of the Hamiltonian, it can be demonstrated that in case 1, the eigenvalues of $F(\mathbf{k})$ and $F(\mathbf{k}')$ coincide, and the eigenvectors of $F(\mathbf{k}')$ are directly obtained from the corresponding eigenvectors of $F(\mathbf{k})$ by the action of that symmetry operator. Moreover, $F(\mathbf{k})$ and $F(-\mathbf{k})$ are always related by symmetry, even if inversion is not present in the space group, owing to the so-called “time reversal symmetry.”¹⁰⁵ In fact, by taking the complex conjugate of Eq. [25] and considering the structure of the COs (Eq. [24]), it is seen that the eigenvalues are the same at \mathbf{k} and $-\mathbf{k}$, because they are real, and the eigenvectors are the complex conjugate of one another. On the basis of these considerations, it is, therefore, recommended that Eq. [25] be solved only at points belonging to the asymmetric part of the first Brillouin zone (the minimal set of symmetry unrelated \mathbf{k} points), as was done in previous examples. Indeed, the use of this kind of symmetry is so easy that it is probably implemented in all periodic codes. In Table 1, we can appreciate how far calculations benefit from symmetry type 1 by comparing n_s , the actual total number of \mathbf{k} points where $F(\mathbf{k})$ was diagonalized, with s^3 , the total number of \mathbf{k} points in the entire first Brillouin zone: The ratio of n_s to s for cubic systems like MgO and Si, when $s = 8$, is close to 1/20th (1/18.2).

As a second step, symmetry type 2 can be applied to the set of the n_s \mathbf{k} points, which allows one to further reduce the Fock matrix into a block-diagonal form. By transforming the basis set into an equivalent set of symmetry adapted basis functions, every block of the transformed matrix in Figure 4, which corresponds to one particular point \mathbf{k}_j , reveals, in turn, a block-diagonal structure, for example, of the kind depicted in Figure 20.

Each block in the matrix on the right corresponds to a different irreducible representation (IR) of the so-called “little co-group,”¹⁰⁶ and the number

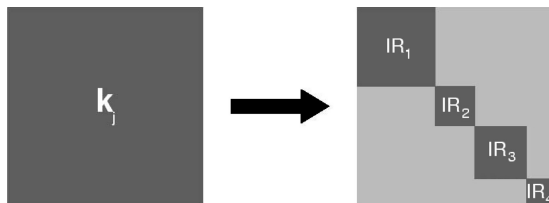


Figure 20 Block-factorization of the Fock matrix corresponding to a specific \mathbf{k} point, \mathbf{k}_j .

of these blocks varies with the symmetry invariance properties of \mathbf{k}_j . As a matter of fact, the application of this kind of symmetry properties to the solution of Eq. [25] is not trivial,^{107,108} but the gain in computational efficiency is dramatic in the case of highly symmetric systems with large unit cells, when diagonalization dominates the calculation.

As an example, we consider pyrope, a garnet that crystallizes according to the cubic space group $Ia3d$, with four $Mg_3Al_2Si_3O_{12}$ formula units per cell consisting of 80 atoms. Shrinking factor $s = 2$ has already been indicated as convenient for such a large unit cell, and symmetry type 1 reduces n_s , the number of \mathbf{k} points to be accounted for, from 8 to just 3: Γ , $H(\frac{1}{2}, \frac{1}{2}, \frac{1}{2})$, and $N(\frac{1}{2}, 0, 0)$. The eigenvectors at these points are all real. If we use a local basis set consisting of $n_f = 1440$ AOs, which corresponds to the choice of a split-valence basis set plus polarization functions for every atom in the unit cell, the size of the matrices in Eq. [25] would be 1440×1440 . But because of symmetry type 2, they can be decomposed into lower size independent blocks as reported in Table 3.

Γ is the most symmetric \mathbf{k} point in the reciprocal space, and all irreducible representations of the O_h point group are contained in the matrices. This situation is the most favorable from the point of view of computational efficiency. In fact, the size of the largest block is $n_f^{T_{2g}} = 90$. Moreover, knowing just one of the eigenvectors for every IR with $d_{IR} > 1$ is enough to obtain the other $(d_{IR} - 1)$ eigenvectors simply by application of the corresponding transfer operators. Thus, only one diagonalization is necessary for each IR. This property is particularly effective when d_{IR} is large, and in this respect, the appearance of IR with d_{IR} as large as 6 (see IR H at point H in Table 3) is an important peculiar feature of symmetry in reciprocal space, which does not occur in direct space. The application of symmetry type 2 has a smaller

Table 3 Example of Decomposition of Fock, Overlap, and Eigenvector Matrices of Pyrope (with a Local Basis Set of $n_f = 1440$ AOs) into Independent Irreducible Blocks at \mathbf{k} Points Γ , H , and N in the First Brillouin Zone

Γ			H			N		
<i>IR</i>	d_{IR}	n_f^{IR}	<i>IR</i>	d_{IR}	n_f^{IR}	<i>IR</i>	d_{IR}	n_f^{IR}
A_{1g}	1	34	E	2	60	E_1	2	358
A_{2g}	1	32	F	2	114	E_2	2	362
E_g	2	60	H	6	182			
T_{1g}	3	88						
T_{2g}	3	90						
A_{1u}	1	32						
A_{2u}	1	30						
E_u	2	62						
T_{1u}	3	88						
T_{2u}	3	88						

n_f^{IR} is the size of the block belonging to one row of the irreducible representation IR with dimension d_{IR} .

impact at N , where the decomposition results in two different blocks only. Nevertheless, even in this case, the size of the bigger matrix is $n_f^{E_2} = 362$, i.e., about one fourth of the original matrix.

TOTAL ENERGY, ENERGY DIFFERENCES, AND DERIVATIVES

In the previous section, we have examined the dependence of the total energy of a system on the number of \mathbf{k} points and have illustrated a convenient use of symmetry for reducing the computational effort. Many other elements influence the accuracy of the method, which for clarity and conciseness, can be grouped into three categories:

1. The Hamiltonian
2. The adopted basis set
3. The computational scheme (the implementation of the basic equations in a specific code).

We will further analyze the problem of accuracy in the calculation of the total energy and its derivatives through a few examples, where we must take into account that, from the physical or chemical point of view, we are never interested in the total energy of a system as such, but rather in energy differences, that might be as small as a few kcal/mol. It is with respect to this scale of energy that the overall accuracy of a calculation must be verified. In fact, systematic improvement of algorithms in molecular codes during the past 40 years now allows an accuracy of 1 kcal/mol for thermochemical data,¹⁰⁹ which is still far from being attained in solid state chemistry, although attention to the quantitative aspects of the calculation is increasing rapidly.

Why is the total energy such an important observable? Reactivity of a surface, formation of a defect, and structural modification of a material to enhance some of its properties can all be discussed with reference to the total energy easily and rigorously. Moreover, knowledge of the total energy derivatives is also informative concerning the equilibrium properties, lattice dynamics, and the response of materials to perturbations. Table 4 lists some of the many energy differences that are relevant in solid state chemistry. Most of them imply a comparison of systems with different periodicity, therefore, it is important that zero- (atoms or molecules), one- (polymeric chains), two- (slabs), and three-dimensional (bulk) systems all be handled in a consistent way, as concerning not only the method used but also the computational conditions, so that the comparability of the total energy be guaranteed to a high degree. As the systems involved in the comparison must be at equilibrium, finding the equilibrium geometry is preliminary to any energy difference calculation and selection of an efficient technique for geometry optimization is another requirement in this kind of calculation. The CRYSTAL code satisfies

Table 4 List of Some Relevant Energy Differences in Solid State Chemistry

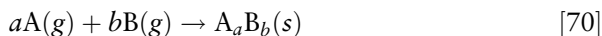
Computed energy	System 1	System 2	Example
Cohesive	Bulk	Atoms	Ionic, covalent crystals
Interaction	Bulk	Molecules	Molecular crystals
Relative stability	Bulk	Bulk	Polymorphism
Super-exchange	AFM bulk	FM bulk	NiO magnetic phases
Solid state reaction	Bulk	Bulk	$\text{MgO} + \text{Al}_2\text{O}_3 \rightarrow \text{MgAl}_2\text{O}_4$
Surface formation	Bulk	Slab	MgO(100)
Surface stability	Slab	Slab	MgO(100) vs MgO(110)
Adsorption	Slab + molecule	Slab, molecule	CO on MgO(100)
Adsorption	Bulk + molecule	Bulk, molecule	NH ₃ in acidic zeolites
Interface	Slab	Slab	MgO monolayer on Ag(100)
Substitution defect	Bulk + defect	Bulk, atoms	C in Si

both these requirements. Four examples of energy calculations involving bulk systems with CRYSTAL are discussed in this section. Other cases will be presented in the sections devoted to surfaces and defects.

Cohesive Energy

Ionic, Covalent, and Metallic Crystals

The *cohesive energy* is the energy necessary to dissociate a solid into separated entities, generally the atoms. Following this definition, the cohesive energy (ΔE) of a crystalline compound with formula unit A_aB_b , for example, is associated with the reaction of formation of A_aB_b in the solid state from the noninteracting atoms A and B in the gas phase



and is computed as

$$\Delta E = aE^{\text{atom}}(A) + bE^{\text{atom}}(B) - E^{\text{bulk}}(A_aB_b) \quad [71]$$

Hence, ΔE is positive for any thermodynamically stable crystal. This definition of cohesive energy is not unique. As alternative definitions, reference can be made to the ions in the case of ionic crystals or to the molecules for molecular crystals. Another expression, lattice energy, is also in use, either as a synonym of cohesive energy or to denote the energy difference relative to the ions or molecules, thereby distinguishing it from the cohesive energy referred to the atoms. Thus, some care must always be taken when analyzing data in the literature in regard to nomenclature. We will use the following symbols: ΔE^{atoms} , ΔE^{ions} , and ΔE^{mol} .

As occurs in the calculation of molecular binding energies, the expression for ΔE implies basis sets that are complete. However, partial basis set

incompleteness is commonly accepted in molecular calculations, provided all terms involved in the expression of the binding energy are computed with the same basis sets. This procedure becomes critical in most cases in the solid state. In fact, convenient basis sets for atoms are generally overcomplete in crystals, where close packing makes atomic function tails unnecessary in the description of the crystalline wave function. Moreover, the use of diffuse AOs with a periodic potential is normally to be avoided, for it may introduce artificially unwanted numerical instability in the calculation of the eigenvalues and eigenvectors of the Hamiltonian. Therefore, in the evaluation of the cohesive energy, partially different basis sets, as concerns the description of the valence region, need to be used for the atoms or ions and the bulk, in most cases.

We will illustrate how these problems can be handled with a simple example: the cohesive energy calculation of bulk NaCl with the HF approximation. Following Pople's scheme for the construction of a basis set, we adopt the convention that every set of (p_x , p_y , p_z) orbitals share the same gaussian function with one s-type AO and these four AOs collectively form an sp shell. An *all-electron* basis set optimized for the bulk is available (see Prencipe et al.¹¹⁰), which consists of one core s-type AO plus three and four sp shells with the origin at Na and Cl, respectively. The exponents of the outer Gaussian functions of both Na and Cl are reported in Table 5 (Case 1). The system is fully ionic, in accordance with the usual representation of NaCl as a salt consisting of Na^+ and Cl^- ions, which explains why the exponent of the outermost Gaussian of the cation, i.e., $\alpha_b(\text{sp})$ in the first row of Table 5, is about three times larger than at the anion (the valence orbitals of Na^+ are basically empty). When the same basis is used to compute the atomic and ionic energies, an extremely large value of ΔE^{atoms} results (Case 1 in Table 6). This is clear evidence of the poor performance of that basis set in the calculation of the atomic energies, which are severely underestimated (Case 1 in Table 7), particularly for $E(\text{Na})$. Indeed, readjustment of $\alpha_b(\text{sp})$ for the atoms and ions in the gas phase is necessary to improve ΔE^{atoms} (Case 2). Obviously, the best

Table 5 Exponents of the Most Diffuse Shells (in Bohr⁻²) of Na and Cl as Optimized for Bulk NaCl and for the Isolated Atoms and Ions at the HF Level

Case	System	Na				Cl			
		$\alpha_a(\text{sp})$	$\alpha_b(\text{sp})$	$\alpha_c(\text{sp})$	$\alpha_a(\text{d})$	$\alpha_a(\text{sp})$	$\alpha_b(\text{sp})$	$\alpha_c(\text{sp})$	$\alpha_a(\text{d})$
1	bulk	0.578	0.323			0.320	0.125		
2	atom	0.497	0.042			0.315	0.119		
	ion	0.542	0.229			0.294	0.090		
3	atom	0.509	0.089	0.030		0.297	0.248	0.116	
	ion	0.539	0.204	0.111		0.329	0.151	0.059	
4	bulk	0.578	0.323	0.125		0.320	0.125		
5	bulk	0.578	0.323	0.125	0.400	0.320	0.125		0.400

Table 6 HF Computed Cohesive Energy for NaCl (in kJ/mol) with Respect to the Isolated Atoms and Ions

Case	ΔE^{atoms}	ΔE^{ions}
1	1499.8 (+132.8)	761.0 (−3.8)
2	521.0 (−19.1)	744.3 (−5.9)
3	512.0 (−20.5)	738.3 (−6.7)
4 ^a	513.3 (−20.3)	739.6 (−6.5)
5 ^a	515.8 (−19.9)	742.1 (−6.2)
Exp.	644.2	791.3

Percentage underestimation/overestimation of the experimental cohesive energies in parentheses. Cases 1–5 correspond to different basis sets in Table 5.

^aCohesive energy computed with respect to atomic and ionic energy of Case 3.

Table 7 HF Total Energy (in Hartree) of the Isolated Atoms and Ions Obtained with the Basis Set of Cases 1–3 Reported in Table 5

	Case 1	Case 2	Case 3
Na (g)	−161.475779	−161.848514	−161.850828
Na ⁺ (g)	−161.669712	−161.670010	−161.670022
Cl (g)	−459.449667	−459.449740	−459.450841
Cl [−] (g)	−459.537121	−459.543201	−459.545457

exponents for the isolated atoms are smaller than in the bulk (Case 2 in Table 5) and the corresponding change in ΔE^{atoms} (Case 2 in Table 6) is dramatic, at the same time being far from negligible (about 2%) in ΔE^{ions} . The addition of one extra sp shell to the basis sets of the isolated atoms and ions (Case 3), followed by re-optimization of the outer valence shell exponents, still decreases both ΔE^{atoms} and ΔE^{ions} by about 1%. Actually, Case 3 corresponds to the hypothesis that extra functions added to the bulk basis set would have no effect on the bulk total energy, which is almost true, as results from a comparison with Case 4.

Also the bulk basis set can still be improved by the addition of polarization functions, which do not contribute to the energy of atoms and ions in the gas phase because of AO orthogonality, but they can be important in the expansion of the bulk wave function. However, in this particular case, the contribution from polarization functions to the bulk total energy (Case 5) is minimal, because of high symmetry and the nearly spherical shape of the closed-shell ions.

Table 6 demonstrates that separate optimizations of the basis sets for the bulk and the isolated atoms or ions is mandatory for obtaining the cohesive energies of ionic compounds. As a general rule, *variationally equivalent* basis sets are to be used for the bulk and the atoms or ions, rather than *equal* basis sets.

Apparently, further improvement of the basis sets would hardly affect the values of ΔE in Table 6, which are much smaller than the corresponding

Table 8 Cohesive Energies (in kJ/mol) of LiF, NaCl, KBr, MgO, Si, and Be Computed with Respect to the Atoms with Different Hamiltonians

	HF	LDA	PW91	B3LYP	CCSD(T)	Exp.
LiF	656.6 (-23.7)	958.1 (+11.3)	850.7 (-1.2)	825.5 (-4.1)	845.4 (-1.8)	861.1
NaCl	512.0 (-20.5)	685.3 (+6.4)	614.7 (-4.6)	589.9 (-8.4)	627.5 (-2.6)	644.2
KBr	477.1 (-21.2)	611.9 (+1.1)	554.8 (-8.4)	533.9 (-11.8)	579.7 (-4.2)	605.4
MgO	699.5 (-29.3)	1118.7 (+13.0)	966.4 (-2.4)	908.0 (-8.3)	969.3 (-2.1)	989.8
Si	643.9 (-29.7)	1101.5 (+20.2)	943.3 (+2.9)	850.9 (-7.2)	852.8 (-7.0)	916.6
Be	180.1 (-43.6)	372.7 (+16.8)	319.2 (0.0)	259.0 (-18.9)	—	319.2

Percentage difference between calculated and experimental data in parentheses.

experimental values. Indeed, HF underestimates ΔE^{atoms} of NaCl by about 20% and ΔE^{ions} by about 6%. The origin of such a poor approximation is to be found in intra-ionic and interionic correlation effects, both disregarded at this level of theory, although the better agreement for ΔE^{ions} is caused by cancellation of intra-ionic correlation effects when subtracting the energy of the ions from that of the bulk.

The underestimation of the cohesive energy is a general feature of HF, as can be seen in Table 8, where ΔE^{atoms} is reported for a series of different simple crystalline compounds, which includes three alkali halides with increasing ion size, an ionic oxide with stronger electrostatic interactions caused by divalent ions (MgO), a covalent system (Si), and a metal (Be).

The error in the HF cohesive energy varies between -20% and -45% for this series. In accordance with the interpretation of electron correlation as the source of such an error, DFT calculations of ΔE allow one to recover part of the contributions that are disregarded with HF, at about the same computational cost. LDA tends even to overestimate the cohesive energy, whereas GGA and B3LYP results are closer to the experimental measurements. At any rate, the performance of none of the Hamiltonians used is fully satisfactory, and the correct answer is always somewhere in between the two extremes represented by HF and LDA, but LDA results are generally improved when gradient corrections are included.

Properly correlated wave functions are obviously expected to perform better than HF and DFT methods. A systematic post-HF investigation of correlation effects in crystalline compounds has been obtained with the “incremental scheme” of Stoll^{71,72} at both CCSD and CCSD(T) levels.⁷³⁻⁷⁵ The CCSD(T) cohesive energies reported in Table 8, in fact, agree on average better with the experimental data than the one-electron results.

Another aspect of the comparison between the calculated and experimental cohesive energy is important to recall here. It is related to the difference between the definition of cohesive energy and the crystal formation energy that is reported in thermodynamic tables, the main point probably being that quantum mechanical calculations refer to the static limit ($T = 0$ K and frozen nuclei), whereas experiments refer to some finite temperature. In fact, the

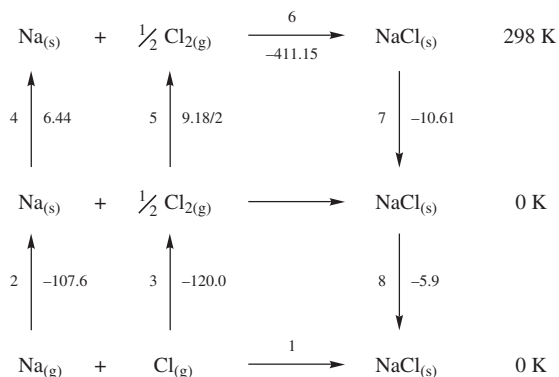


Figure 21 Born–Haber cycle used to correct the experimental formation energy of NaCl from 298 K to the static limit.

comparison is never straightforward, and the original experimental datum is linked to the calculated cohesive energy values through a chain of thermodynamic transformations. As an example, the Born–Haber cycle for the formation of NaCl is reported in Figure 21. The calculated cohesive energies reported in Tables 4 and 5 refer to step 1, i.e., to the formation of the crystal at 0 K from the pure atoms in the gas phase, whereas the tabulated experimental datum refers to the standard formation reaction of NaCl at room temperature, step 6 ($\Delta H_{298}^0 = -411.15$ kJ/mol) of the cycle. Hence, the experimental value reported in Table 8 corresponds, instead, to the path consisting of steps 2–8 of the Born–Haber cycle. These steps are as follows: (2) condensation of Na atoms from the gas phase (the inverse of the sublimation enthalpy); (3) formation of Cl_2 molecules (the inverse of the enthalpy of dissociation); (4) heating solid Na atoms to room temperature; (5) heating Cl_2 molecules to room temperature; (6) formation of crystalline NaCl from the elements in their standard states at room temperature; (7) cooling NaCl to 0 K. These enthalpy differences are tabulated¹¹¹ (ideal behavior of Cl_2 is assumed in step 5). Step 8 refers to the zero point energy ϵ_0 , which is usually not available experimentally. The Debye model (see, for instance, p. 100 of Hill¹¹²) relates ϵ_0 to Debye’s temperature Θ_D , through the following equation:

$$\epsilon_0 = n9/8k_B\Theta_D \quad [72]$$

where k_B is the Boltzmann’s constant and n is the number of atoms in the unit cell. Debye temperatures for alkali halides can be found in Ashcroft and Mermin¹⁰⁵. Θ_D is 321 K for NaCl. In conclusion, the experimental *static* cohesive energy of NaCl reported in Tables 6 and 8 originates from the following sum:

$$\begin{aligned}
 -\Delta E_{\text{static}}^{\text{atoms}} &= -107.6 - 120.0 + 6.44 + \frac{9.18}{2} - 411.15 - 10.61 - 5.9 \\
 &= -644.2 \text{ kJ/mol} \quad [73]
 \end{aligned}$$

The experimental lattice energy at the static limit can also be evaluated with respect to the isolated ions, and it is easily obtained by including the ionization energy of the alkali metal (Na) and the electron affinity of the halogen (Cl). According to *The Handbook of Chemistry and Physics*,¹¹¹ the ionization energy of sodium is -495.8 kJ/mol and the electron affinity of chlorine is 348.7 kJ/mol. Then, the experimental cohesive energy from ions is 791.3 kJ/mol at the static limit.

Molecular Crystals

The cohesive energy of molecular crystals is usually computed with reference to the molecules in the gas phase, like in a sublimation process, so that calculated values of ΔE^{mol} can be compared with experimental sublimation energies. ΔE can be decomposed into two terms:

$$\Delta E^{\text{mol}} = -\Delta E_{\text{condensation}} - \Delta E_{\text{conformation}} \quad [74]$$

with the first term referring to the condensation of molecules from the gas phase, but with the same conformation as in the crystal, and the latter to the difference between the energies of the isolated molecules in the bulk and in the gas phase conformations. $\Delta E_{\text{conformation}}$ is negligible in the case of rigid molecules, but it can be significant for floppy molecules.

Let us consider urea as an example. Crystalline urea is tetragonal, with two molecules in the unit cell (Figure 22a). The molecules are linked to each other through hydrogen bonds to form infinite planar tapes (Figure 22b), which are mutually orthogonal, the cohesion among them being provided by hydrogen bonds. Every oxygen atom is involved in four nearly equivalent hydrogen bonds, two within the tape and the other two linking neighboring tapes. Molecules in nearest neighboring tapes are oriented along opposite directions; this provides additional stabilization through dipole-dipole

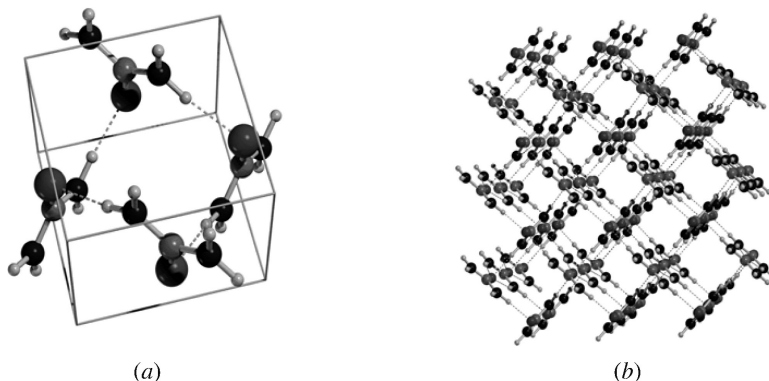


Figure 22 (a) Crystalline urea unit cell. (b) Arrangement of urea molecules in the crystalline structure.

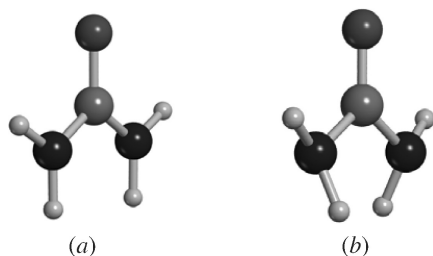


Figure 23 Urea molecular structures: (a) C_{2v} conformation as found in the crystalline structure; (b) C_2 *anti* conformation as found in the gas phase.

interactions, and it annihilates the total dipole of the unit cell, as is always the case in molecular crystals

A molecule in bulk has C_{2v} symmetry, whereas the most stable structure in the gas phase corresponds to a C_2 -symmetric *anti* conformation (see Figure 23). The C_{2v} geometry is a second-order saddle point on the potential energy surface.¹¹³ Therefore, $\Delta E_{\text{conformation}}$ between conformers must be taken into account when computing the cohesive energy.

The cohesive energy of urea with respect to the molecules in the gas phase is calculated as

$$\Delta E^{\text{mol}} = \frac{2E(\text{molecule}) - E(\text{bulk})}{2} \quad [75]$$

In this form, ΔE^{mol} is the cohesive energy per molecule and the factor 2 in the formula is caused by the presence of two molecules in the unit cell. The cohesive energies computed with different Hamiltonians and Pople's 6-31G(d,p) basis set are reported in Table 9. At variance with the case of ionic crystals, molecular-devised basis sets can generally be used for molecular crystals as such, without any exponent reoptimization. As shown in Table 9, $\Delta E_{\text{conformation}}$ accounts for 5–8 kJ/mol. Table 9 also shows that DFT-based

Table 9 Cohesive Energy (ΔE^{mol}) per Molecule of Crystalline Urea Calculated with the Experimental Lattice Parameters (in kJ/mol)

Hamiltonian	$\Delta E_{\text{condensation}}$	$\Delta E_{\text{conformation}}$	ΔE^{mol}	ΔE^{CP}
HF	−80.2	4.9	75.3	54.4
LDA	−177.0	4.9	172.1	135.2
PW91	−124.5	7.5	117.0	79.1
B3LYP	−105.2	6.7	98.5	63.6

ΔE^{CP} includes the correction for the basis set superposition error, estimated via the counterpoise method (CP).

methods give larger ΔE^{mol} than HF, as the correlation energy, somehow included in DFT, makes the crystalline structure more stable.

When the local basis set is incomplete at some extent, the basis set superposition error (BSSE)^{114,115} affects the cohesive energy more extensively than the binding energy in molecules. In fact, in calculating the wave function and total energy of a molecular crystal with a finite basis set, the description of molecule A in the crystal will be improved by the variational freedom provided by the functions of the adjacent molecule B, and vice versa. As a consequence, the energy content of A and B in the crystalline environment turns out to be overestimated, as if an extra binding occurred between A and B. This error is commonly corrected via the counterpoise (CP) method, as proposed by Boys and Bernardi,¹¹⁶ by supplementing the basis set of an isolated molecule with the functions of an increasing number of atoms (ghost atoms) belonging to the surrounding array of molecules that would be present in the crystal. An introductory tutorial about the theory and the practice of BSSE has been published in this book series.¹¹⁵ An interesting discussion of the BSSE problem in molecular crystals can be found in a recent paper by Spackman and Mitchell.¹¹⁷

The dependence of the BSSE on the number of the accounted neighboring atoms in crystalline urea is shown in Figure 24a. The correction converges to a limiting value of about 38.0 kJ/mol, with the largest calculation including 98 ghost atoms. Nevertheless, 30 neighbors are enough to reach a value of 35.3 kJ/mol that represents about 93% of the entire CP correction.

Thus, proper consideration of the BSSE correction decreases ΔE^{mol} considerably at all levels of theory considered here. On the contrary, basis set

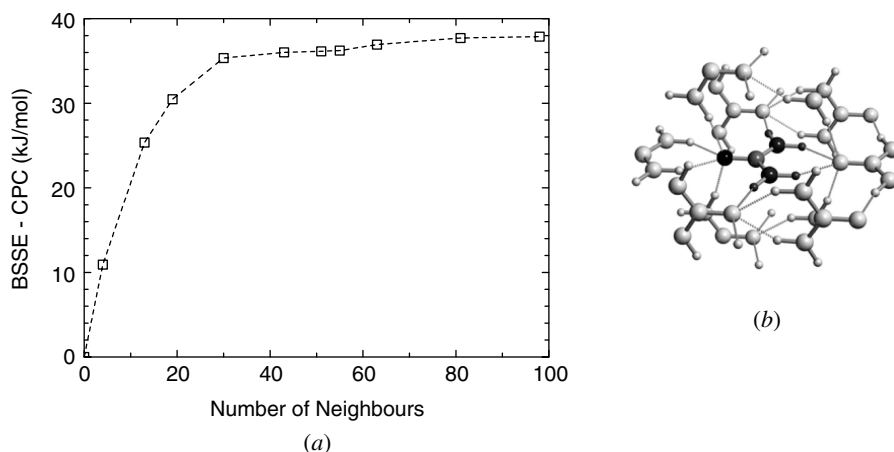


Figure 24 (a) Dependence of the BSSE on the number of neighboring atoms included in the CP correction for crystalline urea, with the LDA approximation (SVWN) and a 6-31G(d,p) basis set. (b) Urea molecule surrounded by a star of 63 neighboring ghost atoms.

improvements, which have been shown to be so relevant in the calculation of the cohesive energy of ionic systems, and particularly with respect to the atoms, are much less important in computing ΔE^{mol} of a molecular crystal like urea. The BSSE-corrected B3LYP cohesive energies obtained with two standard Pople's basis sets, namely 6-31G(d,p) and 6-311G(d,p), and a double- ζ plus polarization basis proposed by Thakkar et al.¹¹⁸ are 63.6, 61.1 and 64.1 kJ/mol, respectively, thus showing an almost negligible dependence on the basis set used, although the BSSE correction decreases with the basis set size.

The experimental sublimation energy of crystalline urea is 90.0 kJ/mol¹¹⁹ and 97.7 kJ/mol after correction for the zero point energy (ab initio estimate), which is more properly compared with the results from calculations. Unfortunately, none of the calculated ΔE^{CP} in Table 9 compares well with this latter value, with the minimum found error being about 20% of the cohesive energy. However, the computed cohesive energies follow closely the trend obtained for hydrogen bonded molecular adducts (see, for instance, Civalleri et al.¹²⁰), where LDA functionals, like SVWN, tend to greatly overestimate the interaction energy, whereas gradient-corrected and hybrid functionals represent definite improvements with respect to LDA. On the other hand, as thermal effects are expected to account only for a few kJ/mol, the difference with respect to experiment must then be traced back to other effects, probably to the lack of dispersion interactions, which are not taken into account¹²¹ at one-electron levels of theory.

Other examples of applications of the CRYSTAL code to molecular crystals include ice polymorphs,^{122–124} orthoboric acid,¹²⁵ vitamin C,¹²⁶ oxalic acid dihydrate,¹²⁷ and *p*-benzoquinone.¹²⁸

Polymorphism

Silica is of great interest in solid state chemistry, as it exists in many different crystalline forms, from high-density polytypes (e.g., quartz, cristobalite, tridymite) to low-density microporous all-silica zeotypes. Despite their enormous structural complexity, silica polymorphs show similar stability. From calorimetric measurements,^{129–132} it is known that α -quartz is the most stable polymorph at room temperature and pressure, with all other polymorphs being confined within a range of just 15 kJ/mol. This small range makes an accurate simulation of the relative stability of silica polymorphs a delicate but challenging task. In fact, quartz and all-silica polytypes have been the subject of many theoretical studies.^{133–135} Here, we consider the relative stability of β -quartz (β -Q), α -cristobalite (α -C), α -tridymite (α -T), sodalite (SOD), chabazite (CHA), faujasite (FAU), and edingtonite (EDI) with respect to α -quartz (α -Q). Frameworks are shown in Figure 25.

In Table 10, CRYSTAL all-electron (AE) calculations at both HF and DFT level of theory (LDA and B3LYP) are compared with shell model results and ab initio PW calculations.¹³⁵ G(HF)¹³⁶ and G(B3LYP)¹³⁷ refer to

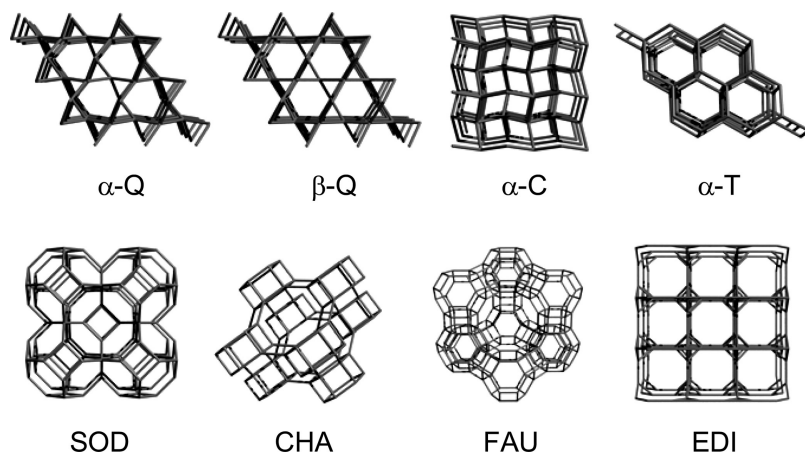


Figure 25 Frameworks of the studied all-silica polymorphs.

a semiclassical approach with model interatomic potentials that were fitted to ab initio calculations on molecular clusters simulating fragments of microporous all-silica frameworks.

The range and the order of stability computed with a local AE basis set are in good agreement with the experimental measurements available, particularly as concerns the B3LYP results (third row in Table 10). Also the G(B3LYP) parameterization of the semiclassical method provides results that are in reasonably good agreement with the experimental evidence. However, the ab initio approach is still to be preferred in the case of more complicated systems, such as Ti-substituted zeolites, for example, where the parameterization procedure may become critical.

Perhaps the most surprising feature in Table 10 is the large difference between AE and PW results, obtained at the same levels of theory. The origin of this inconsistency is probably caused by the different computational

Table 10 Relative Stability (in kJ/mol per SiO_2 unit) of Silica Polymorphs with Respect to α -Q

	β -Q	α -C	α -T	SOD	CHA	FAU	EDI
AE-HF	3.1	0.0	1.7	4.6	6.3	7.6	11.6
AE-LDA		9.1	12.9				
AE-B3LYP		1.2	4.3	5.7	7.0	7.8	11.6
G(HF)	1.6	-3.8	-2.8	0.5	4.4	8.1	9.5
G(B3LYP)		1.4	7.7	7.7	8.6	9.8	13.0
PW-LDA	2.5	2.4	3.3				
PW-GGA	0.2	-3.1	-2.2				
Exp. (ΔH^{298})		2.8	3.2		11.4	13.6	

conditions used by scientists in the different implementations of the method, and especially in the different representations of the wavefunction. These results are a good indication of how much computational and methodological aspects can affect results in solid state calculations, where full standardization has not yet been achieved.

Magnetic Phases

Another context in which simple energy differences provide useful information to chemists is magnetism. The magnetic properties of transition metal insulators such as KMF_3 perovskites ($M = \text{Mn, Fe, Co, Ni, Cu}$)^{138–140}, simple MO oxides ($M = \text{Ni, Mn}$)^{140,141} M_2O_3 sesquioxides ($M = \text{Cr, Fe}$)^{142,143} complex oxides such as Mn_3O_4 (hausmannite),¹⁴⁴ rutile type fluorides MF_2 ($M = \text{Mn, Fe, Co, Ni, Cu}$)^{145–147} and high- T_c superconductor parent compounds¹⁴⁸ have been investigated extensively.

As an example, we discuss the relative stability of some magnetic phases of KMnF_3 , an ionic perovskite, with cubic lattice, where each Mn ion is at the center of a regular octahedron of fluorine ions. Different magnetic structures can be envisaged, as shown in Figure 26. The structure on the left represents a ferromagnetic (FM) phase with the spin at the Mn ions all parallel ($S_z = 5/2$). In the middle, an antiferromagnetic (AFM) phase is shown, where the Mn ions, carrying five unpaired electrons each, are arranged in alternating stacked spin-up and spin-down (111) planes. In the AFM' structure on the right, each Mn atom is surrounded by two Mn nearest neighbors with opposite spin and four with the same spin, thus forming a sequence of alternating spin-up and spin-down Mn (001) planes. Because of the presence of alternating antiparallel spin Mn planes, the two different antiferromagnetic phases imply the use of double supercells.

Information about the basis sets and other computational details can be found in Dovesi et al.,¹³⁸ Harrison et al.,¹³⁹ and Mallia et al.¹⁴⁰ The hypothetical spin arrangement shown in Figure 26 is a schematic representation of a point charge lattice, where the unpaired electrons are fully assigned to the

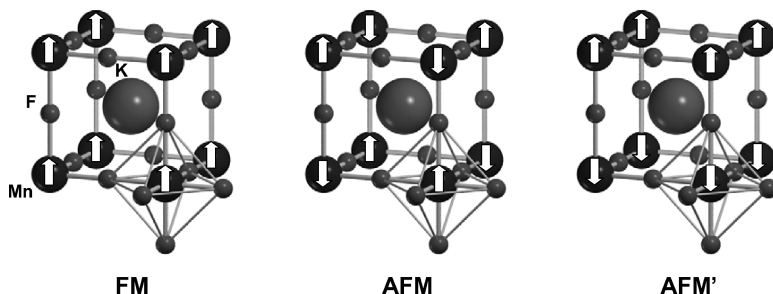


Figure 26 Magnetic phases of KMnF_3 . Arrows denote spin-up and spin-down Mn ions.

Table 11 Net Atomic Charges (q) and Spin Moments (μ) in KMnF_3 Evaluated According to Mulliken Partition of Spin Density

	Mn		F		K	
	q	μ	q	μ	q	μ
FM	1.77	4.94	-0.92	0.02	0.99	0.00
AFM	1.77	4.94	-0.92	0.02	0.99	0.00

Values of q and μ are given in electrons.

transition metal ions. This picture is actually not far from quantum mechanical reality, at least at the unrestricted Hartree–Fock (UHF) level of theory, as documented in Table 11, in spite of the looser constraint the spin density distribution has to comply with in a variational calculation, i.e., that the total spin projection along one direction (Σ_z) be assigned to a constant given value in every cell (Σ_z is $5/2$ and 0 in the ferromagnetic and antiferromagnetic phases of KMnF_3 , respectively). In particular, the ion net charges are close to their formal values ($+2$, -1 , and $+1$ for Mn, F, and K) and the Mn spin moment is close to 5 , with only small polarization of the F anion (see also Figure 27).

The different stability of FM and AFM phases results from the superexchange interaction¹³⁸ along the Mn–F–Mn path and is essentially caused by the different spin polarization of F in the two cases, as shown in Figure 27. Consequently, the corresponding energy differences are expected to be so small that they need to be determined with very high numerical accuracy. In

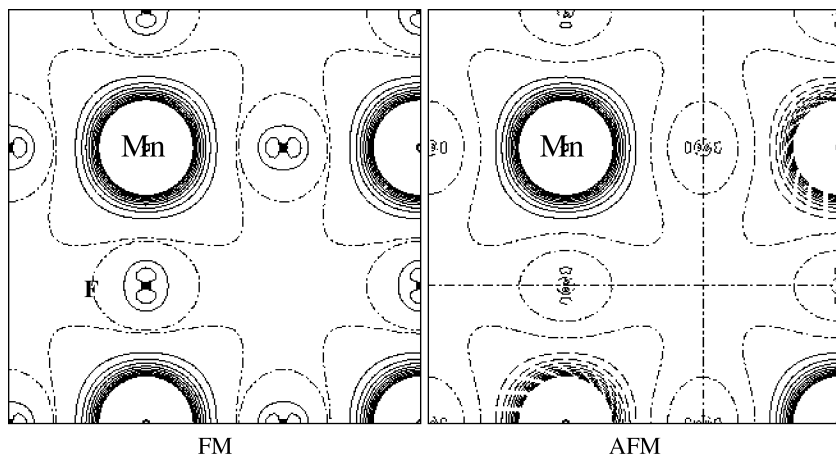


Figure 27 UHF spin density map for the FM and AFM solutions of KMnF_3 on the (001) plane through the Mn and F atoms. The separation between contiguous isodensity lines is 0.01 bohr; the function is truncated in the core region at ± 0.1 bohr. Continuous, dashed, and dot-dashed lines correspond to up-, down-, and zero-spin density, respectively.

Table 12 Total Energy (in Hartree) of the FM and AFM Phases of KMnF_3 as Obtained with Various Hamiltonians

Hamiltonian	E_{FM}	E_{AFM}	ΔE	J
HF	-4095.286164	-4095.286758	1.56	2.50
LDA	-4089.532113	-4089.540105	21.00	33.64
B-LYP	-4101.523522	-4101.531254	20.30	32.56
PBE	-4100.020100	-4100.026538	16.90	27.10
B3LYP	-4101.056636	-4101.060127	9.17	14.70
Exp. [#]				7.30
				7.40

$\Delta E = E_{\text{FM}} - E_{\text{AFM}}$ in kJ/mol. J is the super-exchange coupling constant (in K).

[#]Experimental values from reference 149.

fact, the relative stability of the considered FM phase with respect to the anti-ferromagnetic structures is 0.780 and 0.260 kJ/mol for AFM and AFM', respectively, at the UHF level of theory. The results obtained with different Hamiltonians are compared in Table 12.

ΔE can be used to evaluate the superexchange coupling constant J , which is a measure of the superexchange interaction. A general introduction to the superexchange interaction can be found in Kahn¹⁵⁰ and Yosida.¹⁵¹ According to the Ising model, $\Delta E(\text{FM-AFM})$ and J are related through the following expression:

$$\Delta E = \frac{2zJS_z^2}{k} \quad [76]$$

where z corresponds to the number of nearest Mn transition metal ion neighbors with opposite spin, S_z is the formal S_z of Mn (5/2) and $k = 120.27 \text{ K} \cdot \text{mol} \cdot \text{kJ}^{-1}$ is the conversion factor from kJ/mol to K. The values of J can be compared with the experimental observations, usually fitted to the same Ising model. The UHF value of J is about one third of the experimental value, whereas all DFT functionals provide values that are larger than the experiment¹⁴⁹ and, in the case of LDA, J is overestimated even by a factor of 4.5.

Spin contamination is the main source of error in the evaluation of J , but deviations from the Ising model may also account for part of it. However, despite the large disagreement between the calculated and experimental values of J , the prediction of the relative stability of different magnetic phases is correct. Moreover, investigation of the same properties with the other systems previously mentioned always reproduced phase stabilities correctly and J values were calculated approximately within the same error bar.

Positional Isomorphous Phases

The relative stability of different cation sites in a zeolite framework is one more interesting example of energy difference calculation, in this case

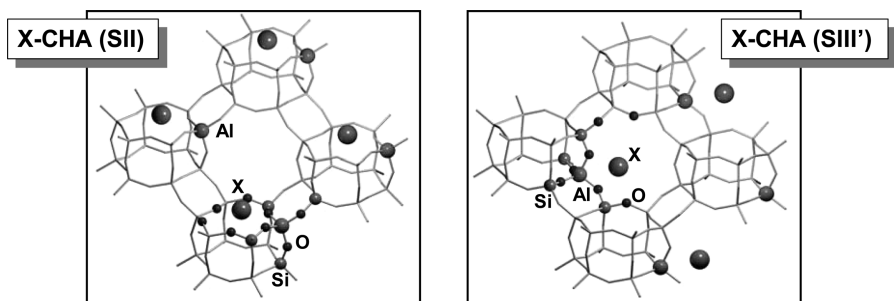


Figure 28 Cation sites in chabazite.

concerning isomorphous crystalline structures with the same composition but a positional difference.

The cation location in a high-silica Al-substituted chabazite¹⁵² has been studied where two possible sites are to be considered (Figure 28) on the basis of the experimental evidence. The SII site corresponds to a cation at the top of a hexagonal prism, whereas for SIII', it is in the eight-member ring. The relative stability of these two sites was computed for a proton and three alkali metal ions: Li, Na, and K at both HF and B3LYP levels of calculation (see Civalleri et al.¹⁵² for details).

In this case, the level of theory is almost irrelevant for evaluating the relative stability of the different sites (Table 13). The proton is preferably predicted at the SIII' site. Li and Na cations are more stable when coordinated on the hexagonal prism (SII), whereas K definitely prefers the eight-member ring site (SIII') for steric reasons.

Energy Derivatives

The interest by computational chemists in the total energy originates from the possibility of comparing different systems or different phases of a given system. The information content of the total energy dependence on the crystal structure permits a wider analysis of the properties of a system. Some examples of observables related to first- and second-order derivatives are listed in Table 14. Beside the search for energy minima, investigating the energy hypersurface is, for example, also a means to go beyond the static

Table 13 Relative Stability (in kJ/mol) of Site SIII' with Respect to the SII Site

	H	Li	Na	K
HF	-11.2	7.9	10.7	-18.3
B3LYP	-6.9	9.2	12.5	-18.1

Table 14 First and Second Order Derivatives of the Total Energy

Differentiating variable	Total energy derivative	Observable
nuclear coordinate	$\left(\frac{\partial E}{\partial \mathbf{r}_i}\right)_T = 0$	equilibrium nuclear coordinates
	$\left(\frac{\partial^2 E}{\partial \mathbf{u}_i \partial \mathbf{u}_j}\right)_{\text{eq}} = k_{ij}$	force constants
lattice parameter	$\left(\frac{\partial E}{\partial \mathbf{a}_i}\right)_T = 0$	equilibrium unit cell
	$\left(\frac{\partial^2 E}{\partial \varepsilon_i \partial \varepsilon_j}\right)_{\text{eq}} = c_{ij}$	elastic tensor
unit cell volume	$\left(\frac{\partial E}{\partial V}\right)_S = -P$	internal pressure
	$\left(\frac{\partial^2 E}{\partial V^2}\right)_{\text{eq}} = B$	bulk modulus

\mathbf{u}_i denotes a nuclear displacement from the equilibrium position, ε_i is a component of the strain tensor, \mathbf{a}_i is a lattice basis vector.

lattice model implicit in the adiabatic approximation and open to lattice dynamical and thermodynamical properties.

We first consider first-order energy derivatives. The calculation of the cohesive energy and of the relative stability of different compounds or phases relies on the hypothesis that the systems involved are all in their respective equilibrium geometries, and that these geometries are to be determined *ab initio*. Thus, the accuracy problem in a calculation of ΔE (see Table 4) cannot be separated from the reliability of a geometry determined with the same method. The analytic calculation of energy gradients with respect to the cell parameters and nuclear coordinates is the most efficient method of finding minima on the total energy hypersurface. As an example, we report the equilibrium lattice parameters (Table 15) that were used to compute the cohesive energies reported in Table 8. The structure of all crystals sampled in the table is simple, with all atoms in a special position (see the subsection on the direct lattice), so that the lattice parameters are the only geometrical variables to be taken into account.

Table 15 shows that in most cases, the percentage deviation from the experimental lattice parameter is below 2%. In general, HF tends to overestimate lattice parameters in nonmetallic systems, whereas LDA shows the opposite trend. The alkali-halide series is more varied in results. For instance, the HF error for the lattice parameter of LiF, NaCl, and KBr increases from about 0% to 8%. This result is a consequence of the increasing importance of

Table 15 Computed Lattice Parameters (in Å) of LiF, NaCl, KBr, MgO, Si, and Be with Different Hamiltonians

	HF	LDA	PW91	B3LYP	CCSD(T)	Exp.
LiF	4.02 (+0.7)	3.93 (-1.5)	4.09 (+2.5)	4.05 (+1.5)	3.99 (0.0)	3.99
NaCl	5.80 (+4.1)	5.50 (-1.3)	5.72 (+2.7)	5.73 (+2.9)	5.63 (+1.1)	5.57
KBr	7.05 (+8.0)	6.60 (+1.1)	6.92 (+6.0)	6.94 (+6.3)	6.65 (+1.8)	6.53
MgO	4.21 (+0.2)	4.18 (-0.4)	4.26 (+1.4)	4.24 (+1.0)	4.18 (-0.5)	4.20
Si	5.52 (+1.7)	5.42 (-0.2)	5.48 (+0.9)	5.50 (+1.3)	5.42 (-0.2)	5.43
Be	2.28 (-0.4)	2.21 (-3.5)	2.24 (-2.2)	2.24 (-2.2)		2.29
	3.55 (-1.1)	3.49 (-2.8)	3.53 (-1.7)	3.52 (-1.9)		3.59

Percentage difference between calculated and experimental data is given in parentheses. All the crystals are cubic, with the exception of Be, which is hexagonal and whose cell is defined in terms of two lattice parameters, a and c .

omitted correlation effects with increasing atomic number. For MgO, all Hamiltonians give reasonable lattice parameters, because the electrostatic interaction is about four times larger than for alkali halides (approximately +2 instead of +1 charges on the cation).

Thermodynamic implications also exist in energy derivatives. For example, one of the basic equations of thermodynamics relates pressure to the rate of energy change with the unit cell volume at constant temperature:

$$P = -\left(\frac{\partial E}{\partial V}\right)_T \quad [77]$$

Pressure is an important variable in condensed matter, because the structural modifications crystals undergo by the action of pressure are usually much larger than the modifications from thermal expansions or contractions. Moreover, the structure and stability of high-pressure phases is of particular interest in Earth science. This is an application where ab initio modeling can play an important role and help experimentalists to understand the behavior of minerals in the Earth's mantle. The knowledge of pressure enables investigation of phase stability and transitions. In fact, enthalpy is immediately obtained from the total energy by

$$H = E + PV \quad [78]$$

At $T = 0$ K, where any transformation of a pure substance tends to be isentropic, phase stability can be related to the enthalpy and a phase transition occurs at those points in the phase diagram where two phases have equal enthalpy. From the computational point of view, it is possible to explore a range of crystalline volumes by isometric lattice deformations and obtain the corresponding values of pressure and, consequently, of enthalpy. It is intended that nuclei are allowed to relax to their equilibrium geometry after

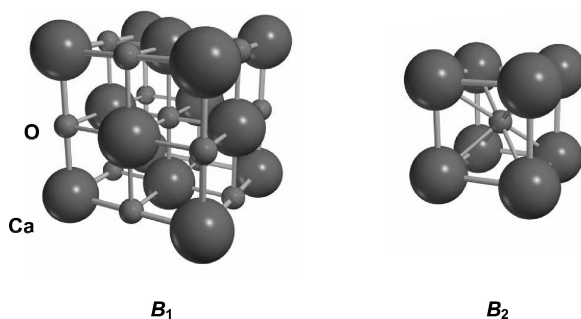


Figure 29 $B_1(Fm\bar{3}m)$ and $B_2(Pm\bar{3}m)$ crystalline phases of CaO.

every lattice deformation. We illustrate this point with a simple example: calcium oxide. CaO presents two polymorphic cubic phases (Figure 29). B_1 corresponds to a face-centered cubic lattice with calcium in a six-fold coordination environment, and B_2 corresponds to a primitive cubic lattice with every Ca coordinated to eight oxygen ions. We consider the following phase transition of CaO:¹⁵³



As occurs with other observables, the range of the calculated phase transition pressure (P_t) and volumes (Table 16) also depends on the choice of the Hamiltonian to some extent. However, the overall agreement with experimental measurements is fairly good.

By interpolating the results of a series of total energy calculations in a range of different lattice volumes, the curves of enthalpy (Figure 30) and the V vs P isothermal (Figure 31) can be plotted in any pressure range easily.

Table 16 Phase Transition Pressure, P_t (GPa), and Volumes, V_{B_1} and V_{B_2} (\AA^3) Calculated with Different Hamiltonians

Hamiltonian	P_t	V_{B_1}	V_{B_2}
HF	69.2	21.2	19.0
LDA	57.2	20.6	18.5
PW91	66.1	20.8	18.8
B3LYP	72.7	20.6	18.6
Exp.	60.0 ^a	—	—
	65.0 ^b	—	—
	63.0 ^c	20.7 ^c	18.7 ^c

^aTaken from Richet et al.¹⁵⁴

^bTaken from Jeanloz et al.¹⁵⁵

^cTaken from Mammone et al.¹⁵⁶

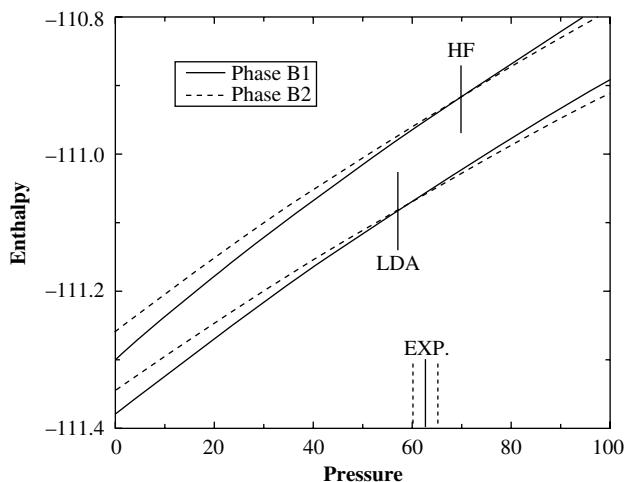


Figure 30 Hartree-Fock and LDA enthalpy of the B_1 and B_2 phases of CaO.

For an application on the phase stability of various TiO_2 polymorphs, see references 157,158.

Other observables also depend on the total energy derivatives, in particular on second-order derivatives, such as the bulk modulus, the elastic constants, and lattice vibration frequencies.

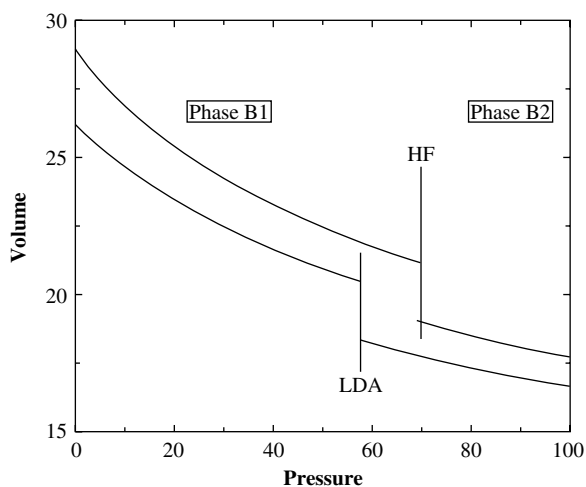


Figure 31 Isothermal phase diagram of CaO (volume, \AA^3 , versus pressure, GPa), as obtained with HF and LDA approximations. Vertical lines represent the transition pressure.

The bulk modulus, B , which measures the response of a crystal to isotropic lattice expansion or compression, is related to the second-order derivative of the total energy with respect to the volume, V , evaluated at the equilibrium volume V_0 :

$$B = -V \left. \frac{\partial^2 E}{\partial V^2} \right|_{V_0} \quad [80]$$

Conversely, the anisotropic response of a crystal to a mechanical force can be described by the elastic constants, C_{ij} , which are defined as the second derivatives of the total energy with respect to the components i and j of the strain tensor, ε :

$$C_{ij} = \frac{1}{V} \frac{\partial^2 E}{\partial \varepsilon_i \partial \varepsilon_j} \quad [81]$$

They provide a full description of the mechanical properties of crystalline materials. B is related to the elastic tensor.¹⁵⁹ In the case of a cubic system, where only three independent components of the elastic tensor differ from zero, B can be obtained from C_{11} and C_{12} as

$$B = \frac{C_{11} + 2 C_{12}}{3} \quad [82]$$

In many computational codes, second derivatives are evaluated numerically (this is also the case of CRYSTAL). This evaluation requires high numerical accuracy in the determination of the total energy. In particular, the lattice deformations involved in calculating lattice constants, which generally reduce the local symmetry, make basis set flexibility (additional sp shells, polarization functions, and so on) necessary. Consequently, a good basis set for the determination of total energy and lattice parameters may be inadequate for the more demanding estimation of these second derivatives.

The effect of the basis set on the bulk properties of MgO is documented in Table 17. Basis set (c), as containing three valence sp shells at oxygen, two

Table 17 Basis Set Effects on Bulk Properties of MgO at the HF Level of Theory

Case	Basis Set	a	B	C_{11}	C_{12}	C_{44}	ΔE^{atoms}
a	8-61/8-51	4.190	200	391	103	201	-715.4
b	8-511/8-411	4.205	181	352	95	188	-699.5
c	8-511*/8-411*	4.194	184	334	108	186	-706.2
Exp.	—	4.195	167	314	94	160	-989.8

a (in Å) is the lattice parameter; B , C_{11} , C_{12} , and C_{44} (in GPa) denote bulk modulus and elastic constants. The cohesive energy ΔE^{atoms} is in kJ/mol.

at magnesium, and a set of polarization functions at both ions, can be considered as nearly complete. The table shows that the basis set quality, which has a relatively small influence on ΔE^{atoms} , becomes more important in the calculation of B and the elastic constants. The addition of d polarization functions is particularly important when computing elastic constants, because the related lattice deformation corresponds to lowering point symmetry. The ions undergo dipolar relaxation, for which the combination of p- and d-type orbitals is required.

Second-order derivatives of energy with respect to the nuclear coordinates are involved in lattice dynamics. Many interesting physical properties¹⁰⁵ are related to lattice dynamics such as vibration spectra (e.g., infrared, Raman, neutron-diffraction), specific heat, thermal expansion, heat conduction, electron-phonon interaction (e.g., superconductivity), and interaction of radiation with matter (e.g., reflectivity of ionic crystals, inelastic scattering of light). The decoupling of the nuclear from the electronic motion through the adiabatic approximation of Born and Oppenheimer¹⁶⁰ and the hypothesis of harmonicity are usually the basic assumptions made when computing lattice dynamics. Within these approximations, force constants relative to all pairs of nuclei in the lattice can be computed as second derivatives of the total energy with respect to small oscillations \mathbf{u} of the nuclei about their equilibrium positions

$$H_{ij}^{\mathbf{g}} = \left(\frac{\partial^2 E}{\partial \mathbf{u}_i^0 \partial \mathbf{u}_j^{\mathbf{g}}} \right)_{\text{eq}} \quad [83]$$

Equation [83] defines one element of the Hessian matrix relative to the oscillations along the i -th coordinate of atom A in the 0-cell and along the j -th coordinate of atom B in the \mathbf{g} -cell (one of the atoms can always be considered in the 0-cell because of the lattice translation invariance). The Hessian matrix of a crystal obviously has infinite size. However, energy derivatives have the same periodicity as does the potential energy, i.e., the periodicity of the lattice. Therefore, the nuclear wave functions describing nuclear oscillations in the lattice must also obey the Bloch theorem, and application of the periodic boundary conditions allows us to represent the Hessian matrix in the reciprocal space, just as in the case of the electronic Schrödinger equation. Thus, the problem is again reformulated by calculating an infinite set of finite-sized square matrices of dimension $3N$, with N being the number of atoms per unit cell, each corresponding to a particular pattern of displacements of the N nuclei in any direction in space. Each matrix is associated with a particular \mathbf{k} point in the reciprocal space and is obtained from Fourier transforming Eq. [83]

$$H_{ij}(\mathbf{k}) = \sum_{\mathbf{g}} e^{i\mathbf{k}\cdot\mathbf{g}} H_{ij}^{\mathbf{g}} \quad [84]$$

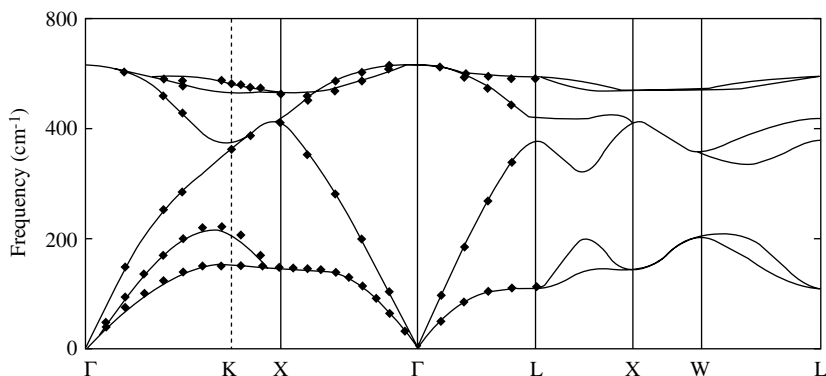


Figure 32 Phonon dispersion of Si from ab initio calculations. Experimental data are denoted by diamonds. Reproduced with permission from reference 161.

Harmonic vibration frequencies are then obtained from diagonalizing the Hessian matrix scaled by the nuclear masses for a convenient sample of reciprocal space points:

$$\Omega_{ij}(\mathbf{k}) = \frac{H_{ij}(\mathbf{k})}{\sqrt{M_i M_j}} \quad [85]$$

Also vibration frequencies, like one-electron energies, then depend on the wave vector \mathbf{k} and $3N$ modes at each \mathbf{k} exist, forming branches. Branches $\omega_1(\mathbf{k}), \omega_2(\mathbf{k}), \dots, \omega_{3N}(\mathbf{k})$ are called *phonon frequencies*, and the relationship between ω and \mathbf{k} determines the *phonon dispersion*. The computed phonon dispersion of Si is presented in Figure 32 as an example.

Three branches have zero frequency at the Γ point and are associated with the translation of the entire crystal along any direction in space. These branches are called *acoustic* modes as the corresponding vibrations behave as acoustic waves. All other branches show finite nonzero frequencies at Γ and are known as *optical* modes, because they correspond to unit-cell dipole moment oscillations that can interact with an electromagnetic radiation. Acoustic and optical modes can be identified clearly in Figure 32.

The dispersion relation contains the most important information concerning vibration normal modes in a crystal. Lattice vibrations can be measured experimentally by means of classical vibration spectroscopic techniques (infrared and Raman) or neutron inelastic scattering. However, only the latter technique allows one to measure the full spectrum in a range of \mathbf{k} vectors, whereas with infrared and Raman spectroscopy, only lattice vibrations at Γ can be detected. This limitation for measuring phonon dispersions is serious, because neutron scattering experiments are demanding.

Once the dispersion relation is known, thermodynamic functions can be calculated on the basis of statistical mechanics equations.⁵⁷ As an example, the Helmholtz free energy, F , can be obtained as:

$$\langle F_{\text{vib}} \rangle = \sum_{n,k} \left\{ \frac{1}{2} \hbar \omega_{nk} + k_B T \ln \left[1 - \exp \left(-\frac{\hbar \omega_{nk}}{k_B T} \right) \right] \right\} \quad [86]$$

where the sum is extended to all lattice vibrations, ω_{nk} , and k_B is the Boltzmann's constant. Another way of computing thermodynamic functions is based on the use of the phonon density of states. The evolution of the crystal structure as a function of temperature and pressure can also be simulated by minimizing $G = F + pV$. The procedure requires a sequence of geometry optimizations, and lattice vibration calculations.

Although the ab initio calculation of vibrational frequencies of molecular systems is a well-known practice, it is not so common in the case of crystalline systems. However, quantum-mechanical calculation of lattice vibrations and phonon spectra has become a subject of increasing interest and effective methods have been developed and implemented. In this respect, a recent review by Baroni et al.¹⁶² gives a detailed overview of the state of the art of ab initio calculation of vibrations and related properties for crystalline materials. Most of the current implementations are based on DPPT and use either plane waves^{162,163} or localized functions as a basis set.¹⁶⁴ As an example, calculated and experimental vibration frequencies at Γ are reported in Table 18 for

Table 18 Calculated and Experimental Vibration Frequencies (cm^{-1}) of α -quartz at Γ

Symmetry	HF ^a	LDA ^a	LDA ^b	LDA ^c	B3LYP	Expt. ^d
A_1	216.7	261.6	193.7	238.9	216.0	219.0
	381.3	332.3	355.0	339.3	350.4	358.0
	504.9	482.1	460.1	461.7	465.1	469.0
	1144.4	1089.1	1123.3	1061.0	1085.4	1082.0
A_{2T}	395.4	326.3	366.4	341.3	352.3	361.3
	544.1	504.6	489.3	493.4	500.9	499.0
	823.4	791.1	792.2	762.4	783.8	778.0
	1132.4	1086.4	1115.4	1056.5	1076.4	1072.0
A_T	138.8	143.4	120.9	133.3	132.5	133.0
	286.5	263.5	257.3	261.3	263.6	269.0
	427.4	376.9	390.0	377.6	391.3	394.5
	490.6	443.8	448.0	443.8	447.0	453.5
	740.9	721.7	703.3	690.8	702.9	698.0
	847.7	835.0	809.6	791.7	810.5	799.0
	1125.2	1070.3	1108.7	1045.0	1068.2	1066.0
	1235.8	1141.7	1190.8	1128.1	1163.1	1158.0

^aTaken from reference 165.

^bTaken from reference 60.

^cTaken from reference 166.

^dTaken from reference 167.

α -quartz. The average error evaluated with respect to the experimental frequencies is 39.9, 16.6, 16.5, 12.6, and 4.7 cm^{-1} for the HF, the three LDA, and the B3LYP calculations reported in the table, respectively. B3LYP harmonic frequencies exhibit a fairly good agreement with the corresponding absorptions observed in the experimental spectrum. On the contrary, the HF energy hypersurface curvature is known to be incorrect, and this leads to a regular overestimation of vibration frequencies. LDA results are better than HF but worse than B3LYP. Large differences, however, exist among the three sets of LDA data in Table 18, which represent an interesting example of how results may depend on the particular implementation of a method.

MODELING SURFACES AND INTERFACES

In nature, crystals are not infinite but finite macroscopic three-dimensional (3-D) objects terminated by surfaces. Many phenomena and processes occur at the interface between a condensed phase and the environment. Modeling surfaces is then of great theoretical and practical interest.

A surface can be created by cutting a crystal, which we simulate as an infinite object, through a crystalline plane. Two semi-infinite crystals are then generated containing an infinite number of atoms in the direction orthogonal to the surface, where periodicity, which is essential for applying the Bloch theorem, is lost. We then need further approximations to be able to treat this problem, for which alternative methods have been proposed such as those based on (2-D) clusters, embedded clusters, or slabs. We will focus here on the two-dimensional (2-D) *slab model*.

The Slab Model

The slab model consists of a film formed by a few atomic layers parallel to the (*hkl*) crystalline plane of interest. The film, of finite thickness, is limited by two surface planes, possibly related by symmetry. For sufficiently thick slabs, this kind of model can provide a faithful description of the ideal surface. The adequacy of the model must be checked by considering convergence of geometry, energy, and electronic properties with an increasing number of atomic layers included in the slab.

In actual calculations, two different schemes can be envisaged to deal with a slab model:

1. By imposing 2-D periodic boundary conditions. The slab model is really two-dimensional, with a 2-D unit cell (Figure 33*a*).
2. By forcing a 3-D periodicity (3-D slab model). The three-dimensional system consists of an array of slabs of selected thickness along one direction, separated by vacuum zones, as shown in Figure 33*b*. The vacuum

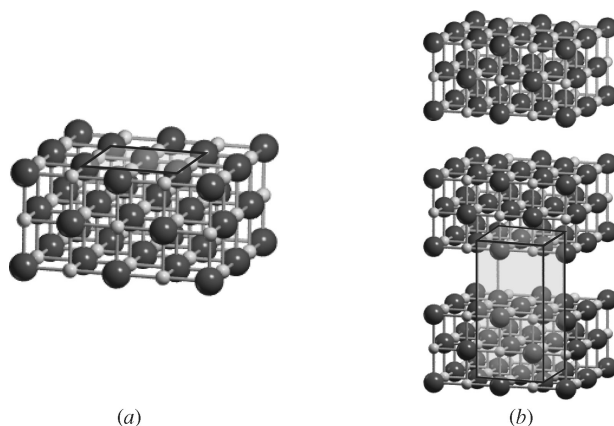


Figure 33 Three-layer slab models of the MgO (100) surface. (a) With 2-D periodic boundary conditions. (b) 3-D supercell approximation of the slab model as adopted in plane wave calculations.

zones must be large enough for the fictitious interactions between slabs to be negligible.

When we use a plane wave basis set, which requires a 3-D Fourier representation of many intermediate quantities, such as the charge density, only model (b) can be adopted. On the contrary, when a local basis set is adopted, no problems occur in the implementation of both schemes.

In a recent paper,¹⁶⁸ 2-D and 3-D slab models have been compared. The (110) surface of rutile TiO₂ served as a case study. Calculations were carried out with CRYSTAL at the HF level with a Gaussian basis set. The convergence of the calculated surface energy and Fermi level was investigated as a function of the slab thickness and interslab vacuum gap. It was found that 2-D and 3-D slabs provide similar convergence with the slab thickness when the vacuum gap is larger than 6.0Å. However, model (a) is more general and is to be preferred, for example, in the simulation of an adsorption process, where attention must be paid to spurious interactions among periodic replicas along the direction perpendicular to the slab.

Specifying the Surface Plane—Miller Indices

The surface is identified by three integers (hkl)—the so-called Miller indices. The three indices specify a plane of atoms in the crystal by means of the components of a vector perpendicular to that plane. Planes parallel to crystallographic axes YZ , XZ , and XY are indicated as ($h00$), ($0k0$), and ($00l$), respectively. The planes closest to the origin are then identified by the normal vector with the smallest indices: (100), (010), and (001). Planes

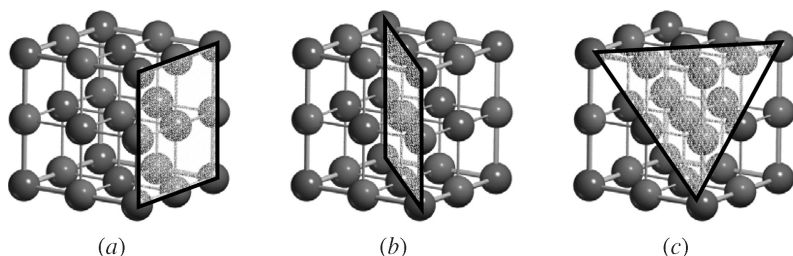


Figure 34 Three types of planes in the MgO crystal: (a) 100, (b) 110, and (c) 111.

parallel to one of the three axes X , Y , or Z are defined by $(0kl)$, $(b0l)$, or $(bk0)$, and so on. Some examples for MgO are shown in Figure 34.

Choosing the Surface Termination

The most interesting surfaces are generally those with low indices, because their creation requires, as a rule, a smaller amount of energy and are, therefore, the most commonly observed. However, not all crystalline surfaces are physically stable or worthy of investigation.

For ionic and semi-ionic crystals, a careful analysis of the possible surface terminations has been carried out by Tasker.¹⁶⁹ Given a slab composed of a certain number of repeated units, which are in turn made up of atomic layers parallel to the selected plane, the resulting structure can be classified in one of the three following categories (Tasker's types):

- Type 1: the slab consists of neutral layers with the same stoichiometry of the host crystal.
- Type 2: the slab consists of charged layers arranged symmetrically so that the repeated unit presents no net dipole perpendicular to the surface.
- Type 3: the slab consists of charged layers alternating in such a way that the repeated unit presents a net dipole normal to the surface.

Although type 1 and 2 surfaces may exist, those of type 3, also referred to as dipolar surfaces, are unstable and can only be stabilized through some mechanism to remove the macroscopic field (i.e., by reconstruction, molecular adsorption, and so on). In the MgO case (see Figure 35), the (100) and (110) surfaces correspond to type 1, whereas the (111) surface is type 3.

In covalent solids, the creation of a surface requires cutting covalent bonds, which means that dangling bonds would be present at the surface. The resulting instability is partly reduced either by creating new bonds, giving rise to a reconstruction of the surface, or chemisorbing atoms from the environment (e.g., H, Cl). The saturation of dangling bonds by chemisorption is important, for example, in silicates. When a surface is cut out from the

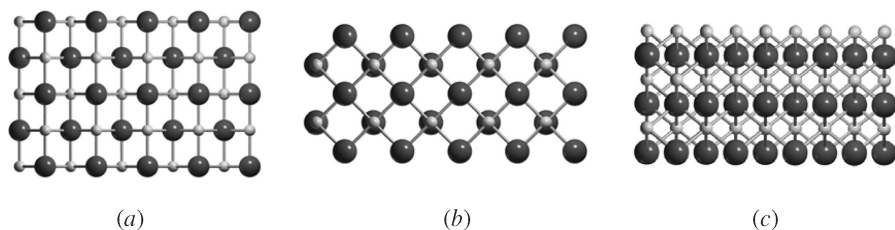


Figure 35 Five-layer slab model of MgO surfaces (lateral view): (a) (100) surface—type 1, (b) (110) surface—type 1, and (c) (111) surface—type 3.

bulk, unstable $\text{Si-O}\cdot$ radicals at the surface react readily with water to give a fully hydroxylated surface with hydrophilic character.

When cutting molecular crystals, the molecular topology must be preserved and only intermolecular bonds are cut. If the molecule has a dipole moment, attention must be paid to the surface termination, because the slab can possess a net dipole perpendicular to the surface. For instance, ice XI, a proton-ordered phase of ice, is ferroelectric because its basic repeating unit, consisting of four water molecules, has a net dipole along the *c*-axis (see Figure 36 on the left).

Thus, by cutting a slab parallel to the (001) face, a dipolar surface is created that would be highly unstable,¹⁷⁰ according to Tasker's classification. Figure 36, on the right, shows that the electrostatic potential difference between the two surfaces is large, which explains their instability. A stable slab of C-ice can be obtained only by cutting the crystal in such a way that the ferroelectric axis is parallel to the surface, which is equivalent to selecting the (010) surface.

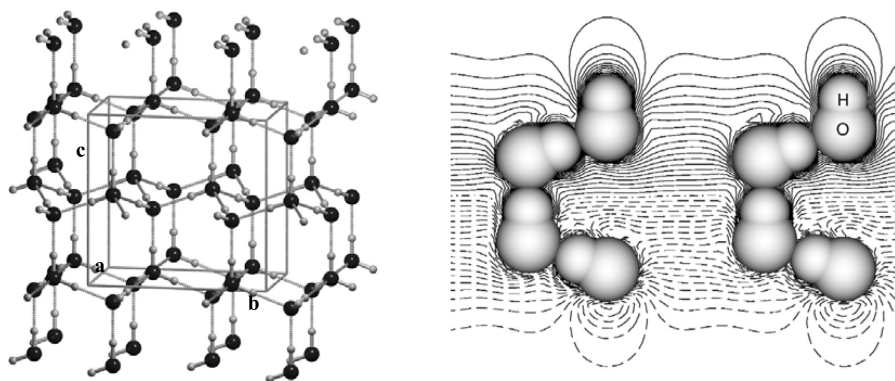


Figure 36 On the left: Structure of ice XI; On the right: Electrostatic potential at the (001) surface of ice XI. Consecutive isodensity lines differ by 0.01 a.u.; continuous, dashed, and dot-dashed curves correspond to positive, negative, and zero potential, respectively. Isopotential lines corresponding to potential values larger than 0.2 a.u. in module are not plotted.

Even if it may appear unrealistic, because of the electric strain parallel to the surface, it comes out that this structure is particularly stable.¹⁷⁰

Surface Formation Energy and Stability

Within the slab model approach, the surface formation energy is computed as

$$\Delta E_{\text{surf}}^n = \frac{(E^n - nE_{\text{bulk}})}{2A} \quad [87]$$

where E^n is the energy of an n -layer slab, E_{bulk} is the energy of a single layer's worth of bulk material, and A is the area of the primitive surface unit cell. The factor $1/2$ accounts for the existence of two limiting surfaces. ΔE_{surf}^n is then the energy per unit area required to form the surface from the bulk, and it is intrinsically a positive quantity (if not, the bulk would exfoliate). As more layers are added in the calculation by increasing the slab thickness ($n \rightarrow \infty$), ΔE_{surf}^n will converge to the surface formation energy per unit area. This important check should be performed, when studying surfaces.

For MgO, which is a wide band gap insulator, the computed HF ΔE_{surf}^n converges rapidly, as shown in Figure 37.

In metals or small band gap semiconductors, convergence can be slower and numerical noise larger. In Eq. [87], total energies from 3-D and 2-D systems are used, and this in principle might create problems of “equivalent” accuracy in algorithms that are specific for 2-D and 3-D. As a cross check, we can use the following definition for the surface energy:

$$\Delta E_{\text{surf}}^n = \frac{E^n - n(E^n - E^{n-1})}{2A} \quad [88]$$

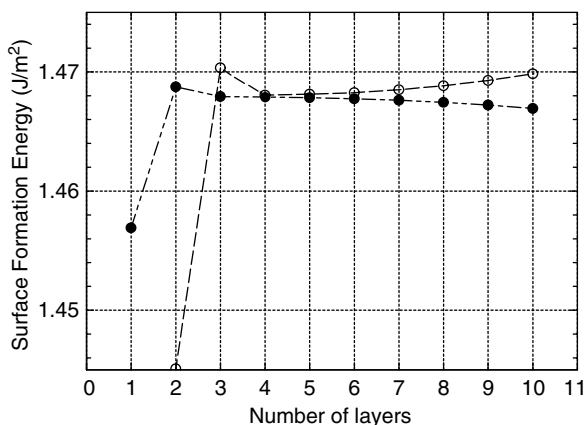


Figure 37 Dependence of the surface energy on the number of layers for a MgO (100) slab model. Filled circles from Eq. [87]; open circles from Eq. [88].

In this expression E_{bulk} has been replaced by $E^n - E^{n-1}$. So the surface formation energy is determined from a series of 2-D calculations. If each additional layer in the slab is seen as the central layer, it is clear that $E^n - E^{n-1}$ should converge to the energy of a single layer in the bulk crystal. In Figure 37, the MgO(100) surface energy computed with Eq. [88] is also reported. A more extensive discussion on the use of Eqs. [87] and [88] when computing the surface energy of metallic lithium, as a case study, can be found in Doll et al.¹⁷¹

When the surface formation energy of different surfaces is available, the relative stability can be evaluated. Surface stability has relevance in determining the crystal morphology, although kinetic effects in many cases can also play an important role. As an example, we can compare the stability of the (100) and (110) MgO surfaces¹⁷² (see Figure 34). When a five-layer slab model is adopted, the computed HF surface energies are 1.47 J/m² and 5.24 J/m². The difference in stability between these two surfaces is easily explained on the basis of the different environment of the surface ions: at the (100) surface Mg and O are fivefold-coordinated, whereas at the (110) surface, coordination decreases to four.

Surface Relaxation and Reconstruction

In general, when a surface is cut out of a perfect crystal, the atoms near the surface will move away from their bulk positions to minimize the surface energy. When the atomic displacements do not change the symmetry of the slab, this is referred to as surface *relaxation*. However, in some systems, the rearrangement is deeper and the surface has a tendency to *reconstruct*; that is, the periodicity of the surface layer changes from that implied by pure bulk termination. If the primitive cell of the surface is defined by lattice vectors \mathbf{a} and \mathbf{b} , then a reconstruction introducing a new periodicity, involving two steps in \mathbf{a} and three steps in \mathbf{b} , is called a (2×3) reconstruction. To model such a phenomenon, the slab model can be combined with the supercell approach by creating a 2-D cell and then enlarging it to introduce the new periodicity. A typical example of surface reconstruction is the (111) and the (100) surfaces of silicon.

At the (100) surface, the presence of highly unstable dangling bonds at the top of the fully unrelaxed surface (indicated in dark in Figure 38a) is partly reduced by the formation of new bonds leading to a (2×1) reconstruction (Figure 38c). A 2-D cell of double size is necessary to model such a reconstruction.

In ionic crystals, reconstruction effects can also be involved in the stabilization of polar surfaces (Tasker's type 3). For instance, the (100) surface of the fluorite-type crystal of Li₂O becomes stable if half of the Li atoms are moved from the bottom face of the slab to the top face above the oxygen atoms to produce a zero-dipole structure (Figure 39). In fact, this kind of surface has been observed experimentally.¹⁷³

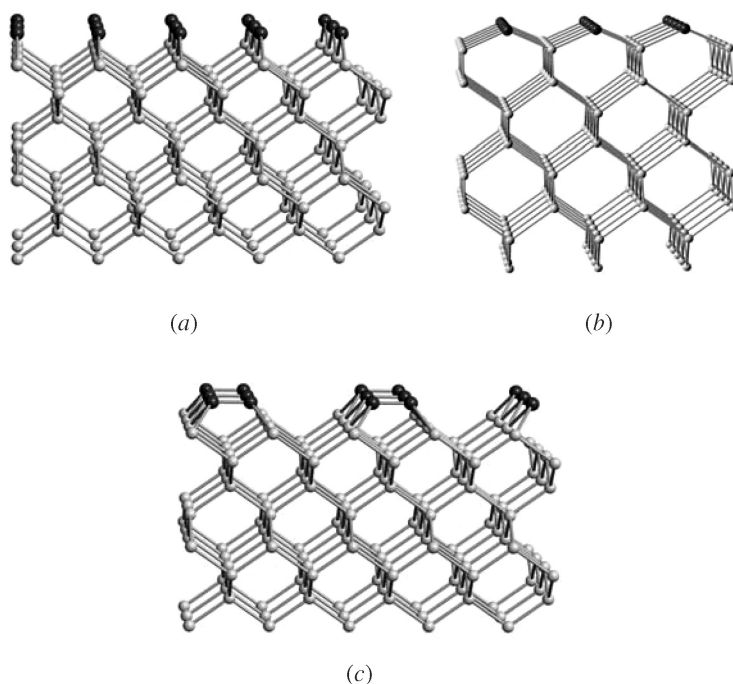


Figure 38 Pictorial view of the (100) surface of silicon. (a) unrelaxed surface; (b) relaxed surface and (c) (2×1) reconstructed surface.

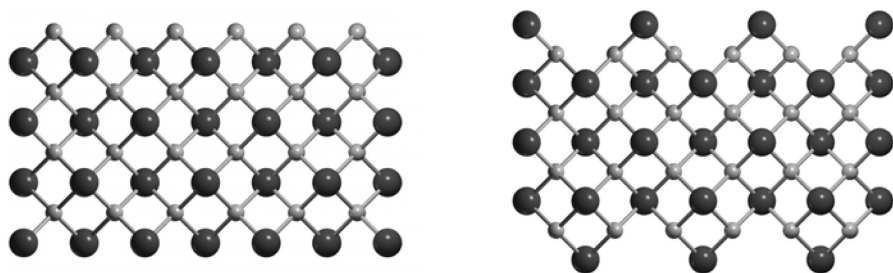


Figure 39 Lateral view of the (100) surface of Li_2O . On the left: unreconstructed dipolar surface. On the right: reconstructed zero-dipole surface.

Relaxation effects are particularly significant in partially-ionic oxides like $\alpha\text{-Al}_2\text{O}_3$. Alumina is of enormous technological importance and is widely used by chemists as a support material in most heterogeneous catalysts. The simplest surface is the Al-terminated (0001) one, which corresponds to the basal plane. As shown in Figure 40 on the left, the basic repeated unit perpendicular to the (0001) surface is a three-layer slab consisting of Al-3O-Al atomic layers, where 3O indicates a layer containing three oxygens per 2-D cell. In the

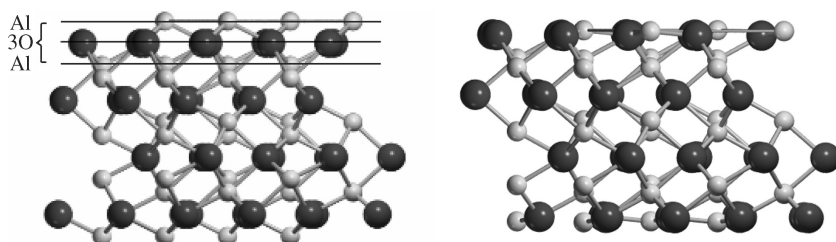


Figure 40 A 12-layer slab model of the Al-terminated (0001) surface of α - Al_2O_3 . Lateral view of the unrelaxed structure (left) and the relaxed structure (right).

unrelaxed slab model, the topmost layer consists of undercoordinated Al ions, as is shown in Figure 40. Consequently, this is an unfavorable structure and the Al atom undergoes a large relaxation (compare left and right pictures in Figure 40). In particular, the first-to-second interlayer spacing largely contracts to lower the surface energy. For a 15-layer slab model, the contraction is as large as -78.8% at HF, and it increases further when DFT methods are adopted: -87.1% and -79.2% , with SVWN and BLYP methods, respectively.

Structural relaxation has also significant effects on the relative stability of different surfaces. For α - Al_2O_3 , five different low-index nonpolar faces are usually believed to be competitive for stability.¹⁷⁴ At the HF level of theory,¹⁷⁵ the stability order is as follows:

$$\begin{array}{l} \text{Unrelaxed: face} \quad (01\bar{1}2) < (11\bar{2}0) < (10\bar{1}1) < (10\bar{1}0) < (0001) \\ \Delta E_{\text{surf}}^n (\text{J/m}^2) \quad 2.70 \quad 3.27 \quad 4.18 \quad 4.50 \quad 4.85 \end{array}$$

$$\begin{array}{l} \text{Relaxed: face} \quad (0001) < (10\bar{1}2) < (11\bar{2}0) < (10\bar{1}0) < (10\bar{1}1) \\ \Delta E_{\text{surf}}^n (\text{J/m}^2) \quad 1.90 \quad 2.00 \quad 2.37 \quad 2.42 \quad 2.47 \end{array}$$

These data show that the inclusion of structural relaxation has a dramatic effect: The stability order is almost completely reversed, and the surface formation energy spans a much more narrow range of values with respect to the unrelaxed data. Relaxation is then important. For example, the (0001) surface, which is the most unstable unrelaxed face, becomes the most stable when relaxation is taken into account. It is worth noting that slab models with more than 20 atomic layers are required to reach full convergence on stability order. The computed trend for the unrelaxed surfaces is close to that obtained from classical simulations within a fully ionic model by Tasker¹⁷⁴ and Mackrodt,¹⁷⁶ whereas the three sets differ after relaxation:

$$\begin{array}{l} \text{Unrelaxed: Tasker} \quad (01\bar{1}2) < (11\bar{2}0) < (10\bar{1}1) < (0001) < (10\bar{1}0) \\ \text{Mackrodt} \quad (01\bar{1}2) < (11\bar{2}0) < (10\bar{1}1) < (0001) < (10\bar{1}0) \end{array}$$

$$\begin{array}{l} \text{Relaxed: Tasker} \quad (01\bar{1}2) < (11\bar{2}0) < (10\bar{1}0) < (0001) < (10\bar{1}1) \\ \text{Mackrodt} \quad (0001) < (10\bar{1}0) < (01\bar{1}2) < (11\bar{2}0) < (10\bar{1}1) \end{array}$$

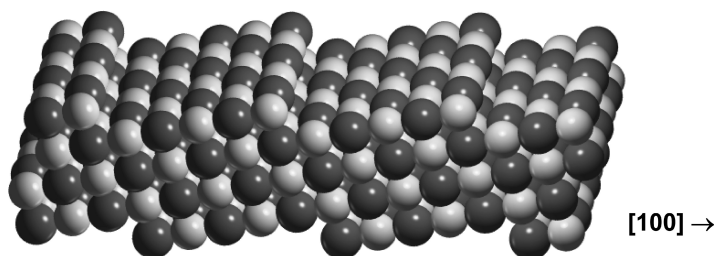


Figure 41 MgO (501) slab model with steps along the [100] direction.

The difference between classical and quantum-mechanical calculations is caused by the important role played by electronic rearrangement.

Vicinal Surfaces—Modeling Steps and Kinks

Real surfaces are rarely atomically flat. Typically, a surface will be covered in plateaus, with edges and corners. Within the slab model, the use of *vicinal* surfaces (those cut at an angle slightly different to that of the low-energy surface) is a useful trick to model steps and kinks. For example, Figure 41 shows a few unit cells of the (501) surface of MgO, which contains a sequence of steps in the [100] direction. These faces may mimic situations occurring at defective ionic surfaces and can therefore be used to investigate the reactivity of different kinds of defects. For instance, it has been found¹⁷⁷ that heterolytic splitting of hydrogen [$\text{H}_{2(\text{g})} \rightarrow \text{H}_{(\text{ads})}^+ + \text{H}_{(\text{ads})}^-$] may take place with low activation energy and favorable energy balance at a (*n*01) face of MgO with $n \geq 3$, which simulates a regular step at a (100) surface.

Ab initio calculations on bare surfaces are now sufficiently accurate and efficient; we propose a (certainly not exhaustive) list of surface studies performed with the CRYSTAL code: halides (LiF,^{178,179} NaCl,¹⁸⁰ CaF₂^{181,182}), oxides (α -Al₂O₃,^{183–186} CeO₂,¹⁸⁷ α -Cr₂O₃,¹⁸⁸ Li₂O,¹⁸⁹ MgO,^{172,190} SnO₂,¹⁹¹ TiO₂,^{192,193} ZnO,^{194–196} ZrO₂^{184,187}), sulphides (Li₂S,¹⁹⁷ FeS₂,¹⁹⁸ PbS,¹⁹⁹ RuS₂²⁰⁰), metals (Li,¹⁷¹ Cu,^{201,202} Ag,^{203,204} Ni,²⁰⁵ Pt²⁰⁶), perovskites (BaTiO₃,²⁰⁷ LaMnO₃,²⁰⁸ SrTiO₃^{209,210}), molecular crystals (water ice²¹¹), and silicates.²¹²

Adsorption on Surfaces

An appropriate slab model of a surface is also useful to study the adsorption of atoms or molecules. Both physisorption and chemisorption processes can be modeled easily.

The binding energy between surface and adsorbate, ΔE , is a key observable. It corresponds to the process in which the molecules move from an ideal

gas state onto the surface, and it is defined as

$$\Delta E = E(\text{slab}) + N \cdot E(\text{mol}) - E(\text{slab}/\text{ads}) \quad [89]$$

where $E(\text{mol})$ is the energy of one isolated adsorbed molecule and N is the number of adsorbed molecules per unit cell. These energies are defined per unit cell and are negative.

ΔE can also be written as the sum of two contributions:

$$\Delta E = \Delta E_{\text{ads}} + \Delta E_{\text{L}} \quad [90]$$

The first contribution is the binding energy per unit cell per adsorbed molecule and is defined as

$$\Delta E_{\text{ads}} = E(\text{slab}) + E(\text{ads}) - E(\text{slab}/\text{ads}) \quad [91]$$

where $E(\text{slab}/\text{ads})$ is the total energy of the slab in interaction with the periodic array of adsorbed molecules, $E(\text{slab})$ is the energy of the slab alone, and $E(\text{ads})$ is the energy of the periodic array of adsorbed molecules without the underneath solid surface. ΔE_{L} is the lateral interaction energy, per unit cell, among the adsorbate molecules, i.e., without the underneath surface, and can be either positive (repulsion) or negative (attraction), depending on the nature of the ad-molecules. In the limit of low coverage, i.e., large distances between molecules, ΔE_{L} tends to zero, so that $\Delta E_{\text{ads}} \sim \Delta E$.

Modeling different coverages is of interest in adsorption processes and can be achieved easily by enlarging the underlying surface unit cell (i.e., within a supercell approach), so that the density of adsorbed molecules can be increased or reduced. In the limit of low coverage, lateral interactions tend to vanish and adsorbed molecules can be considered as isolated.

If the basis set is not complete, the computed binding energy per adsorbed molecule should be corrected for the BSSE following the CP method as proposed for molecular complexes. Therefore, the BSSE corrected binding energy $\Delta E_{\text{ads}}^{\text{C}}$ becomes

$$\Delta E_{\text{ads}}^{\text{C}} = E(\text{slab}/[\text{ads}]) + E([\text{slab}]/\text{ads}) - E(\text{slab}/\text{ads}) \quad [92]$$

in which $E(\text{slab}/[\text{ads}])$ and $E([\text{slab}]/\text{ads})$ are, respectively, the energy of the slab with the basis functions of the adsorbate only, and vice versa.

Let us consider, as an example, the interaction of carbon monoxide with the MgO (100) surface. This system has been the subject of several simulations where cluster and periodic models have been used (see Damin et al.²¹³ and references therein). Here we focus on a periodic approach through a slab model.

The MgO (100) surface is modeled by a three-layer slab. As shown above (Figure 37), the adopted slab is thick enough to ensure good convergence of

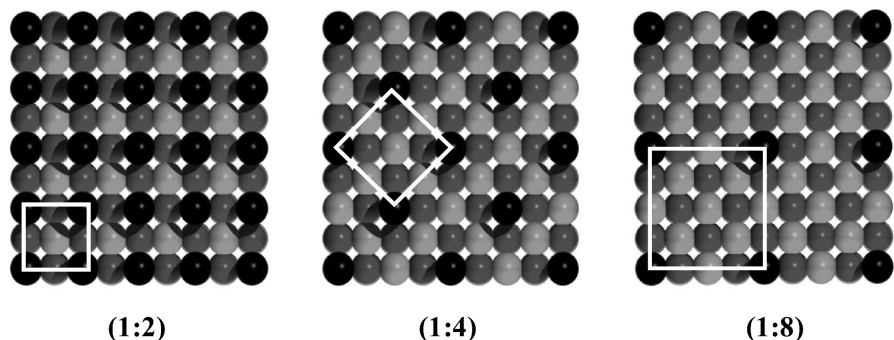


Figure 42 Pictorial view of the CO/Mg (100) system at different CO coverages. Light and dark gray spheres are Mg and O, respectively; black spheres represent the CO molecules.

the surface energy. Three different CO coverages have been considered, namely the (1:2), (1:4), and (1:8) (here (1: n) means that adsorption involves one CO molecule per n Mg²⁺ ions), in order to study the effect of the lateral interactions on ΔE . Preliminary calculations indicate that the adsorption through the oxygen atom is disfavored in comparison with that via the carbon atom, so it will not be considered in the following discussion. The resulting 2-D unit cell are shown in Figure 42.

The CO molecules were adsorbed at both faces of the MgO (100) slab model. Calculations were carried out at the HF and DFT levels. For the latter, the B3LYP method was adopted. Two basis sets were employed, hereafter indicated as A and B, with B being more accurate and costly than A. For more details concerning the all-electron basis sets and optimized geometry, see Damin et al.²¹³

Table 19 shows the HF and B3LYP computed binding energies. ΔE is small at both levels of theory, with a value of about 10 kJ/mol at the best B3LYP/B level. The BSSE correction is large: ΔE^C is nearly null at HF/A, around 2.0 kJ/mol at B3LYP/A and 3.7 kJ/mol at B3LYP/B for the (1:4)

Table 19 ΔE (kJ/mol) of CO Adsorbed on the MgO (100) Surface as a Function of CO Coverage, Hamiltonian and Basis Set

Method	HF/A			B3LYP/A			B3LYP/B	
	(1:2)	(1:4)	(1:8)	(1:2)	(1:4)	(1:8)	(1:2)	(1:4)
ΔE	6.2	6.4	6.4	13.6	14.0	14.0	9.1	10.3
ΔE^C	0.9	0.8	0.7	2.8	3.0	2.0	3.0	3.7
ΔE_L	2.4	0.6	0.1	1.6	0.4	0.1	2.6	0.4
ΔE_N	-1.5	0.2	0.6	1.2	2.6	1.9	0.4	3.3

ΔE^C is corrected for BSSE. ΔE_L is the lateral interaction and $\Delta E_N = \Delta E_C - \Delta E_L$ is the net binding energy.

coverage. The lateral interaction energy, ΔE_L , is important only when the smallest cell (1:2) is used. The final binding energy at the B3LYP/B level for the (1:4) coverage is 3.3 kJ/mol. This result is to be compared with the best experimental measurement of 13.5 kJ/mol.^{214,215}

The disagreement with experiment suggests that dispersive contribution to the binding energy, not accounted for by both HF and DFT methods, may play an important role. To cope with this flaw, Ugliengo and Damin²¹⁶ proposed an interesting approach to include correlation contributions at the MP2 level of theory, through a kind of cluster-in-crystal embedding technique. Those authors were able to obtain a final extrapolated MP2 binding energy of 12.7 kJ/mol, in good agreement with the experimental value, which shows that dispersive contributions account for about 7 kJ/mol.

Further examples of adsorption systems investigated with the CRYSTAL code include H₂O on NaCl¹⁸⁰; CO, N₂, and O₂ on LiF(100)^{178,179}; Na,²¹⁷ K,²¹⁸ and noble metals²¹⁹ on TiO₂ surfaces; CH₃OH,²²⁰ CO,²²¹ and CO₂²²² on SnO₂; CO on Cu₂O (111)²²³; formic acid²²⁴ and hydrogen²²⁵ on ZnO (10-10); the interaction of pyrite (100) surfaces with O₂ and H₂O²²⁶; NH₃ on a model of a silica surface²²⁷; HCl on water ice²¹¹; Cl on Cu (111)²⁰¹; and Pd on α -Al₂O₃ (0001).²²⁸

Interfaces

Apart from the simulation of ideal surfaces, increasing interest in “real” 2-D crystals now exists, which are quasi-periodic structures in two dimensions but only a few atomic layers thick, and which may present new and useful properties precisely because of their limited thickness. This branch of nanoscience is then an ideal ground for application of the slab model.

The study of epitaxial interfaces between crystals of different nature is an example of this flexible technique. The interface is modeled by creating two slabs and letting them interact to form a sort of supra-slab model (i.e., a wafer), as shown schematically in Figure 43. Care must be paid to the lattice mismatch because the 2-D unit cells, with different size, must match at the interface.

The interaction energy at the interface or adhesion energy is computed as

$$\Delta E = \frac{E(\text{interface}) - E(\text{slab1}) - E(\text{slab2})}{2} \quad [93]$$

which is the difference between the total energy of the interface model and the energies of the isolated slabs, divided by a factor two to account for the existence of two outer surfaces.

By taking the BSSE into account, we get:

$$\Delta E = \frac{E(\text{interface}) - E(\text{slab1}/[\text{slab2}]) - E([\text{slab1}]/\text{slab2})}{2} \quad [94]$$

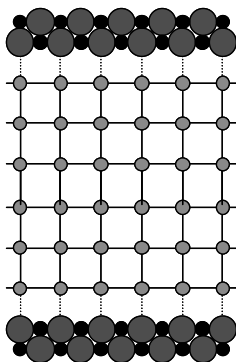


Figure 43 Schematic representation of an interface as simulated through a slab model.

where $E(\text{slab1}/[\text{slab2}])$ and $E([\text{slab1}]/\text{slab2})$ are, respectively, the energy of the first slab obtained in the presence of the basis functions of the second one, and vice versa.

An interesting example of the application of the slab model approach to the study of interfaces is the modeling of ultrathin oxide films on metallic substrate, which has been the subject of recently published papers by Pisani et al.^{229,230} It deals with a model of the epitaxially grown MgO (100) thin film on Ag (100). An advantage of studying the MgO/Ag system is that it has a small mismatch between MgO and Ag lattice parameters ($\sim 3\%$) and allows a cube-on-cube epitaxy.

This system was studied at the DFT level with both LDA (SPZ) and GGA (PW91) methods. A six-layer slab model of Ag parallel to the (100) surface was adopted, covered with one or two MgO monolayers on both surfaces (as in Figure 43). Three high symmetry configurations were considered: (A) Mg^{2+} upon a surface Ag atom, (B) O^{2-} upon a silver atom, and (C) both ions bridged.

The interaction energy computed with respect to the distance between the MgO overlayer, at first considered as a rigid entity, and the silver substrate is represented in Figure 44. The most stable configuration was found to be (B). Such a configuration was further analyzed, allowing an independent optimization of Mg and O positions to check the possibility of rumpling. Calculated MgO/Ag distances and BSSE-corrected adhesion energies are reported in Table 20.

Both DFT methods show that Mg relaxes toward the silver surface, although the rumpling is partly recovered when a second MgO layer is present, probably caused by the electrostatic attraction of the oxygen ions in the upper plane. Accordingly, the additional MgO layer also reduces the adhesion energy. It is worth noting that LDA gives an interaction energy that is larger (more than double) than GGA. This confirms the general observation that LDA

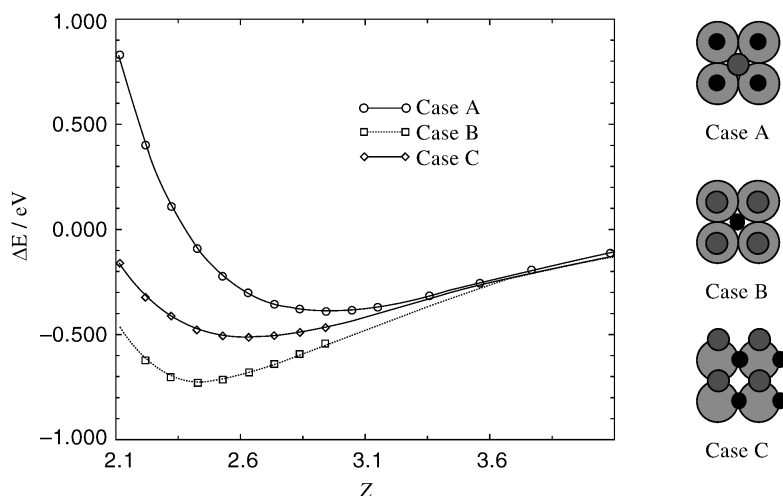


Figure 44 Interaction energy ΔE per MgO unit between a six-layer-thick silver slab and two monolayers of MgO at distance z . The reported data refer to the SPZ method.

methods tend to overestimate binding energies with respect to gradient-corrected methods, as already pointed out here for different kinds of system.

The interface model can be further complicated by considering the possible adsorption of molecules. Obviously, the substrate will modulate the interaction of the surface with adsorbates. For instance, the interaction of the Ag-supported MgO with water was simulated and compared with that on a pure MgO²²⁹ surface.

Interfaces are a field of growing interest, and some other applications have been carried out, which include ultra-thin adlayers of Ag on

Table 20 Calculated Properties of the MgO/Ag System in the (B) Configuration

	SPZ		PW91	
	No Rumpling	Rumpling	No Rumpling	Rumpling
One layer				
d_{Mg}	2.45	2.32	2.55	2.39
d_{O}	2.45	2.47	2.55	2.55
ΔE	-41.8	-53.1	-17.7	-29.6
Two layers				
d_{Mg}	2.45	2.38	2.55	2.46
d_{O}	2.45	2.47	2.55	2.55
ΔE	-41.1	-42.6	-18.2	-19.2

d_X is the distance of ion X from the surface. ΔE is the BSSE-corrected adhesion energy of the MgO overlayer on the Ag substrate (in kJ/mol).

MgO(100), MgO(110),²³¹⁻²³⁴ and Al₂O₃²³⁵; the interface between a transition metal oxide, NiO, and Ag(100),²³⁶ and the study of oxides on oxides, like the MgO/NiO films.^{237,238}

MODELING DEFECTIVE SYSTEMS

Defects in Solids

Defects in solids are ubiquitous and can be found both in the bulk and at the surface of materials.^{239,240} Two classes can be distinguished: point defects and extended defects. The former, also called local defects, produce a modification of the site environment of an otherwise perfect lattice: for instance, the absence of an atom in a lattice position (vacancy), the presence of an atom in an interstitial position (interstitial defect), or the substitution of an atom for another atom of a different chemical species at a regular lattice site (substitutional defect). Figure 45 shows typical examples of local defects in an ionic solid.

Extended defects, on the other hand, correspond to structural imperfections in the assembly of either lattice planes (planar defects), as stacking faults in layer structures, or lattice directions (linear defects), as dislocations.

At their surface, along with point (e.g., vacancy on a terrace) and extended defects (observed in crystal growth processes), solids present other typical defects such as vertices, edges, kinks, and steps, as shown in Figure 46. Defects play an important role in determining the surface reactivity, as briefly mentioned in the previous section for a stepped MgO surface model. In a

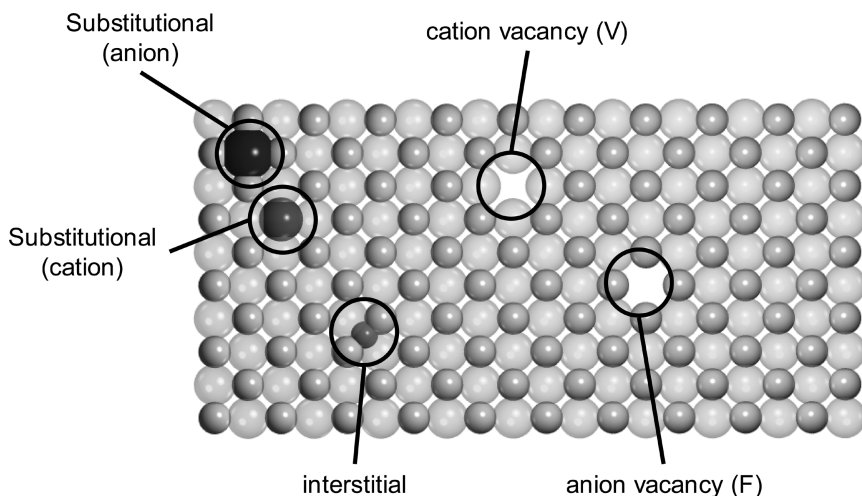


Figure 45 Examples of local defects in ionic solids.

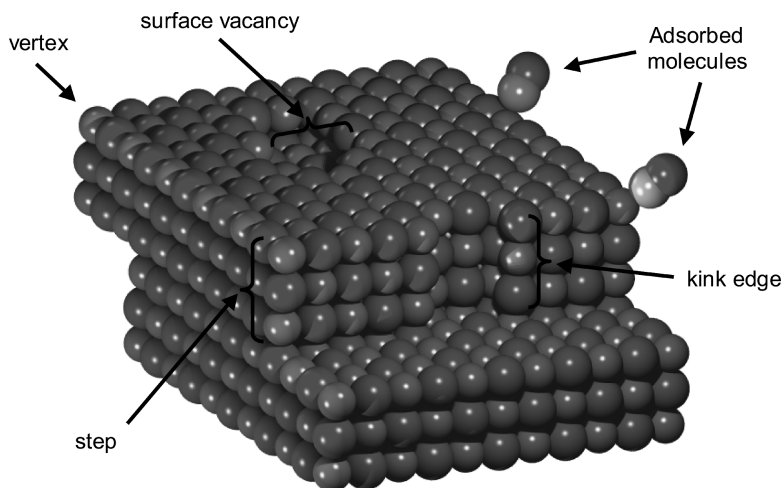


Figure 46 Examples of surface defects.

broad classification of defects, a surface with adsorbed atoms or molecules can also be considered as a defective system with respect to the bare surface.

How to Model a Defect

Here, we mainly focus on the modeling of point defects in a perfect crystal. Because of their local nature, we can assume that the perturbation in the crystal is small. Therefore, both structural and electronic effects can be considered as confined in the finite region close to the defect (defect zone). The rest of the system can then be treated as a perfect host with a well-defined periodic structure. On the basis of these assumptions, two strategies can be envisaged in the modeling of point defects:

1. The host as an environment
2. The defect as an impurity

The Host as an Environment

Both perfect and defective systems are simulated as a *finite cluster*, i.e., a relatively small cluster is cut out of the bulk structure containing the defect. This kind of strategy is also called the *cluster approach*.²⁴¹ The main advantage of this approach is its flexibility: first, because it does not assume any translational symmetry and allows us to investigate complex structures as defects in amorphous or disordered solids. Second, high quality standard molecular ab initio codes can be used, which thus allow a high-level quantum-mechanical treatment of the defect zone.

Nevertheless, the abrupt termination of an otherwise infinite solid gives rise to spurious effects, such as nonphysical electronic states localized at the boundary, levels in the gap, finite size quantum effects, and neglect of Coulomb and exchange interactions with the environment. Such effects depend on the nature of the chemical bond in the studied solids: ionic, semi-ionic, covalent, metallic, and molecular. Therefore, additional manipulations may be needed to take into account the environment where the cluster would be contained. For ionic systems, the most important contribution from the missing ions is the Coulomb field, which may be approximated by introducing a finite/infinite array of point charges or polarizable semiclassical ions, described with a shell model.²⁴¹ For metals and covalent solids, border quantum effects are important and not easily simulated. In covalent solids, the atoms at the surface present dangling bonds that have to be saturated with capping atoms, like H, F, and so on. An ambiguity remains, however, related to the field modification originating from the presence of the capping atoms, especially for mixed ionic-covalent situations.

It is worth mentioning here a variant of the cluster model that has been recently proposed to embed the cluster in its environment, based on a cluster-in-cluster scheme. The method, proposed by Morukuma et al., is the so-called our N-layer integrated molecular orbitals—molecular mechanics (ONIOM) scheme.^{242–244} The system is modeled through a large cluster (real system) that is then partitioned into two or more regions (model cluster). Each region is described with a hierarchical level of theory, higher for the model cluster and lower for the real system. The total energy is obtained from that of the real system, i.e., the largest cluster, including a series of correcting terms. This scheme, originally developed in a molecular context, has also been reformulated for defects-in-solids.^{245,246}

Finally, size and shape of the cluster are critically important and results should converge with the cluster size. Unfortunately, when enlarging the cluster, the number of atoms grows fast, which makes the calculation rapidly unaffordable. For solids with complex frameworks and containing a large unit cell, such as zeolites, it is also difficult to preserve the memory of the original crystalline structure in the cluster.

The Defect as an Impurity

The host system is treated as a perfect crystalline structure, and the exploitation of periodicity or quasi-periodicity is an essential ingredient when treating the defect as an impurity. From a quantum-mechanical point of view, the defect is treated as a perturbation to the electronic structure of the perfect crystal environment.

Two different approaches can be adopted:

1. The embedded cluster approach
2. The supercell approach

The embedded cluster approach is based on schemes that smoothly link the quantum-mechanical solution of the cluster to the perfect crystal. Different methods have been developed based on either Green function²⁴⁷ or group-function (localized crystalline orbitals)²⁴⁸ techniques.

In the supercell approach, the defect is instead enclosed in a sufficiently large unit cell and periodically repeated throughout space. A common problem with both approaches is the availability of high-level quantum-mechanical periodic solutions, because, as already mentioned, it is difficult to go beyond the one-electron Hamiltonian approximations (HF and DFT), at present.

The supercell scheme is the most widely adopted approach because it is easily implemented in all periodic *ab initio* codes. Embedding approaches, on the other hand, may require specific and not widely disseminated softwares, which make their development slow, and their accuracy relatively low. A discussion of limits and merits of the embedding techniques can be found in Pisani.²⁴⁹

In the following pages, we illustrate in more detail the supercell approach and discuss a few examples.

The Supercell Approach

The supercell approach consists of a periodic replica of the defect, which is enclosed in a large nonprimitive unit cell. A pictorial view (in 2-D) of the supercell approach is given in Figure 47, where, by starting from the perfect

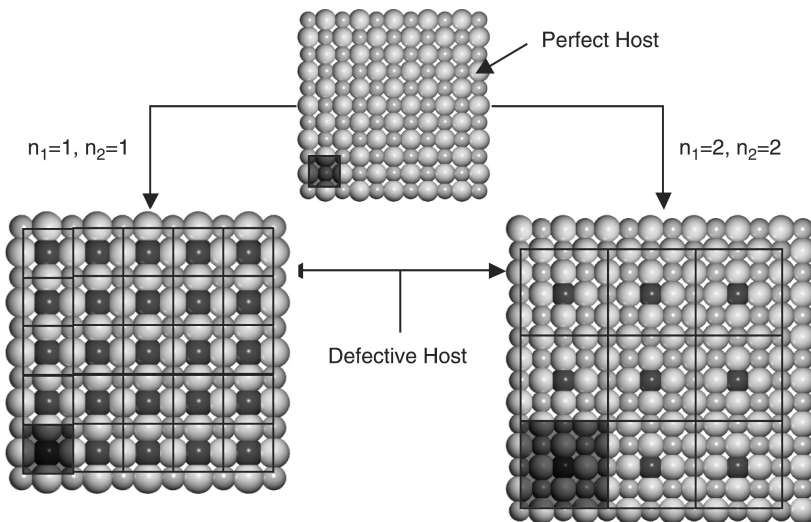


Figure 47 Schematic example of a local defect in a two-dimensional lattice as modeled by the supercell approach.

host, a substitutional defect is created through two bi-dimensional supercell models with different size.

The supercell scheme has some attractive features:

1. It is of wide applicability, and it may be adopted, in principle, to model both bulk and surface defects of ionic, covalent, metallic, and molecular systems.
2. It is conceptually simple. The size of the supercell depends on an expansion matrix that consists of integers. The matrix is 2×2 or 3×3 according to the dimensionality of the periodic system.
3. It allows for a proper definition of the defect formation energy, as will be discussed in the next section.
4. Properties of the defective solid can be calculated easily.

Obviously, computed properties are required to converge with the supercell size. This internal consistency check is important for estimating the interaction between defects in neighboring cells. In fact, two kinds of limitations in the model exist, which correspond to two different levels of complexity:

1. The supercell size must be such as to contain the defect zone, which includes all atoms involved in the structural and electronic relaxation.
2. The distance among defects must be large enough to reduce their electrostatic interaction to negligible values.

In the latter case, it must be distinguished whether the defect is neutral or charged. For neutral defects, the supercell scheme is expected to converge quickly to the isolated defect limit (we will see later that “quickly” can imply large supercells).

For charged defects, the electrostatic energy of the supercell diverges, and approximations must be adopted to neutralize the unit cell to cancel the interaction between neutralized defects. The treatment of charged defects within periodic boundary conditions is still a partially unsolved problem, and *ad hoc* solutions have been proposed like, for instance, the corrective schemes proposed in Leslie and Gillan,²⁵⁰ Makov and Payne,²⁵¹ and Gerstmann et al.²⁵²

Finally, the supercell shape should be such as to exploit the point symmetry of the defect as far as possible.

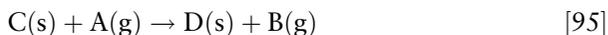
When a suitable supercell model of the defective system is devised, three major issues have to be faced:

1. The determination of the equilibrium geometry, that is the evaluation of structural effects on the surroundings because of the presence of the defect (relaxation/reconstruction).
2. The description of the electronic structure in the defect region.
3. The estimate of the defect formation energy.

Points 1 and 2 will be highlighted with a number of examples, whereas point 3 deserves some more comments.

Defect Formation Energy

The formation process of a point defect can be described by the reaction:



where C is the perfect crystal and D is the defective system. A and B are the reactants and the products, respectively, and are typically atomic or molecular species, usually in the gas (g) phase. For instance, in a substitutional defect, A is the substituting atom for atom B. In the process of creating a vacancy, A is absent and B is the leaving moiety. The formation energy is then given by the following expression:

$$\Delta E^n = E^n(D) - nE(C) + E(B) - E(A) \quad [96]$$

i.e., the energy difference between the infinite system with the defect ($E(D)$) and without ($E(C)$), plus the energy difference of the atomic reactants, $E(A)$, and products, $E(B)$, with n being the ratio between the volume of the supercell S_n and that of the perfect crystal primitive cell.

The defect formation energy can also be considered as the sum of two contributions: a term originating from the creation of the defect in the perfect crystal, $\Delta E^n(\text{dc})$, and a term that accounts for the relaxation effects because of the perturbation caused by the presence of the defect, $\Delta E^n(\text{rel})$. That is,

$$\Delta E^n = \Delta E^n(\text{dc}) + \Delta E^n(\text{rel}) \quad [97]$$

Within the supercell approach, ΔE^n should tend to a well-defined limit with increasing the supercell size:

$$\Delta E = \lim_{n \rightarrow \infty} \Delta E^n \quad [98]$$

For a defect to be considered as isolated, sufficiently large supercells must be adopted to avoid spurious interactions among neighboring defects because of both relaxation/reconstruction and long-range electrostatic effects.

To allow a consistent definition of the defect formation energy, the computational method must satisfy a size-extensivity criterion: Supercells of different size, for the perfect crystal, must provide the same value per formula unit for all properties.

Examples

The applicability of ab initio periodic methods to the study of defects will be illustrated through a few examples, the first of which is a neutral vacancy in LiF. This defect is typical in ionic solids, called F-center, because its presence produces a color change (F comes from the German: *Farbe*) in the bulk material.

The second example concerns trapped hole centers in alkaline earth oxides (BeO, MgO, CaO, and SrO). These neutral defects essentially consist of the substitution of a monovalent cation (H/D, Li, Na, K) for one of the bivalent cations (Be, Mg, Ca, Sr). Thus, one electron is missing, so that an electron hole is expected to be localized and “trapped” at the substitutional cation. In both cases, the defect is paramagnetic, and in the second one, part of the original lattice symmetry is lost.

A third example, carbon substitution in bulk silicon will compare the cluster and supercell approaches.

F-center in LiF

An F-center consists of an electron trapped at a negative-ion vacancy within the crystal. It is a paramagnetic defect, and its presence in ionic compounds has been the object of extensive and systematic experimental investigations, mainly by means of EPR and ENDOR techniques. Here we consider an F-center in LiF.^{140,253} Computational details and references to experimental data are reported elsewhere in the original papers.^{140,253}

This defect is a good case for size-extensivity checks, because it is simple, with the full cubic symmetry of the unperturbed lattice. Moreover, a relatively small basis set can be adopted because light atoms are involved, so it has been possible to consider supercells containing up to 256 atoms (or 128 primitive cells, S_{128}).

Energy data are given in Table 21. The fourth column indicates that the defect formation energy converges rapidly even with relatively small supercells. The second column is reported just to show that the total energy per LiF pair of the perfect crystal is independent of the size of the supercell.

Relaxation effects are small as shown in Table 22 for S_{32} . Partial relaxation was allowed by including progressively up to the third nearest-neighbors

Table 21 Effect of the Supercell Size on the Defect Formation Energy, ΔE^n (in kJ/mol)

n	Lattice	$E^n(\text{LiF})^a$	$E^2(\text{LiF})^b$	$E^{n-1}(\text{F-c})^c$	ΔE^{n-d}
4	P ^e	-428.221800	-107.055450	-328.590048	674.0
8	F ^f	-856.443601	-107.055450	-756.811638	674.6
16	I ^g	-1712.887207	-107.055450	-1613.255239	674.6
27	F	-2890.497155	-107.055450	-2790.865051	674.9
32	P	-3425.774381	-107.055449	-3326.142400	674.6
64	F	-6851.548839	-107.055451	-6751.916825	674.7
108	P	-11561.988593	-107.055450	-11462.356596	674.6
125	F	-13381.931279	-107.055450	-13282.299274	674.7
128	I	-13703.097661	-107.055450	-13603.465658	674.7

^aTotal energy (hartree) of a perfect LiF supercell.

^bTotal energy (hartree) per LiF formula unit.

^cTotal energy (hartree) of the F-center defective system.

^dReferred to the unrelaxed defect geometry.

^ePrimitive lattice.

^fFace-centered lattice.

^gBody-centered lattice.

Table 22 Relaxation Effects in F-Centred LiF for a S_{32} Supercell Model

	N^a	ΔE^c	I^d	II^d	III^d
First nearest neighbours	6 (6) ^b	-1.7	0.028		
Second nearest neighbours	18 (12)	-2.3	0.035	0.011	
Third nearest neighbours	26 (8)	-2.3	0.035	0.011	-0.001
Fully relaxed	63	-2.6	0.040	0.013	-0.003

^aNumber of relaxed atoms.

^bNumber of atoms in each *star* (set of atoms equidistant from the defect) of neighbors.

^cGain in energy (in kJ/mol) with respect to the unrelaxed structure.

^dDisplacements (in Å) of the stars of neighbors with respect to their position in the unrelaxed geometry.

of the F-center, in order to show the trend to the fully relaxed geometry. Data indicate that nearest and next-nearest neighbors move away from the defect center by a small amount, with the largest relaxation involving the nearest neighbors, whereas relaxation of the third nearest neighbors is negligible. Accordingly, the gain in energy caused by relaxation is just a few kJ/mol. Relaxation effects are thus negligible and die down quickly, so that the unrelaxed structure could safely be considered as the reference geometry.

One of the interesting features of LiF is that it has been a sort of model system in the interpretation of EPR and ENDOR data.²⁵⁴ Experimental spectra have been fitted to model Hamiltonians, and hyperfine coupling constants up to the eighth nearest neighbors have been proposed.²⁵⁵ In the calculation of the hyperfine coupling, it is then important to check the convergence of the spin density $\rho^{\alpha-\beta}$ with the supercell size, not only at the center of the defect, but also at a relatively large distance from it. The spin density at the nuclear position for various supercells up to nine stars of neighbors is given in Table 23.

Table 23 Effect of the Supercell Size on the Spin Density $\rho^{\alpha-\beta}$ (in units of 10^{-2} bohr⁻³) at the Nuclei of the Indicated Atoms for the F-Centre in LiF

n	F_C^a	I Li_{100}^b	II F_{110}	III Li_{111}	IV F_{200}	V Li_{210}	VI F_{211}	VII F_{220}	VIII Li_{221}	IX Li_{300}
4	2.074	4.431	7.204	0.054						
8	2.080	2.272	3.641	0.021	0.143					
16	2.083	2.254	1.835	0.013	0.116	0.017				
27	2.082	2.255	1.837	0.006	0.022	0.008	0.034			0.000
32	2.083	2.255	1.829	0.007	0.044	0.009	0.038	0.096	0.000	
64	2.083	2.255	1.816	0.006	0.021	0.004	0.013	0.039	0.000	0.000
108	2.083	2.255	1.819	0.006	0.021	0.004	0.012	0.021	0.000	0.000
125	2.083	2.255	1.816	0.006	0.021	0.004	0.011	0.020	0.000	0.000
128	2.083	2.255	1.816	0.006	0.021	0.004	0.011	0.020	0.000	0.000

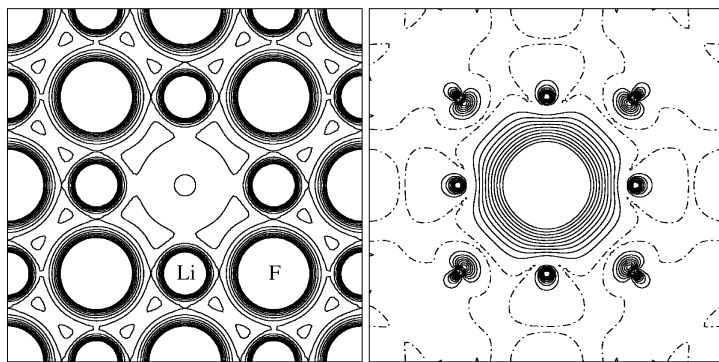
Nine sets of neighbors are considered (I-IX).

^a F_C is the anion vacancy.

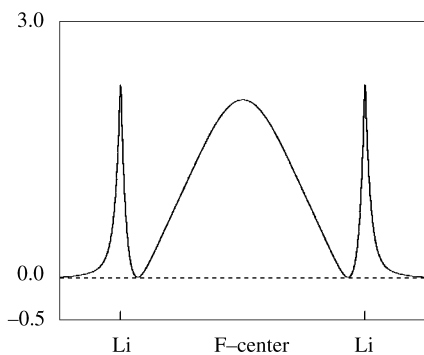
^bSubscripts give the Cartesian coordinates of the vacancy neighbors in units of the cation-anion distance.

S_{32} is the smallest supercell containing all atoms of interest. When S_{108} is considered, all $\rho^{\alpha-\beta}$ at the nuclei up to the eighth nearest neighbors are numerically stable with respect to larger cells. The table shows that after the second neighbors, the spin density drops by two orders of magnitude.

Insights on the nature of the paramagnetic defect can be obtained by analysis of the electronic structure. Figure 48(a) shows the total charge (left) and the spin density (right) of the F-center in LiF (S_{16}) obtained at the UHF level. The spin density map shows that the unpaired electron is localized at the vacancy site, whereas the spin density profile [Figure 48(b)] gives an indication



(a)



(b)

Figure 48 (a) Total charge and spin density maps for an F-center in LiF as obtained at the UHF level of theory. The section is parallel to the (100) plane through the defect. The separation between contiguous isodensity curves is 0.01 and 0.001 bohr⁻³ for the electron charge and spin density, respectively. The density range is 0.01–0.1(charge) and –0.01–0.01(spun). Continuous, dashed, and dot-dashed lines denote positive, negative, and zero values. (b) Spin density profile (in 10⁻² bohr⁻³) along a line connecting the F-center to opposite nearest neighboring Li ions. Ticks indicate nuclear positions.

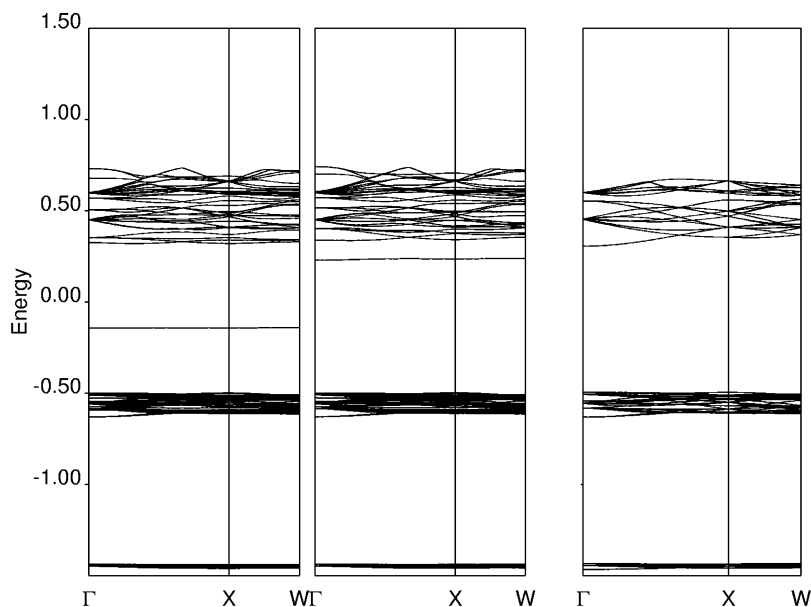
Table 24 Mulliken Charge q (in electrons) and Spin Density $\rho^{\alpha-\beta}$ (in units of 10^{-2} bohr $^{-3}$) at the Vacancy Site (F-center) Obtained with Various Hamiltonians (S_{16})

	UHF	SPZ	BLYP	PBE	B3LYP
q	1.05	0.89	1.06	0.93	1.03
$\rho^{\alpha-\beta}$	2.08	1.66	1.86	1.73	1.89

of the spread of the spin density within the vacancy. The Mulliken charge of the F-center (first row of Table 24) confirms that the amount of electronic charge that can be attributed to the vacancy is close to one.

One of the possible effects of the presence of a defect is the appearance of localized states in the band gap of the perfect host. Trapping and releasing electrons to and from these states requires less energy than exciting electrons from the top of the valence band to the bottom of the conduction band of the perfect crystal.

Figure 49 shows the band structure of the F-center in LiF for the S_{16} -supercell model obtained at the UHF level along with the band structure of bulk LiF. Alpha and beta electrons are described by different sets of orbitals. Two band structures are obtained for the α - and β -spin states. The shape of the bands is similar to those of the perfect system, but a new band appears in the


Figure 49 Band structure for α - (left) and β -spin (middle) of the LiF F-center and perfect LiF (right). Plotted data refer to a UHF calculation with a S_{16} supercell.

band gap, because of the state associated with the F-center. The analysis of that band through the projected density of states shows that it is essentially associated with a hydrogen s-like state.

When other Hamiltonians are considered, the qualitative picture of the defect remains essentially unaltered (we will see that this is not the case for the trapped hole centers in alkaline earth oxides), as shown in Table 24, where Mulliken charge q and spin density $\rho^{\alpha-\beta}$ at the vacancy site obtained with five different Hamiltonians is reported.¹⁴⁰

The general picture emerging from the UHF and UDFT data confirm that the F-center is nearly totally localized at the anion vacancy and that the various functionals provide similar descriptions. Note that UDFT tends to spread the spin density onto the nearest neighbors, in particular with the local density approximation. This picture is also confirmed by spin density maps and profiles (not reported here, see Mallia et al.²⁵³).

In summary, when we consider the applicability of the supercell model to the LiF defect, we see that in this case, we are in a favorable position, because:

1. Nuclear relaxation is small.
2. Electronic perturbation is confined within nearest neighbors, and actually from the next-nearest neighbors the electronic density is indistinguishable from the perfect bulk on a “normal” scale.
3. The defect is neutral and conforms to the cubic symmetry, as no long-range electrostatic defect-defect and defect-bulk effects take place.

Because of these conditions, S_8 or S_{16} would be large enough, if we were interested only in the properties of the F-center itself. As, however, we are also investigating the hyperfine coupling of the unpaired electron with up to the eighth nearest neighbors, a much larger supercell is required. Thus, the point is then raised concerning the definition of the extent of the “perturbed zone”: Because the hyperfine coupling is detected up to the seventh nearest neighbors by EPR/ENDOR experiments, the perturbed zone is obviously large enough to include up to the seventh nearest neighbors. However, the amount of spin density present at the nuclei farther than the next-nearest neighbors is small (see Table 23), and examining these interactions becomes interesting only in this special case, where extremely accurate and sensitive experiments are available. As other properties are concerned, such as the defect formation energy (Table 21) or the nuclear relaxation (Table 22), the perturbed zone is much smaller, and a S_8 - S_{16} supercell is large enough for most purposes, as previously mentioned.

Let us now consider a slightly more complicated defect, which is common in all alkaline earth oxides.

Trapped Hole Centers in Alkaline Earth Oxides

The Cubic Oxides: Li in MgO. Ionizing radiation produces a variety of trapped hole centers in alkaline earth oxides at low temperature. In the cubic

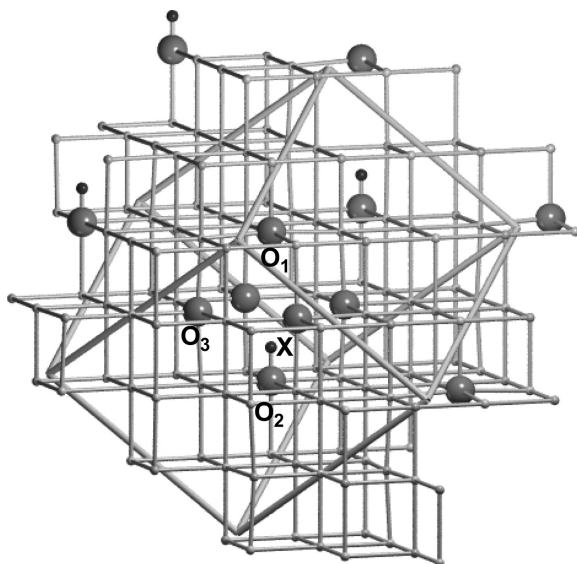


Figure 50 Schematic picture of a S_{16} supercell model of the trapped hole center in cubic alkaline earth oxide: $MO:[X]^0$ (where $M = \text{Mg, Ca, Sr}$ and $X = \text{H, Li, Na}$). O_1 is the oxygen ion at which the hole is trapped.

case (MgO , CaO , SrO , excluding BeO , which has a lower symmetry), the defect has axial symmetry along one of the main directions of the cubic lattice. The presence of various impurity ions occupying different positions along the hole-vacancy axis produces neutral defects indicated as $[X]^0$, where X represents H, Li, Na , or K (see Figure 50). When X stands for H (D), the defects are also denoted as V_{OH} (V_{OD}) centers. These trapped holes have been the subject of theoretical investigations at the UHF level of theory.^{140,175,256–259} Here we only discuss the $\text{MgO}:[\text{Li}]^0$ case and refer to the cited papers for additional information on experimental evidences and computational details not included here.

The convergence of the defect data with the supercell size must be checked again. Table 25 reports the defect formation energies of the S_8 , S_{16} , S_{32} , and S_{64} supercells, with respect to the atomic energies of the species involved in the substitution (Li : -7.429609 hartree; Mg : -199.602732

Table 25 Dependence of the $\text{MgO}:[\text{Li}]^0$ Defect Formation Energy (in kJ/mol) with Respect to the Supercell Size and Geometry Relaxation

	S_8	S_{16}	S_{32}	S_{64}
Li only	465.3	481.3	488.0	492.4
Full relaxation	403.8	400.8	401.1	400.4

hartree), when only the Li atom is allowed to relax (first row) and for the fully relaxed defective structure (second row).

We can compare the first row of Table 25, where the defect formation energy increases by about 40 kJ/mol in going from the smallest to the largest supercell, with the LiF case (Table 21), where convergence is already reached in the unrelaxed defective structure.

The main difference here is that the substitution of a Mg atom with lithium lowers the crystalline symmetry from cubic to tetragonal and generates a dipole moment within the cell, as a consequence of the Li displacement. A long-range dipolar defect–defect interaction originates then among defects in neighboring cells, and larger supercells are needed to compensate for it.

However, when all atoms in the cell are allowed to relax, a dramatic change is observed in the defect formation energy, which decreases by 61.5, 80.5, 86.9, and 92.0 kJ/mol for the four supercells. Again, this behavior can be compared with the case of the F-center in LiF, where relaxation effects are essentially absent (2–3 kJ/mol). In the fully relaxed case, the convergence of the defect formation energy is much faster (3 kJ/mol in going from S_8 to S_{64}), which shows that structural relaxation is an effective mechanism to screen and minimize long-range electrostatic interactions induced by the dipolar nature of the defect center.

Thus, geometry optimization plays a crucial role, which has been analyzed through partial optimizations within the S_{64} supercell, by including an increasing number of neighbors in the process. Results are reported in Table 26.

When only the atomic position of lithium is optimized, it migrates by $\Delta z = 0.279 \text{ \AA}$ away from O_1 , with a corresponding relaxation energy of 31.3 kJ/mol; when the first nearest neighbors of Li along the z axis (O_1 , O_2)

Table 26 Convergence of the $\text{MgO}:[\text{Li}]^0$ Defect Formation Energy (in kJ/mol) in the S_{64} Supercell with Respect to Structural Relaxation (in \AA) Allowed up to the Fourth Nearest Neighbors of the Defect in the Otherwise Unrelaxed Structure (changes in the geometry around the defect are also reported)

	Unrelaxed	Li	Li + O_1^a + O_2^a	Li + $O(6)^c$	Li + $O(6)$ + $\text{Mg}(12)$	Li + $O(6)$ + $\text{Mg}(12)$ + $O(8)$	Li + $O(6)$ + $\text{Mg}(12)$ + $O(8)$ + $\text{Mg}(6)$	Fully relaxed
ΔE	523.7	492.4	484.2	477.2	428.3	426.3	411.2	400.4
Li Δz		0.279	0.312	0.291	0.251	0.251	0.245	0.236
O_1^a Δz			-0.032	-0.031	0.003	0.002	-0.017	0.007
O_2^a Δz			0.095	0.075	0.059	0.060	0.060	0.059
O_3^b Δz				-0.035	-0.017	-0.015	-0.013	-0.012
Δr				0.035	0.040	0.040	0.040	-0.046

^aOxygen atoms above and below the Li atom along the defect axis (see Figure 50).

^bEquatorial oxygen atom (see Figure 50).

^c $O(6)$ includes also the four equatorial oxygen atoms around the defect in addition to O_1 and O_2 .

are also relaxed, the energy gain is 8.2 kJ/mol and displacements are $\Delta z(\text{O}_1) = -0.032 \text{ \AA}$, $\Delta z(\text{O}_2) = 0.095 \text{ \AA}$. When also including the four equatorial O_3 atoms, the formation energy decreases further by 7.0 kJ/mol and the displacements of O_3 are $\Delta z = -0.035 \text{ \AA}$ and $\Delta r = 0.035 \text{ \AA}$ (in the direction perpendicular to the axial defect). Including in the geometry optimization the next star of neighbors (12 atoms of magnesium) reduces the formation energy by 48.9 kJ/mol. Full relaxation leads to a total gain of 123.3 kJ/mol. Interestingly, a large fraction of the energy gain is caused by the relaxation of the Mg ions (48.9+15.1 kJ/mol, to be compared with 15.2 + 2.0 kJ/mol for the first and third oxygen neighbors), the reason being that Mg^{2+} is smaller than O^{2-} and mobile in the cage of its six oxygen neighbors, which is rigid, because the oxygen ions are in contact. The smaller the cation, the larger this effect, as in the case of Be^{2+} (see next example).

The relaxation mechanism is simple and similar in all alkaline earth oxides: When the alkali metal ion replaces an alkaline earth cation, it relaxes from the perfect lattice position toward the oxygen ion (O_2) along the axial direction (z axis), which brings a formal +2 charge; the electron hole localizes at the opposite oxygen (O_1), which in turn relaxes away from the X monovalent ion.

The S_{32} supercell is certainly adequate for describing this defect, and it will be used for the analysis of its electronic and magnetic features as follows. The electron charge and spin density, computed at the UHF level of theory and shown on the top of Figure 51, illustrates the two main effects of substituting a Li ion for one Mg in MgO. Li binds to one of the neighboring O ions (O_2) and, at the same time, like all other monovalent cations, acts as a dopant, which causes the formation of a trapped electron hole, well localized at the opposite ion (O_1). The spin density map permits us to appreciate the localization of the unpaired electron at O_1 , in a p_z -type state, with minor spin polarization on the neighboring atoms. This analysis is supported by the Mulliken population data, having a net charge of about +1 electrons for Li, -1 for O_1 , and -2 for O_2 . According to the spin density Mulliken analysis, the spin moment of O_1 is close to 1 electron, whereas it is almost null on Li and on the other neighboring oxygen ions.

The different role of O_1 and O_2 among the O ions of the crystal is reflected in the band structure. In particular, the p states of both atoms split off the valence band, which is essentially contributed to by the p orbitals of the bulk oxygen atoms, as shown in Figure 52. A detailed analysis of the band structure shows that the most stable α states are associated with the p_z (lower in energy) and the p_x, p_y orbitals of O_1 ; the stabilization is a consequence of the lack of interelectronic repulsion with the corresponding β electron. The empty $\beta - p_z$ state corresponds to the hole level and lies in the band gap.

As stated above, the UHF electronic structure of the trapped hole defect indicates the localization of the unpaired electron at the O_1 atom. However, this picture changes significantly when different Hamiltonians are

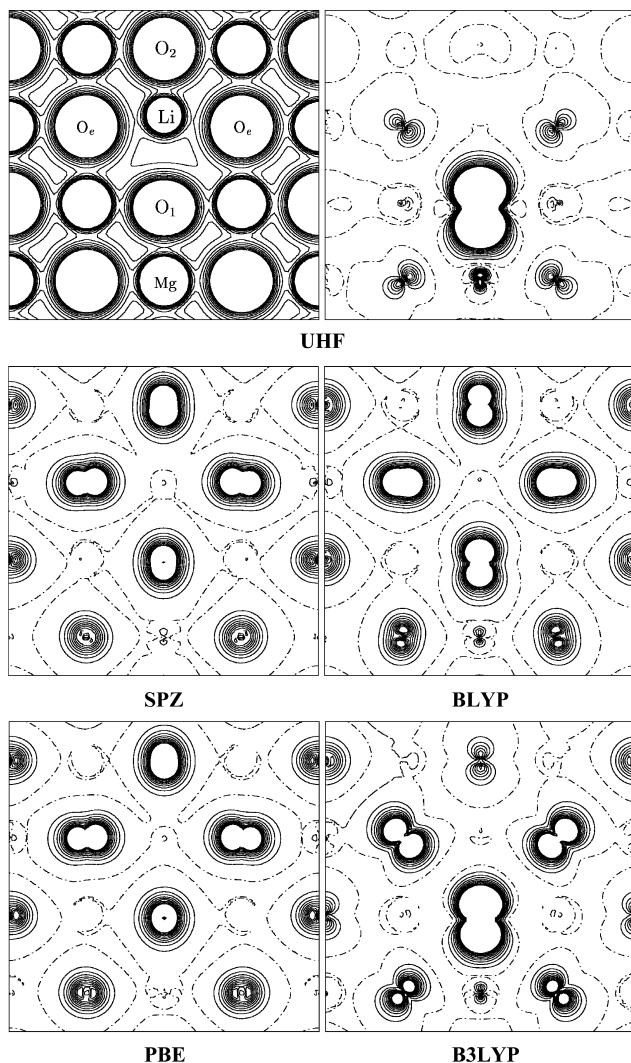


Figure 51 Total charge and spin density maps for $\text{MgO}:[\text{Li}]^0$ as obtained at the UHF level and with various DFT Hamiltonians. The section illustrated is parallel to the (100) plane through the defect. The separation between contiguous isodensity curves is 0.01 and 0.001 bohr^{-3} for the electron charge and spin density, respectively. The density range is 0.01–0.1(charge) and -0.01 –0.01(spin map). Continuous, dashed, and dot-dashed lines denote positive, negative, and zero values.

considered.¹⁴⁰ Table 27 reports the net atomic charges and spin moments on Li, O_1 , O_2 , and O_3 , in $\text{MgO}:[\text{Li}]^0$, as computed with UHF and four different DFT methods. The degree of localization as quantified by the spin moment of O_1 (Table 27) decreases from 0.98 at the UHF level, to 0.41 for B3LYP, to

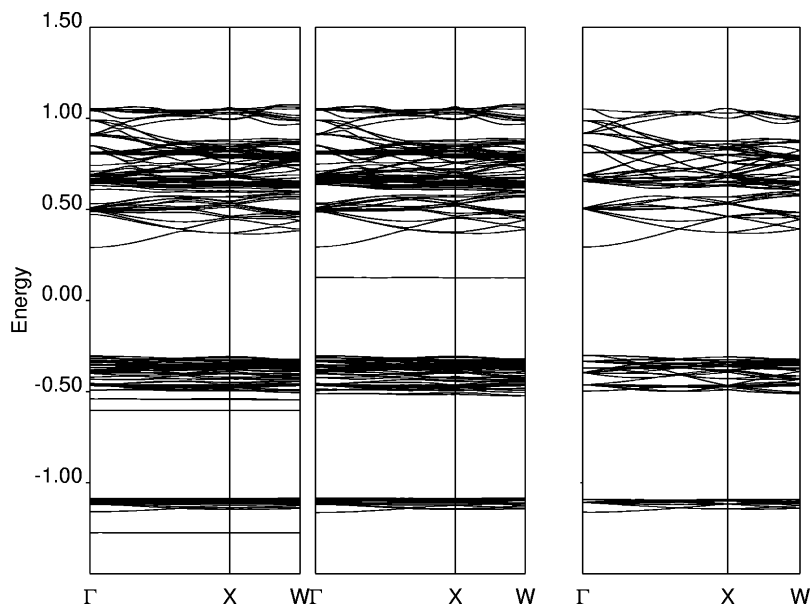


Figure 52 Band structure for α - (left) and β -spin (middle) of $\text{MgO}:\text{[Li]}^0$ and perfect MgO (right). Plotted data refer to a UHF calculation with a S_{16} supercell.

about 0.1 with other DFT methods. With DFT methods, this spread of the unpaired electron over the nearest and next-nearest oxygen neighbors is evident in the spin density maps (Figure 51) and causes the O_1 ion to have a net charge similar to the other oxygen ions in the lattice, i.e., about -1.7 electrons.

The different degree of localization produced by DFT methods also has important consequences on the atomic relaxation, with the Li ion being less strongly attracted to O_2 than at the UHF level. These effects are less pronounced when the hybrid B3LYP method is adopted.

Table 27 Net Atomic Charges (q) and Spin Moments (μ) in $\text{MgO}:\text{[Li]}^0$ Evaluated According to a Mulliken Partition of Charge and Spin Densities

Method	Li		O_1		O_2		O_3	
	q	μ	q	μ	Q	μ	q	μ
UHF	+0.99	0.00	-1.03	0.97	-1.91	0.00	-1.88	0.01
SPZ	+0.98	0.00	-1.71	0.09	-1.69	0.12	-1.69	0.11
BLYP	+0.97	0.00	-1.66	0.14	-1.70	0.10	-1.68	0.11
PBE	+0.98	0.00	-1.74	0.08	-1.71	0.10	-1.71	0.10
B3LYP	+0.98	0.00	-1.48	0.41	-1.80	0.01	-1.72	0.10

Label of atoms as in Figure 50. Data in electrons.

Table 28 Calculated and Experimental Hyperfine Isotropic (*a*) and Anisotropic (*b*) Coupling Constants and Nuclear Quadrupole (*P*) Coupling Constant for $\text{MgO}:[\text{Li}]^0$

Method	<i>a</i>	<i>b</i>	<i>P</i>
UHF	-2.393	2.258	-0.017
SPZ	-3.691	-0.129	-0.003
BLYP	-3.078	0.092	-0.003
PBE	-3.979	-0.202	-0.010
B3LYP	-3.339	0.480	-0.004
Exp. ^a	-4.539	2.313	-0.014

^aExperimental data taken from Abraham et al.²⁶⁰ and Chen and Abraham.²⁶¹

Magnetic coupling constants determined by EPR and ENDOR techniques permit a direct comparison with experimental data. Table 28 shows that, in the particular case of the Li defect, the agreement is reasonable for the UHF result, where the hole is localized at O_1 . For the other Hamiltonians, the disagreement increases in parallel with the delocalization of the hole.

The BeO Case. The Li-trapped hole center in BeO ($\text{BeO}:[\text{Li}]^0$), is slightly more complicated than the corresponding defect in MgO, and it presents some new features we must now consider. At variance with respect to the other alkaline earth oxides, BeO has a wurzite-like crystalline structure. The cation is fourfold coordinated, with one Be-O distance (the axial or vertical one) slightly different from the other three that are equivalent. Substitution of Li^+ for one Be^{2+} ion in the hexagonal structure generates an electron hole that can be localized either at the axial oxygen or at one of the three equatorial oxygen ions, which is indicated in Figure 53 as O^- .

These features make studying the relative stability of the two point defects interesting. Experiment²⁶² indicates that, when the crystal is irradiated at low temperature, the hole is trapped at an axial oxygen; electron holes at

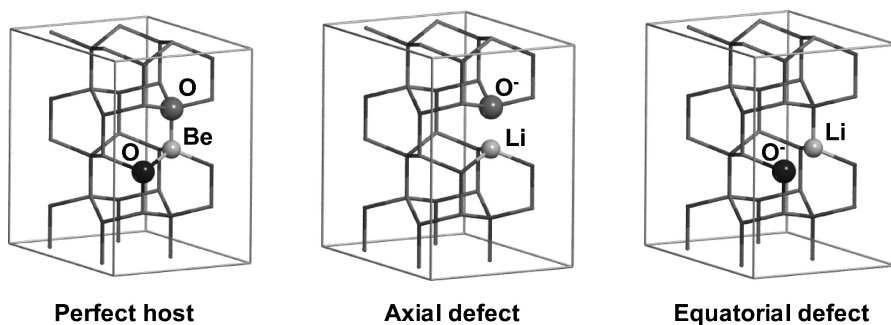


Figure 53 Schematic view of a S_{16} supercell model of the two different trapped hole centers in BeO. O^- indicates the oxygen ion where the electron hole is localized. Axial oxygen in light-gray, and equatorial oxygen in black.

Table 29 Defect Formation Energy, ΔE , and Relative Stability, δE , (in kJ/mol) of the BeO:[Li]⁰ Axial and Equatorial Centers as Obtained with Supercells of Different Size

Supercell ^a	BeO	Axial BeO:[Li] ⁰		Equatorial BeO:[Li] ⁰ Ax-Eq		
	E_{tot}	E_{tot}	ΔE	E_{tot}	ΔE	δE
S ₁₆ (2 2 2)	-1435.23633	-1427.83826	677.9	-1427.85604	631.2	46.7
S ₅₄ (3 3 3)	-4843.92262	-4836.53959	638.4	-4836.54241	631.0	7.4
S ₁₂₈ (4 4 4)	-11481.89066	-11474.50982	632.6	-11474.51129	628.8	3.8

Total energies in hartrees.

^a(i j k) are the expansion coefficients of the primitive lattice basis vectors **a**, **b** and **c** to obtain S_n .

equatorial oxygens can be obtained via thermal excitation. The energy difference between the two configurations is then expected to be small. At variance with the cases previously discussed, here we are not interested in the absolute defect formation energy, but in the relative value for the two positions. How much this relative value depends on the supercell size must be checked carefully.

Calculations have been performed at the UHF level with full optimization of the positions of all atoms in the supercell. As for cubic alkaline earth oxides, at the UHF level of the theory, the electron hole is fully localized at O⁻.

In both the axial and the equatorial configurations, relaxation of Li⁺ and O⁻ is qualitatively similar to that observed for the other members of the series. However, the extent of the O⁻ relaxation in the case of the axial defect, $\Delta r = -0.23$ Å, is four times as large as in MgO:[Li]⁰, where $\Delta r = -0.05$ Å. Relaxation of the Be²⁺ ions is larger than that of the Mg²⁺ ions, because the former can migrate more easily in the oxygen cage.

The formation energy obtained with three supercells of increasing size is reported in Table 29, which shows that the convergence of the formation energy with the supercell size is much slower than the one reported for MgO:[Li]⁰ (Table 25), where the formation energy is stable already for small supercells.

Many reasons exist for this different behavior: In MgO, the point symmetry remains high (tetragonal); the mobility of ions (in particular of the cations) is low, so that relaxation effects are not large; the site coordination of the ions remains essentially octahedral. In the present case, Be is almost free to move within the oxygen cage, the point symmetry of the defect is lower than in the MgO case, and the site symmetry of each ion is also lower so that nonzero low-order multipoles are generated by the defect. As a consequence, larger supercells are required.

Indeed, the defect formation energy of the axial defect is still changing by more than 5 kJ/mol when going from S₅₄ to S₁₂₈ (Table 29). The screening mechanism is more effective in the equatorial direction along which the defect is better accommodated. Table 29 shows that the equatorial defect is more

stable than the axial one for the supercells considered here, in disagreement with experimental evidence,²⁶² with the energy difference between the two configurations, however, small and decreasing when increasing the supercell size. In supercells as large as $S_{250}(5\ 5\ 5)$ or $S_{432}(6\ 6\ 6)$, the stability order might be reversed. Unfortunately, they correspond to large unit cells containing 500 and 864 atoms, respectively, that would make the calculation demanding.

To check the mutual interactions of defects in different supercells, the formation energy of the axial center has been studied in more detail. A series of 13 supercells with increasing size (from 32 to 300 atoms) and different shape has been considered. In fact, given the hexagonal unit cell, the supercell may be increased by enlarging it in either the axial or the equatorial direction, or both. Figure 54 shows, graphically, the dependence of the formation energy on the number of atoms in the supercell. Each $\text{Li}^+ - \text{O}^-$ pair can be viewed as a dipole oriented along the c axis. Making the supercell larger in the equatorial directions (see the $S_n(i\ i\ 3)$ series connected by the continuous line in the figure) reduces the dipole lateral repulsion and decreases the formation energy. On the contrary, when separating the dipole along the axial direction, the cooperative interaction between dipoles decreases and ΔE grows slightly (see, for example, the $S_n(3\ 3\ i)$ series). By growing the supercell equatorially, ΔE converges more rapidly with respect to axial growth, as can be seen comparing the $S_n(3\ 3\ i)$ and $S_m(4\ 4\ i)$ series.

The present example shows that it is not difficult to find situations where the supercell size must be large, and the accuracy of the calculations, referring to different supercells, must be high.

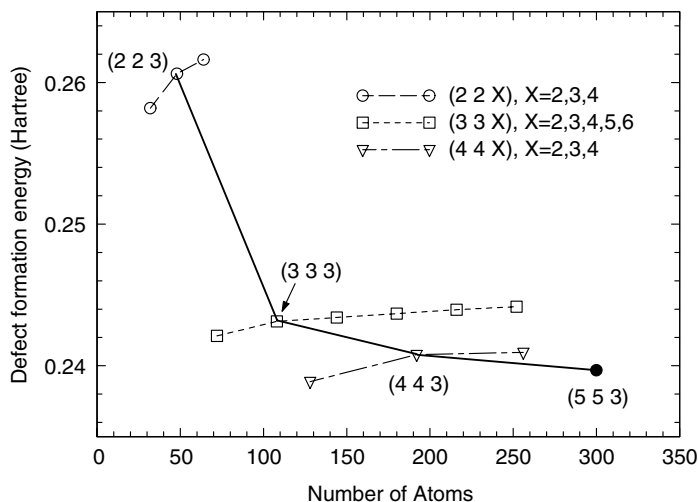


Figure 54 Dependence of the formation energy of the axial $\text{BeO}:[\text{Li}]^0$ defect with size and shape of the adopted supercell. $(i\ j\ k)$ are the expansion coefficients of the primitive lattice basis vectors.

It is hard to believe that a cluster model would give reliable results when relaxation, polarization, and long-range electrostatic interactions play an important and competitive role, because border effects are expected to alter the relative energies by an amount that is orders of magnitude larger than the relative stabilities being investigated.

Carbon Substitution in Silicon: A Supercell Versus Cluster Investigation

As a last example, we consider another simple defect: the carbon substitution in bulk silicon.^{263,264} In this case, however, we will not only consider the convergence properties of the supercell approach but also compare the results of the cluster and supercell schemes. Calculations were performed at the HF level with a 6-21G basis set plus polarization functions for C and Si and a 2-1G basis set for H (the latter was used in the cluster calculations).

We consider first the convergence of the results with respect to the supercell size. Four supercells with 8 (S_4), 16 (S_8), 32 (S_{16}), and 64 (S_{32}) atoms (the last is shown in Figure 55) are considered, all with the cubic symmetry. As in previous examples, to investigate how far the perturbation propagates, an increasing number of defect neighbors has subsequently been allowed to relax in each supercell.

The stars of neighbors completely contained in the unit cell, and the number of atoms belonging to a star (in parentheses) for the four supercells are I (4), I (4), I + II (4 + 12), and I + II + III + V (4 + 12 + 12 + 12), respectively. Notice that in S_8 , next-nearest neighbors are shared with defects in neighboring cells. In the S_{32} supercell, the atoms of star IV are at special positions and cannot relax.

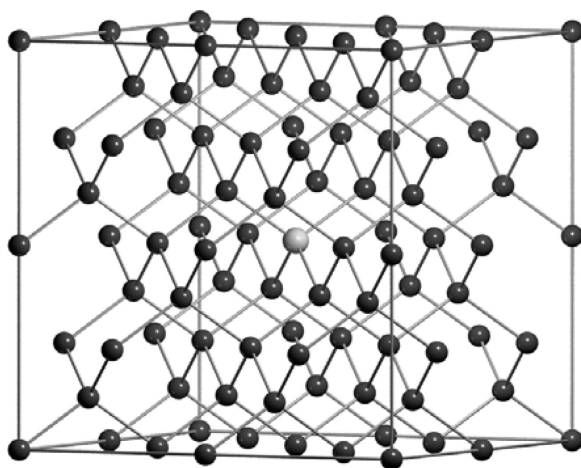


Figure 55 A 64-atom supercell (S_{32}) model of a carbon impurity in bulk silicon.

Table 30 Defect Formation Energies (in kJ/mol) for a Carbon Substitutional Impurity in Silicon, as a Function of Supercell and Cluster Size

	Unrelaxed	I	II	III	IV	V	Fully Relaxed
Supercell							
S ₄	222.6						105.1
S ₈	223.6	100.4					92.3
S ₁₆	223.2	59.0	24.4				9.7
S ₃₂	223.0	60.1	28.5	25.8		12.5	12.4
Cluster							
CSi ₄ H ₁₂	220.5	56.3					
CSi ₃₄ H ₃₆	230.1	97.2	49.1	50.6			
CSi ₈₆ H ₇₆	225.4	68.1	39.8	40.1	41.5	6.5	

Relaxation effects are taken into account by including increasing stars of neighbors of the carbon impurity.

The substitutional defect formation energy, ΔE , computed with respect to atomic energies according to Eq. [96], is reported in Table 30. The Si and C atomic energies are -288.812622 and -37.654208 hartree, respectively.

Carbon has both a higher electronegativity and a smaller covalent radius than does silicon, so a large charge transfer and atomic relaxation is foreseen. The former feature is expected to polarize the charge distribution in the cell, with a charge alternation between subsequent stars of neighbors and relatively strong electrostatic interactions among defects in neighboring cells, at least for small supercells. Table 31 shows that indeed this polarization occurs, with a huge difference in the Mulliken net charge of the central carbon (-0.7 electrons) atom with respect to its four nearest neighbors. Charge oscillations, however, damp down rapidly; in the S₃₂ supercell, the Mulliken net charge of the second neighbors is as small as -0.018 electrons, and third and fourth

Table 31 Mulliken Net Charges for a Carbon Substitutional Impurity in Silicon, as a Function of Supercell and Cluster Size

	C	Si ^I	Si ^{II}	Si ^{III}	Si ^{IV}	Si ^V
Supercell						
S ₄	-0.644	0.210	-0.065 ^a			
S ₈	-0.661	0.219	-0.035 ^a			
S ₁₆	-0.758	0.237	-0.017	0.001	0.002 ^a	
S ₃₂	-0.755	0.237	-0.018	-0.003	0.001	0.002
Cluster						
CSi ₄ H ₁₂	-0.738	0.575 ^b				
CSi ₃₄ H ₃₆	-0.723	0.166	0.102 ^b	0.118 ^b		
CSi ₈₆ H ₇₆	-0.746	0.235	-0.038	-0.023	-0.027	0.109 ^b

Net charges refer to fully relaxed supercell structures whereas clusters are partially relaxed up to first, third, and fifth nearest-neighbors of CSi₄H₁₂, CSi₃₄H₃₆, and CSi₈₆H₇₆, respectively.

^aIncomplete star of neighbors.

^bSilicon atoms bonded to one or more hydrogens.

nearest neighbors are almost neutral. These data refer to the relaxed solution, but results are similar in the unrelaxed calculations, which helps us understand why the unrelaxed defect formation energy is essentially the same for the various supercells (first column in Table 30: numbers differ by less than 1 kJ/mol): The defect is already screened effectively at the nearest neighbor level, so that the electrostatic defect–defect interaction is essentially null even with small cells (in the S_4 supercell, for example, the defect–defect distance is as small as 5.52 Å). This nearly perfect screening is also a consequence of symmetry: The defect zone has zero dipole and quadrupole.

When relaxation is taken into account, however, the defect perturbation propagates farther away, and convergence of the defect substitutional energy is slower.

The structural relaxation is large, and the process is dominated by modifications in the covalent network with no dependence on electrostatic effects. The largest structural change involves nearest neighbors as is shown in Table 32. The C–Si¹ bond length reduces by 0.312 Å with respect to the bulk Si–Si

Table 32 Relaxation Effects in a Carbon Substitutional Impurity in Bulk Silicon as a Function of Supercell and Cluster Size

	<i>N</i>	I	II	III	IV	V
	<i>R</i>	2.390	3.903	4.577	5.520	6.015
Supercell						
S_4	1	−0.205				
S_8	1	−0.213				
	fr ^a	−0.217				
S_{16}	1	−0.261				
	2	−0.300	−0.066			
	fr ^a	−0.315	−0.078	0.018		
S_{32}	1	−0.259				
	2	−0.300	−0.065			
	3	−0.300	−0.065	−0.003		
	5	−0.313	−0.081	−0.002		−0.038
	fr ^a	−0.312	−0.082	−0.002		−0.040
Cluster						
CSi_4H_{12}	1	−0.208				
$CSi_{34}H_{36}$	1	−0.237				
	2	−0.279	−0.058			
	3	−0.278	−0.062	−0.016		
$CSi_{86}H_{76}$	1	−0.254				
	2	−0.292	−0.058			
	3	−0.291	−0.056	0.007		
	4	−0.291	−0.056	0.009	0.014	
	5	−0.306	−0.072	0.010	0.014	−0.038

This table gives the variation (in Å) of the distance R between the defect and its neighbors (N in Roman numerals). Relaxation effects are taken into account by including increasing stars of neighbors (Arabic numerals) of the carbon impurity.

^aFull relaxation in the supercell.

distance, from 2.390 to 2.078 Å, whereas the Si^I-Si^{II} bond elongates to 2.446 Å. When only the nearest neighbors are allowed to relax, the energy gain is 120 kJ/mol for S_4 and S_8 , which increases to 163 kJ/mol in the S_{16} and S_{32} supercell. A further gain of about 30 kJ/mol is obtained by relaxing the next-nearest neighbors (this is possible only in S_{16} and S_{32}). Relaxation of the third nearest neighbors is small and results in essentially no energy gain, whereas a further 13 kJ/mol is obtained by relaxing the fifth nearest neighbors. Full relaxation yields a further small energy gain.

Full relaxation of S_{16} reduces ΔE to 9.7 kJ/mol, close to the value obtained with the fully relaxed S_{32} supercell. Thus, from the point of view of the convergence of defect properties, the present example is similar to the F-center in alkali halides previously discussed, where a relatively small supercell (S_{16}) is large enough to “contain” all the defect perturbation.

Let us now investigate the same problem with a cluster model.²⁶⁴ Clusters containing 5, 35, and 87 silicon atoms have been considered; they are referred to as small, medium, and large in Figure 56. Dangling bonds were saturated with hydrogen atoms along the Si-Si directions of the perfect crystal. The Si-H distance was kept constant at 1.46 Å during the optimization of all cluster atoms (for this reason clusters in the tables are not “fully relaxed”). The medium and large clusters were constructed subject to the constrain that silicon atoms at the cluster surface are connected to no more than two hydrogen atoms. The total number of atoms in the three clusters is then 17, 71, and 163. Computational conditions are the same for cluster and supercell models. The defect formation energies, Mulliken net charges, and structural relaxation effects as evaluated with the cluster models are given in the lower part of Tables 30, 31, and 32, respectively.

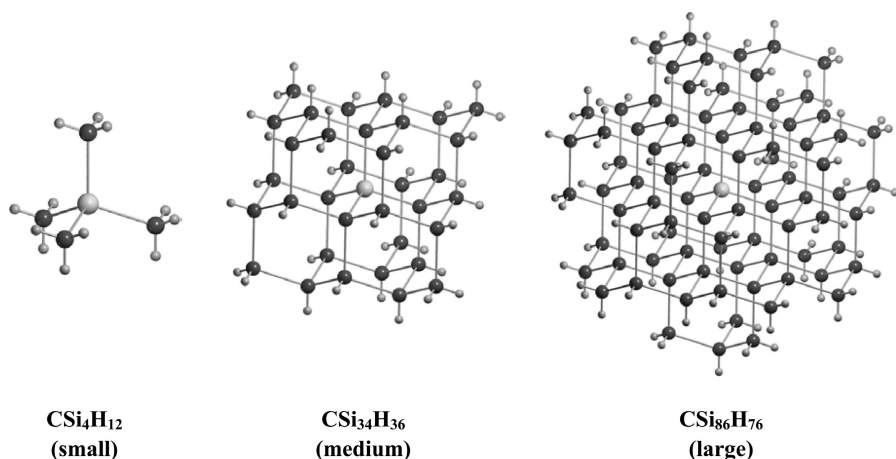


Figure 56 Adopted cluster models of the carbon impurity in bulk silicon.

The defect formation energies for the unrelaxed clusters are similar to those calculated by the supercell approach, even in the case of small clusters. The same screening mechanism, already discussed for the supercell models, is active also in the cluster calculations.

When relaxation effects are taken into account, the defect perturbation extends farther from the impurity into regions where the screening of border effects (H saturation) is only partial. The cluster defect substitutional energy differs from the S_{32} datum by -3.8 (small), 37.1 (medium), and 8.1 (large) kJ/mol when only the nearest neighbors are allowed to relax, and by 20.6 (medium) and 11.3 (large) kJ/mol when next-nearest neighbors can relax. Atomic charges in Table 31 confirm that the positive charge on the first Si neighbors compensates the negative charge on carbon, which makes the electrostatic contribution short-ranged. However, closer inspection of Table 31 shows that only for the largest cluster do net charges damp down as in the supercell. In fact, silicon atoms close to the border H atoms are positively charged, and this is expected to perturb their interaction to move toward the cluster center. Eventually, as regards the defect formation energies, the largest supercell and cluster models data are reasonably close to each other.

It is worth noting that if the hydrogen atoms are allowed to relax, a dramatic change in the structure originates, and the formation energy becomes negative. Fixed, saturating hydrogen atoms force the cluster to retain the memory of the bulk geometry.

The comparison between supercell and cluster approaches shows that the cluster size is crucial to derive accurate results and care must be taken to account for border effects. Only the largest cluster considered here (86 silicon atoms) is adequate for describing relaxation and defect formation energy properly, whereas a S_{16} (32-atom) supercell is already large enough.

Larger differences between the supercell and the cluster scheme may appear when other properties related to the infinite nature of the perturbed crystalline system are analyzed. In Figure 57, on the left, the band structure of defective S_{32} supercell is shown and, on the right, the energy levels of the $CSi_{86}H_{76}$ cluster are shown (the energy scale is shifted in such a way that the 1s level of carbon of the two systems coincide). In the present example, no defect states are present in the gap; the computed band gap is 6.38 eV for the defective S_{32} supercell, to be compared with the 8.8 eV HOMO-LUMO gap of the cluster.

These examples show that the supercell approach is an accurate and, in many cases, relatively cheap tool for the study of neutral defects in crystalline systems, once properly gauged with respect to supercell size.

The supercell approach, as implemented in CRYSTAL, has been applied to the study of many different bulk and surface defective systems. These include Ca and Be substitution in bulk MgO ,²⁶⁵ F-center in CaF_2 ,²⁶⁶ Fe doped NiO ,²⁶⁷ Li doped NiO ,²⁶⁸ V doped TiO_2 ,²⁶⁹ and Ti substitution in an all-silica Chabazite.^{270,271} An example of reactivity of a surface defect has been

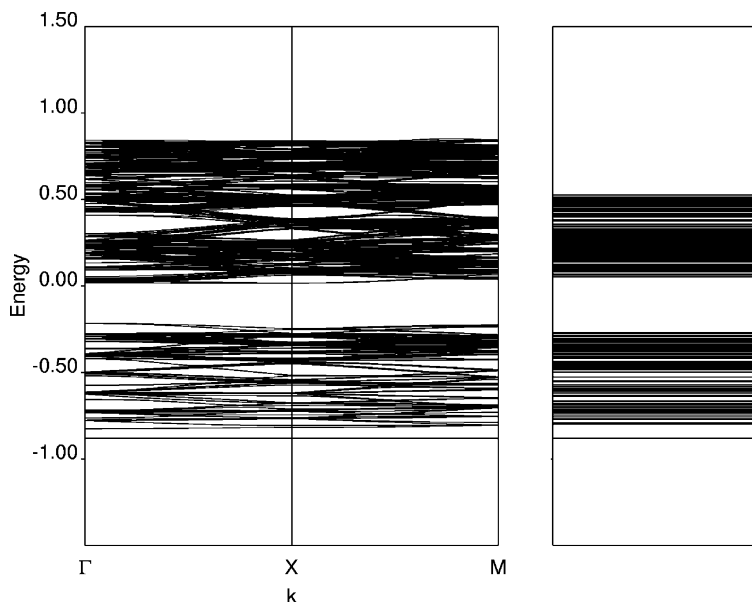


Figure 57 Band structure of the fully relaxed carbon doped S_{32} silicon supercell (left) and energy levels of the $\text{CSi}_{86}\text{H}_{76}$ cluster (right). In the cluster, atomic positions were relaxed up to the fifth nearest neighbors of the central carbon atom. The cluster energy levels are shifted so that the lowest level of both systems coincide.

reported by Orlando et al.,²⁷² where they studied the hydrogen abstraction from methane by Li doped MgO. An interesting application in the modeling of extended defects has been reported recently by Gruen et al.²⁷³ in which the growth of crystalline diamond through planar defects was investigated. Convergence properties of the cluster model in the study of local perturbations has also been studied in ionic systems as in the case of bulk defects in MgO.²⁷⁴

ACKNOWLEDGMENTS

We would like to acknowledge many fruitful discussions and interactions with Cesare Pisani. The authors wish also to thank Piero Ugliengo for providing some figures and assisting with the production of this chapter and for many helpful discussions.

APPENDIX 1: AVAILABLE PERIODIC PROGRAMS

Many periodic codes are mentioned in the literature, mostly based on either a plane waves basis set and pseudopotentials or projector-augmented waves. Some of this software can be purchased, and the rest is available through collaboration with the main development team or downloadable

Table A1.1 List of Available Solid State ab initio Computer Programs

Program	Description	Web site	Refs
ABINIT	DFT(LDA,GGA); TD-DFT; NCPP; PW; PAW; TE; GO; PH	www.abinit.org	163
CASTEP	DFT(LDA,GGA); PP; PW; TE; GO; CP-MD	www.accelrys.com/mstudio/ ms_modeling/castep.html	275
CPMD	DFT(LDA,GGA); NCPP; PW; TE; GO; CP-MD	www.cpmc.org	276
Dacapo	DFT(LDA,GGA); PP; PW; TE; GO	www.fysik.dtu.dk/CAMP/daca- po.html	
DoD-Planewave	DFT(LDA,GGA); PP; PW; TE; GO	cst-www.nrl.navy.mil/people/ singh/planewave/	
FHI98md	DFT(LDA,GGA); NCPP; PW; TE; GO; BO-MD	www.fhi-berlin.mpg.de/th/ fhi98md/index.html	277
PARATEC	DFT(LDA,GGA); TD-DFT; NCPP; PW; TE; GO	www.nersc.gov/projects/para- tec/	278
PWSCF	DFT (LDA,GGA); DF-PT; NCPP; PW; TE; GO; PH; CP- MD	www.pwscf.org	279
VASP	DFT (LDA,GGA); USPP; PW; PAW; TE; GO; PH; CP-MD	cms.mpi.univie.ac.at/vasp/	280
CP-PAW	DFT(LDA,GGA); PAW; TE; GO; CP-MD	www.pt.tu-clausthal.de/~paw/ index.html	281
PWPAW	DFT(LDA); PAW; TE; GO	www.wfu.edu/~natalie/papers/ pwpaw/man.html	282, 283
QUICKSTEP/ CP2K	DFT(LDA,GGA); PP; hybrid GTO/PW	cp2k.berlios.de	284
SIESTA	DFT(LDA,GGA); PP; NTO; TE; GO; MD	www.uam.es/departamentos/ ciencias/fismateriac/siesta/	285
DMol ³	DFT(LDA,GGA); AE; NTO; TE; GO	www.accelrys.com/mstudio/ ms_modeling/dmol3.html	286
LmtART	DFT; AE; LMTO; TE; GO; PH	physics.njit.edu/~savrasov/Pro- grams/index_lmtart.htm	164
FLEUR	DFT; AE; FLAPW; TE	www.flapw.de	287
WIEN2K	DFT(LDA,GGA); AE; FLAPW; TE; GO; PH	www.wien2k.at/	288
MOPAC2002	SE; TE; GO	www.schrodinger.com/ Products/mopac.html	
ADF2002 (BAND)	DFT(LDA,GGA); TD-DFT; AE; STO; TE	www.scm.com	289
Gaussian03	HF; DFT; AE; GTO; TE; GO; PH	www.gaussian.com	290
CRYSTAL03	HF; DFT; AE; PP; GTO; TE; GO	www.crystal.unito.it	

AE	All-electron basis set	BO	Born–Oppenheimer approximation
CP	Car–Parrinello method	DFT	Density functional theory
FLAPW	Fully linearized augmented plane wave	GGA	Generalized gradient approximation
GO	Geometry optimization	GTO	Gaussian-type orbitals
HF	Hartree–Fock	LDA	Local density approximation
MD	Molecular dynamics	NCPP	Norm-conserving pseudopotentials
NTO	Numerical type orbitals	PAW	Projector-augmented wave method
PH	Phonons	PP	Pseudopotentials
PT	Perturbation theory	PW	Plane waves
SE	Semi-empirical methods	STO	Slater-type orbitals
TD	Time dependent	TE	Total energy
USPP	Ultra-soft pseudopotentials		

with no restriction. A tentative list of public codes for solid state ab initio calculations is reported in Table A1.1, along with a list of the main functionalities and indication of the corresponding homepage.

APPENDIX 2: PERFORMANCE OF THE PERIODIC PROGRAM CRYSTAL

The cost of a quantum mechanical calculation depends on a large number of variables, of which the hardware available is certainly the most volatile, owing to rapid technological evolution. Also the compiler and compilation options that generate the binary have an influence on the performance of a program, as well as the more specific choice of the computational parameters controlling the accuracy of the computer program. For these reasons, the data reported in this appendix are intended to give only a rough indication of the cost of a periodic calculation and show how computational time scales with the dimensionality of the system, the approximation used, the unit cell, and the basis set size. To achieve this goal, we reconsider some of the examples illustrated before from the point of view of performance using CRYSTAL.⁵⁶

We begin the analysis by comparing periodic calculations of increasing dimensionality with a single molecule calculation of a molecule consisting of the atoms in the unit cell. Data for MgO are represented in Figure A2.1, where the time required for the calculation of the HF total energy and wave function of a MgO molecule (0-D) is compared with the time required for the

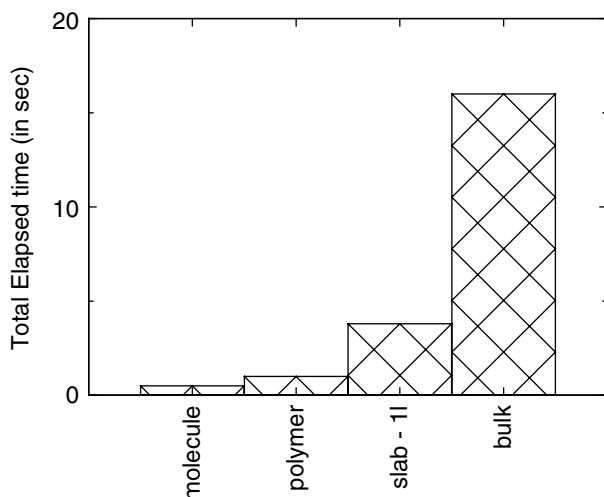


Figure A2.1 Computer time of a CRYSTAL calculation of the HF total energy and wave function for a MgO molecule, polymer, one-layer (001) slab, and bulk.

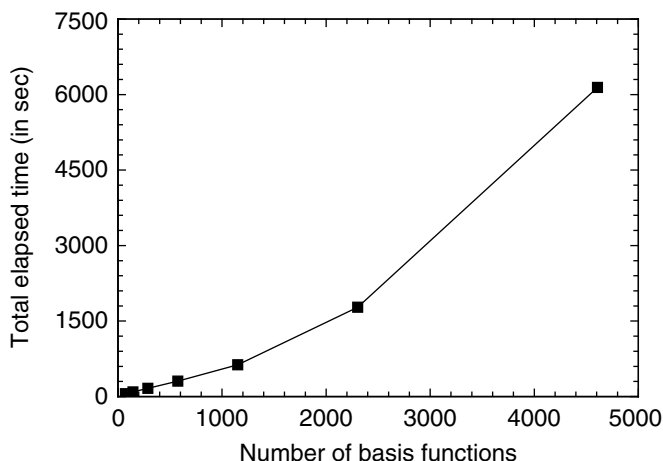


Figure A2.2 Total elapsed time for HF total energy calculations of MgO cubic supercells with 8, 16, 32, 64, 128, 256, and 512 ions. The CRYSTAL program was compiled using the Intel Fortran Compiler IFC7.0 with the `-O2 -tp p7` options. Calculations were carried out with a Pentium Xeon 2.4-GHz single-processor computer, with 2-GB RAM, 512-KB cache, wide SCSI disks.

corresponding polymer (1-D), one-layer (001) slab (2-D), and bulk (3-D). We have used the same basis set, computational conditions, and geometry in all cases.

Cost increases exponentially with the dimensionality of the system, following approximately the progression 1:2:8:30 from 0-D to 3-D. In this simple case, even the bulk calculation takes only a few seconds on a small PC.

The cost of a bulk calculation is primarily a function of the unit cell size. Figure A2.2 shows the total time required for the calculation of the total energy with the MgO supercells that we used in the study of trapped-hole centers. We are considering the supercells before creating the defect. Therefore, the system possesses the full symmetry of the perfect crystal (48 point-symmetry operations). Calculations refer to the S_4 , S_8 , S_{16} , S_{32} , S_{64} , S_{128} , and S_{256} supercells; nine AOs are used for every ion, so that the largest cell contains 4608 basis functions.

A full energy and gradient calculation with 512 ions in the supercell takes less than 2 hours on a low-level PC. Comparing the cost of calculations with supercells of increasing size, we see in the left part of the curve (Figure A2.2) that the elapsed time scales linearly with the number of the basis functions in the supercell up to S_{64} . The departure from linearity at that point corresponds to some nonlinear processes becoming important, in particular the diagonalization of large Fock (or KS) matrices.

However, the MgO supercells are a favorable case for their high point symmetry, of which CRYSTAL takes full advantage. For example, the

computer time spent for a calculation with the S_8 supercell increases by about 20 times when symmetry is neglected, and full geometry optimization of large supercells (S_{64} or S_{128}) containing a trapped-hole center, where only 8 of 48 original point symmetry operations exist, takes a few days on a single PC.

The cost of a calculation can increase also because of basis set enlargement. In particular, the truncation of the infinite series in CRYSTAL is effective for relatively sharp Gaussian functions. In ionic and covalent compounds, the exponents of the most diffuse Gaussians in a double-zeta-type basis set are relatively high, typically between 0.13 and 0.3 bohr⁻², and the corresponding computational effort is not too large. On the contrary, the exponent of the outermost Gaussian in a metal can be smaller than 0.1 bohr⁻², with a dramatic increase in computer time, as a huge amount of one- and two-electron integrals have to be computed, which is also the case for any large molecular basis sets containing diffuse functions with a high angular quantum number used for describing crystalline systems.⁸⁹ As an example, we consider the crystal of urea, with two molecules in the unit cell (16 atoms, 8-point symmetry operations), and we compare the elapsed time for the integral evaluation, SCF iteration, and gradient calculation as a function of the basis set. Six different molecular basis sets have been considered, from 3-21G to 6-311G(d,p). A few details on the basis sets (number of AOs and primitive functions per cell, exponents of the outermost atomic Gaussian) are given in Table A2.1, and results are shown on the right side of Table A2.2. The cost of a typical HF optimization of atomic positions (lattice parameters were fixed at their experimental values)²⁹¹ is also reported.

The 3-21G and 6-21G rows in Table A2.2 are similarly cheap, because the additional core Gaussian function exponents in 6-21G are too large to affect the total cost of the calculation. The higher cost of the 6-31G basis set is caused by the increased number of primitives in the valence shell, and to the smaller exponent of the outermost uncontracted valence Gaussian functions, as shown in Table A2.1. For similar reasons, 6-311G is more expensive than 6-31G. Although d-type functions are usually not diffuse, computing integrals involving d-type AOs is more demanding than with p-type AOs

Table A2.1 Description of the Basis Sets Used for Crystalline Urea

Basis set	N_{AO}^a	N_{γ}^b	$\alpha_{sp}(H)^c$	$\alpha_{sp}(C)^c$	$\alpha_{sp}(N)^c$	$\alpha_{sp}(O)^c$
3-21G	88	144	0.183	0.196	0.283	0.374
6-21G	88	166	0.183	0.196	0.283	0.374
6-31G	88	208	0.161	0.169	0.212	0.270
6-311G	128	248	0.103	0.146	0.201	0.256
6-31G(d,p)	152	280	0.161 (1.100)	0.169 (0.800)	0.212 (0.800)	0.270 (0.800)
6-311G(d,p)	192	320	0.103 (0.750)	0.146 (0.626)	0.201 (0.913)	0.256 (1.292)

^aNumber of basis functions.

^bNumber of primitive Gaussians.

^cExponent of the outermost sp Gaussian (exponent of polarization functions in parentheses).

Table A2.2 Elapsed Time (in sec) for Hartree–Fock Calculations of Urea Molecular Dimer and Crystal

Basis set	Molecular			Crystal				
	t_{INT}^a	t_{SCF}^b	t_{GRAD}^c	t_{INT}^a	t_{SCF}^b	t_{GRAD}^c	$t_{\text{OPT}}(N_{\text{step}})^d$	$t_{\text{OPT}}/N_{\text{step}}^e$
3-21G	3	5	11	13	13	43	853 (13)	65
6-21G	4	5	12	14	13	45	833 (12)	69
6-31G	5	7	24	30	20	124	2765 (15)	184
6-311G	15	21	58	135	66	466	8398 (13)	645
6-31G(d,p)	24	32	103	72	67	318	5673 (13)	457
6-311G(d,p)	53	79	199	263	251	973	18267 (13)	1405

With an AMD Athlon 2.8-GHz single-processor computer, 1-GB RAM, 512-KB cache, EIDE disks. Compilation of the program source with release 4.2 of the Portland Group PGF90 compiler, with -O1 -tp athlon options.

^aElapsed time (sec) for the calculation of integrals.

^bElapsed time (sec) for the full self-consistent field cycle.

^cElapsed time (sec) for the calculation of energy gradients.

^dElapsed time (sec) for geometry optimization (number of optimization steps in parentheses).

^eAverage elapsed time (sec) per geometry optimization step.

with the same exponent. In summary, full geometry optimization with the largest basis set is 20 times slower than with the smallest basis set considered. For comparison, the computer time necessary to run similar calculations for a dimer of urea molecules (0-D), with the same geometry as in the crystal unit cell, is also reported on the left side of Table A2.2.

Beside the composition of the basis set, the choice of the Hamiltonian is also important in determining the length of a quantum-mechanical calculation. For example, the time spent in a single point energy plus gradient calculation, i.e., 667 seconds at the Hartree–Fock level (see Table A2.2), becomes 548, 898, and 1535 seconds, respectively, when we use LDA, GGA, and B3LYP, with a pruned grid for numerical integration of the exchange–correlation functional defined by 75 radial points and 494 angular points (the total number of points in the cell is 27,364; such a grid is labeled as LGRID in the CRYSTAL manual).⁵⁶

Because parallel machines are becoming common in routine calculations, we also provide a few examples of parallel calculations. Two versions of parallel CRYSTAL exist: The first is based on a replicated data scheme (PCRYSTAL), whereas the second implements a distributed data algorithm (MPP-CRYSTAL). The most important difference between these versions concerns the Fock (or KS) matrix diagonalization step. Every matrix associated with one \mathbf{k} -point is diagonalized by a single processor in PCRYSTAL, and maximum efficiency is obtained when the number of \mathbf{k} -points in the reciprocal unit cell ($n_{\mathbf{k}}$) is an exact multiple of the number of processors. When $n_{\mathbf{k}}$ is small and the matrices to be diagonalized are large, as for example with large unit cell systems, parallelization with PCRYSTAL may become inefficient with

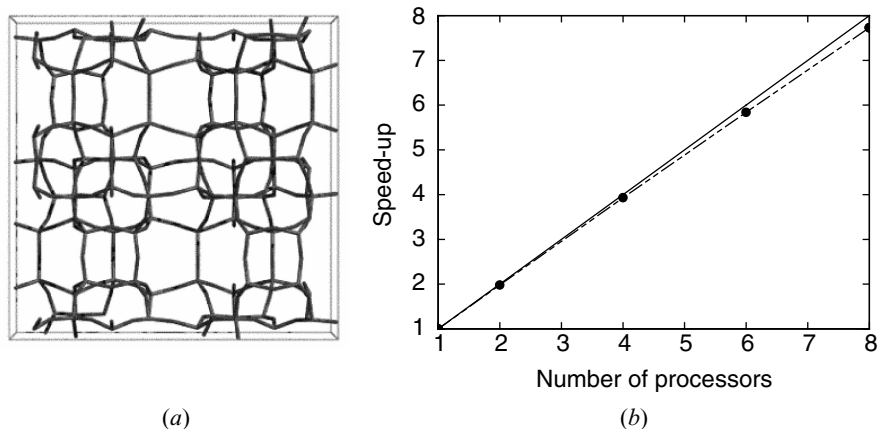


Figure A2.3 (a) Structure of an all-silica zeolite silicalite, MFI framework; (b) Speed-up of the total energy and wavefunction calculation with the number of processors in a cluster of AMD Athlon 1.9-GHz single-processor, 1-GB RAM, 512-KB cache, EIDE disks. The code was compiled with PGF90 v4.2 and `-O1 -tp athlon` options.

any number of processors greater than n_k . MPP-CRYSTAL obviates this problem in massive-parallel computers by distributing every diagonalization task across a large number of processors.

We consider the scaling of PCRYSTAL with the number of active processors for silicalite (MFI framework; see Figure A2.3a), an all silica zeolite with 288 atoms in the unit cell (4416 AOs, 8-point symmetry operations; 8 k-points). Figure A2.3b shows that an almost linear correspondence exists between the number of active processors and execution time. The CPU time decreases from about 23 to 3 hours when distributing the job to eight processors.

MPP-CRYSTAL has been used recently for the calculation of the HF total energy of a small structural protein that has been characterized by X-ray diffraction studies (0.52 Å) to a very high precision: crambin,²⁹² which has $P2_1$ symmetry with two chains per unit cell, 46 aminoacidic residues per chain, and 1284 atoms per cell.

The scaling of such a calculation with the number of active processors of IBM p-series 690 RS6000/P4 1.3 GHz (1240 processors) has been tested on three basis sets of increasing size: STO-3G (3948 AOs), 6-31G (7194 AOs), and 6-31G(d,p) (12354 AOs) at the HPCx Supercomputing Center in Daresbury, (U.K.). Figure A2.4 shows that scalability increases with increasing the basis set size. A total of 1024 active processors speed-up the calculation with the largest basis set by a factor of 700, with the calculation taking about 3 hours to be completed. Almost linear scaling is observed up to 256 processors.

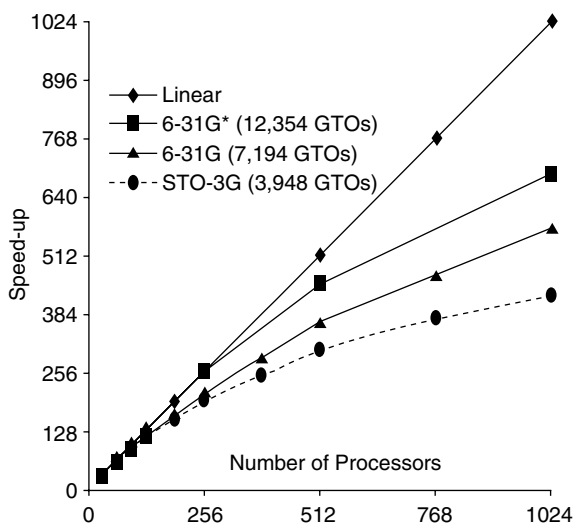


Figure A2.4 Comparison of the CPU time speed-up with the number of processors for three different basis sets of benchmark calculations on crambin (by courtesy of I. J. Bush).

APPENDIX 3: ACRONYMS

AE	All-electron
AFM	Antiferromagnetic
AO	Atomic orbital
APW	Augmented plane waves
B3LYP	Becke 3-parameter exchange-correlation functional
BLYP	Becke and Lee–Yang–Parr exchange-correlation functional
BSSE	Basis set superposition error
BZ	Brillouin zone
CCA	Coupled-cluster approximation
CCSD	CC truncated to singles and doubles substitutions
CCSD(T)	CC truncated to singles, doubles, and (approximated) triples substitutions
CHA	Chabazite
CI	Configuration-interaction
CO	Crystalline orbital
CP	Counterpoise method
DFT	Density functional theory
EDI	Edingtonite
ENDOR	Electron-nuclear double-resonance

EPR	Electron paramagnetic resonance
FAU	Faujasite
FLAPW	Fully linearized augmented plane waves
FM	Ferromagnetic
GGA	Generalized gradient approximation
HF	Hartree-Fock
HOMO	Highest occupied molecular orbital
IR	Irreducible representation
KKR	Korringa-Kohn-Rostoker
KS	Kohn-Sham
LAPW	Linearized augmented-Plane-Waves
LCAO	Linear combination of atomic orbitals
LDA	Local density approximation
LSDA	Local spin-density approximation
LUMO	Lowest unoccupied molecular orbital
MP2	Møller-Plesset second-order perturbation expansion
ONIOM	Our N-layer integrated molecular orbitals—molecular mechanics
OPW	Orthogonalized plane waves
PP	Pseudopotentials
PW	Plane waves
PW91	Perdew-Wang 91 exchange-correlation functional
SOD	Sodalite
SPZ	LDA functional formulation (Slater exchange, Perdew-Zunger correlation)
STO	Slater type orbital
SVWN	LDA functional formulation (Slater exchange, Vosko-Wilk-Nusair correlation)
UHF	Unrestricted Hartree-Fock

REFERENCES

1. R. Colle and O. Salvetti, *Theor. Chim. Acta*, **37**, 329 (1975). Approximate Calculation of Correlation Energy for Closed Shells.
2. E. Wigner, *Phys. Rev.*, **46**, 1002 (1934). On the Interaction of Electrons in Metals.
3. P. Hohenberg and W. Kohn, *Phys. Rev.*, **136**, B864 (1964). Inhomogeneous Electron Gas.
4. W. Kohn and L. J. Sham, *Phys. Rev.*, **140**, A1133 (1965). Self-Consistent Equations Including Exchange and Correlation Effects.
5. L. Hedin and S. Lundqvist, in *Solid State Physics*, Vol. 23, F. Seitz, D. Turnbull, and H. Ehrenreich, Eds., Academic Press, New York, 1969, p. 1. Effects of Electron-Electron and Electron-Phonon Interactions on the One-Electron States of Solids.
6. S. H. Vosko, L. Wilk, and M. Nusair, *Can. J. Phys.*, **58**, 1200 (1980). Accurate Spin-dependent Electron Liquid Correlation Energies for Local Spin Density Calculations: A Critical Analysis.
7. J. P. Perdew and A. Zunger, *Phys. Rev.*, **B23**, 5048 (1981). Self-Interaction Correction to Density Functional Approximations for Many-Electron Systems.

8. V. R. Saunders, in *Computational Techniques in Quantum Chemistry and Molecular Physics*, Vol. 15, G. H. F. Diercksen, B. T. Sutcliffe, and A. Veillard, Eds., Reidel, Dordrecht, the Netherlands, NATO ASI Series C, 1975, p. 347. An Introduction to Molecular Integral Evaluation.
9. V. R. Saunders, in *Methods in Computational Molecular Physics*, Vol. 113, G. H. F. Diercksen and S. Wilson, Eds., Reidel, Dordrecht, the Netherlands, NATO ASI Series C, 1983, p. 1. Molecular Integrals for Gaussian Type Functions.
10. C. F. Bender, *Phys. Rev.*, **183**, 23 (1969). Studies in Configuration Interaction: The First-Row Diatomic Hydrides.
11. W. Meyer, *Int. J. Quantum Chem. Symp.*, **5**, 341 (1971). Ionization Energies of Water from PNO-CI Calculations.
12. P. J. Hay and I. Shavitt, *J. Chem. Phys.*, **60**, 2865 (1974). Ab Initio Configuration Interaction Studies of the π -electron States of Benzene.
13. R. Ahlrichs, H. Lischka, V. Stämmler, and W. Kutzelnigg, *J. Chem. Phys.*, **62**, 1225 (1975). PNO-CI (Pair Natural Orbital Configuration Interaction) and CEPA-PNO (Coupled Electron Pair Approximation with Pair Natural Orbitals) Calculations of Molecular Systems. I. Outline of the Method for Closed-Shell States.
14. V. R. Saunders and J. H. Van Lenthe, *Mol. Phys.*, **48**, 923 (1983). The Direct CI. A Detailed Analysis.
15. P. Pulay, *Mol. Phys.*, **17**, 197 (1969). Ab Initio Calculation of Force Constants and Equilibrium Geometries in Polyatomic Molecules.
16. R. Krishnan, H. B. Schlegel, and J. A. Pople, *J. Chem. Phys.*, **72**, 4654 (1980). Derivative Studies in Configuration-Interaction Theory.
17. E. Clementi and A. Veillard, IBMOL, Computation of Wavefunction for Molecules of General Geometry Using the LGCO-MO-SCF Method. QCPE program number 92, 1966, Quantum Chemistry Program Exchange, Indiana University, Bloomington, Indiana.
18. W. J. Hehre, W. A. Lathan, R. Ditchfield, M. D. Newton, and J. A. Pople, GAUSSIAN 70, QCPE program number 237, 1970, Quantum Chemistry Program Exchange, Indiana University, Bloomington, Indiana.
19. F. Bassani, G. Pastori Parravicini, and R. A. Ballinger, *Electronic States and Optical Transitions in Solids*, Pergamon Press, Oxford, 1975.
20. V. L. Moruzzi, J. F. Janak, and A. R. Williams, *Calculated Electronic Properties of Metals*, Pergamon Press, New York, 1978.
21. D. R. Hamann, *Phys. Rev. Lett.*, **42**, 662 (1979). Semiconductor Charge Densities with Hard-Core and Soft-Core Pseudopotentials.
22. D. R. Hamann, M. Schlüter, and C. Chang, *Phys. Rev. Lett.*, **43**, 1494 (1979). Norm-Conserving Pseudopotentials.
23. A. Zunger, *Phys. Rev.*, **B21**, 4785 (1980). Ground-State Properties of Crystalline Silicon in a Density-Functional Pseudopotential Approach.
24. G. B. Bachelet, D. R. Hamann, and M. Schlüter, *Phys. Rev.*, **B26**, 4199 (1982). Pseudopotentials that work: From H to Pu.
25. J. C. Slater, in *Computational Methods in Band Theory*, P. Marcus, J. F. Janak, and A. R. Williams, Eds., Plenum Press, New York, 1971, p. 447. The Self-Consistent Field Method for Crystals.
26. J. Korrington, *Physica*, **13**, 392 (1947). On the Calculation of the Energy of a Bloch Wave in a Metal.
27. W. Kohn and N. Rostoker, *Phys. Rev.*, **94**, 1111 (1954). Solution of the Schrödinger Equation in Periodic Lattices with an Application to Metallic Lithium.
28. C. Herring, *Phys. Rev.*, **57**, 1169 (1940). A New Method for Calculating Wave Functions in Crystals.
29. J. C. Slater, *Phys. Rev.*, **92**, 603 (1953). An Augmented Plane Wave Method for Periodic Potential Problem.

30. M. M. Saffren and J. C. Slater, *Phys. Rev.*, **92**, 1126 (1953). An Augmented Plane-Wave Method for the Periodic Potential Problem. II.
31. O. K. Andersen, *Phys. Rev.*, **B12**, 3060 (1975). Linear Methods in Band Theory.
32. J. R. Leite, B. I. Bennett, and F. Herman, *Phys. Rev.*, **B12**, 1466 (1975). Electronic Structure of the Diamond Crystal Based on an Improved Cellular Calculation.
33. A. Zunger and A. J. Freeman, *Int. J. Quantum Chem. Symp.*, **10**, 383 (1976). Combined Fourier Transform and Discrete Variational Method Approach to the Self-Consistent Solution of the Electronic Band Structure Problem within the Local Density Formalism.
34. C. R. A. Catlow and W. C. Mackrodt, *Computer Simulation of Solids*, Springer-Verlag, Berlin, Germany, 1982.
35. J. M. André, L. Gouverneur, and G. Leroy, *Int. J. Quantum Chem.*, **1**, 427 (1967). L'Etude Théorique des Systèmes Périodiques. I. La Méthode LCAO-HCO.
36. J. M. André, L. Gouverneur, and G. Leroy, *Int. J. Quantum Chem.*, **1**, 451 (1967). L'Etude Théorique des Systèmes Périodiques. II. La Méthode LCAO-SCF-CO.
37. F. E. Harris and H. J. Monkhorst, *Phys. Rev. Lett.*, **23**, 1026 (1969). Complete Calculations of the Electronic Energies of Solids.
38. G. Del Re, J. Ladik, and G. Biczó, *Phys. Rev.*, **155**, 997 (1967). Self-Consistent-Field Tight-Binding Treatment of Polymers. I. Infinite Three-Dimensional Case.
39. H. Stoll and H. Preuss, *Phys. Status Solidi*, **60**, 185 (1973). Convergence of Lattice Sums in Hartree-Fock LCAO Calculations.
40. H. Stoll and H. Preuss, *Int. J. Quantum Chem.*, **IX**, 775 (1975). Hartree-Fock Calculation of Cohesive Energies and Equilibrium Lattice Constants for Solid Li and Be.
41. F. E. Harris, in *Advances and Perspectives in Theoretical Chemistry*, Vol. 2, H. Eyring and D. Henderson, Eds., Academic Press, New York, 1975, p. 147. Hartree-Fock Studies of Electronic Structures of Crystalline Solids.
42. R. N. Ewema, *Phys. Rev.*, **B7**, 818 (1972). General Crystalline Hartree-Fock Formalism: Diamond Results.
43. R. N. Ewema, G. T. Surratt, D. L. Willhite, and G. G. Wepfer, *Philos. Mag.*, **29**, 1033 (1974). Hartree-Fock Electron Distribution of Cubic BN.
44. C. Pisani and R. Dovesi, *Int. J. Quantum Chem.*, **17**, 501 (1980). Exact Exchange Hartree-Fock Calculations for Periodic Systems. I. Illustration of the Method.
45. R. Dovesi, C. Pisani, C. Roetti, M. Causà, and V. R. Saunders, CRYSTAL88, an Ab Initio All-Electron LCAO Hartree-Fock Program for Periodic Systems. QCPE program number 577, 1989, Quantum Chemistry Program Exchange, Indiana University, Bloomington, Indiana.
46. L. Bellaiche and D. Vanderbilt, *Phys. Rev.*, **B61**, 7877 (2000). Virtual Crystal Approximation Revisited: Application to Dielectric and Piezoelectric Properties of Perovskites.
47. N. J. Ramer and A. M. Rappe, *J. Phys. Chem. Solids*, **61**, 315 (2000). Application of a New Virtual Crystal Approach for the Study of Disordered Perovskites.
48. S. W. De Leeuw, J. W. Perram, and E. R. Smith, *Proc. R. Soc. Lond. A*, **373**, 27 (1980). Simulation of Electrostatic Systems in Periodic Boundary Conditions. I. Lattice Sums and Dielectric Constants.
49. S. W. De Leeuw, J. W. Perram, and E. R. Smith, *Proc. R. Soc. Lond. A*, **373**, 57 (1980). Simulation of Electrostatic Systems in Periodic Boundary Conditions. II. Equivalence of Boundary Conditions.
50. E. R. Smith, *Proc. R. Soc. Lond. A*, **375**, 475 (1981). Electrostatic Energy in Ionic Crystals.
51. E. R. Smith, *Proc. R. Soc. Lond. A*, **381**, 241 (1982). Effects of Surface Charge on the Electrostatic Energy of an Ionic Crystal.
52. P. P. Ewald, *Ann. Phys. (Leipzig)*, **64**, 253 (1921). Die Berechnung Optischer und Elektrostatischer Gitterpotentiale.

53. F. E. Harris and H. J. Monkhorst, *Phys. Rev.*, **B2**, 4400 (1970). Electronic-Structure Studies of Solids. I. Fourier Representation Method for Madelung Sums.
54. V. R. Saunders, C. Freyria-Fava, R. Dovesi, L. Salasco, and C. Roetti, *Mol. Phys.*, **77**, 629 (1992). On the Electrostatic Potential in Crystalline Systems where the Charge Density is Expanded in Gaussian Functions.
55. V. R. Saunders, C. Freyria-Fava, R. Dovesi, and C. Roetti, *Comput. Phys. Commun.*, **84**, 156 (1994). On the Electrostatic Potential in Linear Periodic Polymers.
56. V. R. Saunders, R. Dovesi, C. Roetti, R. Orlando, C. M. Zicovich-Wilson, N. M. Harrison, K. Doll, B. Civalieri, I. J. Bush, P. D'Arco, and M. Llunell, CRYSTAL03 User's Manual, 2003, Università di Torino, Torino, Italy.
57. A. R. Oganov, J. P. Brodholt, and D. Price, in *Energy Modelling in Minerals*, Vol. 4, C. M. Gramaccioli, Ed., Eötvös University Press, Budapest, EMU Notes in Mineralogy, 2002, p. 83. Ab Initio Theory of Phase Transitions and Thermoelasticity of Minerals.
58. R. Car and M. Parrinello, *Phys. Rev. Lett.*, **55**, 2471 (1985). Unified Approach for Molecular Dynamics and Density-Functional Theory.
59. F. Mauri, B. G. Pfommer, and S. G. Louie, *Phys. Rev. Lett.*, **77**, 5300 (1996). Ab Initio Theory of NMR Chemical Shifts in Solids and Liquids.
60. P. Umari, A. Pasquarello, and A. Dal Corso, *Phys. Rev.*, **B63**, 094305 (2001). Raman Scattering Intensities in Alpha-Quartz: A First-Principles Investigation.
61. M. Veithen, X. Gonze, and P. Ghosez, *Phys. Rev. Lett.*, **93**, 187401 (2004). First-Principles Study of the Electrooptic Effect in Ferroelectric Oxides.
62. M. Schütz, G. Hetzer, and H. J. Werner, *J. Chem. Phys.*, **111**, 5691 (1999). Low-Order Scaling Local Electron Correlation Methods. I. Linear Scaling Local MP2.
63. M. Schütz, *Phys. Chem. Chem. Phys.*, **4**, 3941 (2002). A New, Fast, Semi-Direct Implementation of Linear Scaling Local Coupled Cluster Theory.
64. N. Marzari and D. Vanderbilt, *Phys. Rev.*, **B56**, 12847 (1997). Maximally Localized Generalized Wannier Functions for Composite Energy Bands.
65. C. M. Zicovich-Wilson, R. Dovesi, and V. R. Saunders, *J. Chem. Phys.*, **115**, 9708 (2001). A General Method to obtain Well Localized Wannier Functions for Composite Energy Bands in Linear Combination of Atomic Orbital Periodic Calculations.
66. C. Pisani, M. Busso, G. Capocchi, S. Casassa, R. Dovesi, L. Maschio, V. R. Saunders, C. M. Zicovich-Wilson, and M. Schütz, *in preparation*, Local-MP2 Electron Correlation Method for Non Conducting Crystals.
67. A. Lüchow and J. B. Anderson, *Annu. Rev. Phys. Chem.*, **51**, 501 (2000). Monte Carlo Methods in Electronic Structures for Large Systems.
68. S. Suhai, *Phys. Rev.*, **B27**, 3506 (1983). Quasiparticle Energy-Band Structures in Semiconducting Polymers: Correlation Effects on the Band Gap in Polyacetylene.
69. J. Q. Sun and R. J. Bartlett, *J. Chem. Phys.*, **104**, 8553 (1996). Second-Order Many-Body Perturbation-Theory Calculations in Extended Systems.
70. Q. Y. Ayala, K. N. Kudin, and G. E. Scuseria, *J. Chem. Phys.*, **115**, 9698 (2001). Atomic Orbital Laplace-Transformed Second-Order Møller-Plesset Theory for Periodic Systems.
71. H. Stoll, *Phys. Rev.*, **B46**, 6700 (1992). Correlation Energy of Diamond.
72. H. Stoll, *Chem. Phys. Lett.*, **191**, 548 (1992). The Correlation Energy of Crystalline Silicon.
73. K. Doll, M. Dolg, P. Fulde, and H. Stoll, *Phys. Rev.*, **B52**, 4842 (1995). Correlation Effects in Ionic Crystals: The Cohesive Energy of MgO.
74. K. Doll and H. Stoll, *Phys. Rev.*, **B56**, 10121 (1997). Cohesive Properties of Alkali Halides.
75. A. Shukla, M. Dolg, P. Fulde, and H. Stoll, *Phys. Rev.*, **B60**, 5211 (1999). Wave-Function-Based Correlated Ab Initio Calculations on Crystalline Solids.
76. E. Runge and E. K. U. Gross, *Phys. Rev. Lett.*, **52**, 997 (1984). Density-Functional Theory for Time-Dependent Systems.

77. M. E. Casida, in *Recent Developments and Applications of Modern Density Functional Theory*, Vol. 4, J. Seminario, Ed., Elsevier, Amsterdam, Theoretical and Computational Chemistry, 1996, p. 391. Time-dependent Density Functional Response Theory of Molecular Systems: Theory, Computational Methods, and Functionals.
78. M. Petersilka and E. K. U. Gross, *Int. J. Quantum Chem.*, **60**, 181 (1996). Spin-Multiplet Energies from Time-Dependent Density Functional Theory.
79. L. Bernasconi, M. Sprik, and J. Hutter, *Chem. Phys. Lett.*, **394**, 141 (2004). Hartree-Fock Exchange in Time Dependent Density Functional Theory: Application to Charge Transfer Excitations in Solvated Molecular Systems.
80. M. S. Hybertsen and S. G. Louie, *Phys. Rev. Lett.*, **55**, 1418 (1985). First-Principle Theory of Quasiparticles: Calculations of Band Gaps in Semiconductors and Insulators.
81. M. Rohlfing, P. Krüger, and J. Pollmann, *Phys. Rev.*, **B52**, 1905 (1995). Efficient Scheme for GW Quasiparticle Band-Structure Calculations.
82. S. Albrecht, L. Reining, R. Del Sole, and G. Onida, *Phys. Rev. Lett.*, **80**, 4510 (1998). Ab Initio Calculation of Excitonic Effects in the Optical Spectra of Semiconductors.
83. B. Arnaud and M. Alouani, *Phys. Rev.*, **B62**, 4464 (2000). All-Electron Projector-Augmented-Wave GW Approximation: Application to the Electronic Properties of Semiconductors.
84. S. Lebègue, B. Arnaud, M. Alouani, and P. E. Blöchl, *Phys. Rev.*, **B67**, 155208 (2003). Implementation of an All-Electron GW Approximation Based on the Projector Augmented Wave Method without Plasmon Pole Approximation to Si, SiC, AlAs, InAs, NaH and KH.
85. A. W. Hewat and C. Riekel, *Acta Crystallogr. Sec. A*, **35**, 569 (1979). The Crystal Structure of Deuteroammonia between 2 and 180 K by Neutron Powder Profile Refinement.
86. M. F. C. Ladd, *Symmetry in Molecules and Crystals*, Ellis Horwood, New York, 1989.
87. T. Hahn, Ed., *International Tables of Crystallography*, Vol. A, 5th ed., Kluwer Academic Publishers, Dordrecht, the Netherlands, 2002.
88. F. Bloch, *Z. Phys.*, **52**, 555 (1928). Über die Quantenmechanik der Electronen in Kristallgittern.
89. C. Pisani, R. Dovesi, and C. Roetti, *Hartree-Fock Ab Initio Treatment of Crystalline Systems*, Springer, Berlin, 1988.
90. P. A. M. Dirac, *Proc. Cambridge Philos. Soc.*, **26**, 376 (1930). Note on Exchange Phenomena in the Thomas Atom.
91. A. D. Becke, *J. Chem. Phys.*, **98**, 5648 (1993). Density-Functional Thermochemistry. III. The Role of Exact Exchange.
92. H. Landolt and R. Börnstein, *Numerical Data and Functional Relationships in Science and Technology*, Springer, Berlin, 1982.
93. T. Koopmans, *Physica*, **1**, 104 (1934). Über die Zuordnung von Wellen Funktionen und Eigenwerten zu den Einzelnen Elektronen eines Atom.
94. A. Savin, C. J. Umrigar, and X. Gonze, *Chem. Phys. Lett.*, **288**, 391 (1998). Relationship of Kohn-Sham Eigenvalues to Excitation Energies.
95. A. I. Al-Sharif, R. Resta, and C. J. Umrigar, *Phys. Rev.*, **A57**, 2466 (1998). Evidence of Physical Reality in the Kohn-Sham Potential: The Case of Atomic Ne.
96. A. Görling and M. Levy, *Phys. Rev.*, **A50**, 196 (1994). Exact Kohn-Sham Scheme Based on Perturbation-Theory.
97. A. Görling and M. Levy, *Int. J. Quantum Chem. Symp.*, **29**, 93 (1995). DFT Ionization Formulas and a DFT Perturbation-Theory for Exchange and Correlation, through Adiabatic Connection.
98. A. D. Becke, *Phys. Rev.*, **A38**, 3098 (1988). Density-Functional Exchange-Energy Approximation with Correct Asymptotic Behavior.
99. C. Lee, W. Yang, and R. G. Parr, *Phys. Rev.*, **B37**, 785 (1988). Development of the Colle-Salvetti Correlation-Energy Formula into a Functional of the Electron Density.

100. J. D. Pack and H. J. Monkhorst, *Phys. Rev.*, **B16**, 1748 (1977). Special Points for Brillouin-zone Integration - A Reply.
101. G. Gilat and P. Raubenheimer, *Phys. Rev.*, **144**, 390 (1966). Accurate Numerical Method for Calculating Frequency-Distribution Functions in Solids.
102. G. Gilat, *J. Comput. Phys.*, **10**, 432 (1972). Analysis of Methods for Calculating Spectral Properties in Solids.
103. M. Methfessel and A. T. Paxton, *Phys. Rev.*, **B40**, 3616 (1989). High-precision Sampling for Brillouin-zone Integration in Metals.
104. R. Dovesi, *Int. J. Quantum Chem.*, **29**, 1755 (1986). On the Role of Symmetry in the Ab Initio Hartree-Fock Linear-Combination-of-Atomic-Orbitals Treatment of Periodic Systems.
105. N. W. Ashcroft and N. D. Mermin, *Solid State Physics*, Saunders College Publishing, Fort Worth, Texas, 1976.
106. M. Lax, *Symmetry Principles in Solid State and Molecular Physics*, Wiley, New York, 1974.
107. C. M. Zicovich-Wilson and R. Dovesi, *Int. J. Quantum Chem.*, **67**, 299 (1998). On the Use of Symmetry Adapted Crystalline Orbitals in SCF-LCAO Periodic Calculations. I. The Construction of the Symmetrized Orbitals.
108. C. M. Zicovich-Wilson and R. Dovesi, *Int. J. Quantum Chem.*, **67**, 311 (1998). On the Use of Symmetry-Adapted Crystalline Orbitals in SCF-LCAO Periodic Calculations. II. Implementation of the Self-Consistent-Field Scheme and Examples.
109. L. A. Curtiss, K. Raghavachari, G. W. Trucks, and J. A. Pople, *J. Chem. Phys.*, **94**, 7221 (1991). Gaussian-2 Theory for Molecular-Energies of 1st-Row and 2nd-Row Compounds.
110. M. Prencipe, A. Zupan, R. Dovesi, E. Aprà, and V. R. Saunders, *Phys. Rev.*, **B51**, 3391 (1995). Ab Initio Study of the Structural Properties of LiF, NaF, KF, LiCl, NaCl, and KCl.
111. D. R. Lide, Ed., *The Handbook of Chemistry and Physics*, 72nd edition, CRC Press, Boca Raton, Florida, 1991.
112. T. L. Hill, *An Introduction to Statistical Thermodynamics*, Addison-Wesley, Reading, Massachusetts, 1960.
113. A. Masunov and J. J. Dannenberg, *J. Phys. Chem. A*, **103**, 178 (1999). Theoretical Study of Urea. I. Monomers and Dimers.
114. E. R. Davidson and D. Feller, *Chem. Rev.*, **86**, 681 (1986). Basis Set Selection for Molecular Calculations.
115. N. R. Kestner and J. E. Combariza, in *Reviews in Computational Chemistry*, Vol. 13, K. B. Lipkowitz and D. B. Boyd, Eds., Wiley, New York, 1999, p. 99. Basis Set Superposition Errors: Theory and Practice.
116. S. F. Boys and F. Bernardi, *Mol. Phys.*, **19**, 553 (1970). The Calculation of Small Molecular Interaction by the Difference of Separate Total Energies. Some Procedures with Reduced Errors.
117. M. A. Spackman and A. S. Mitchell, *Phys. Chem. Chem. Phys.*, **3**, 1518 (2001). Basis Set Choice and Basis Set Superposition Error (BSSE) in Periodic Hartree-Fock Calculations on Molecular Crystals.
118. A. J. Thakkar, T. Koga, M. Saito, and R. E. Hoffmeyer, *Int. J. Quantum Chem. Symp.*, **27**, 343 (1993). Double and Quadruple Zeta Contracted Gaussian Basis Sets for Hydrogen through Neon.
119. R. Dovesi, M. Causà, R. Orlando, C. Roetti, and V. R. Saunders, *J. Chem. Phys.*, **92**, 7402 (1990). Ab Initio Approach to Molecular Crystals: A Periodic Hartree-Fock Study of Crystalline Urea.
120. B. Civalieri, E. Garrone, and P. Ugliengo, *J. Mol. Struct. (THEOCHEM)*, **419**, 227 (1997). Density Functional Study of Hydrogen-Bonded Systems: Energetic and Vibrational Features of Some Gas-Phase Adducts of Hydrogen Fluoride.
121. J. F. Dobson, K. McLennan, A. Rubio, J. Wang, T. Gould, H. M. Le, and B. P. Dinte, *Aust. J. Chem.*, **54**, 513 (2001). Prediction of Dispersion Forces: Is There a Problem?

122. L. Ojamäe, K. Hermansson, C. Pisani, M. Causà, and C. Roetti, *J. Chem. Phys.*, **100**, 2128 (1994). Mechanical and Molecular Properties of Ice VIII from Crystal-Orbital Ab Initio Hartree-Fock Calculations.
123. B. Silvi, A. Beltrán, and J. Andrés, *J. Mol. Struct.*, **436-437**, 443 (1997). Periodic Hartree-Fock Calculation of the A_{1g} (T_z) and E_g (T_x , T_y) Phonon Modes in Ice VIII.
124. C. Pisani, S. Casassa, and P. Ugliengo, *Chem. Phys. Lett.*, **253**, 201 (1996). Proton-Ordered Ice Structures at Zero Pressure: A Quantum-Mechanical Investigation.
125. P. Zapol, L. A. Curtiss, and A. Erdemir, *J. Chem. Phys.*, **113**, 3338 (2000). Periodic Ab Initio Calculations of Orthoboric Acid.
126. M. Milanesio, R. Bianchi, P. Ugliengo, C. Roetti, and D. Viterbo, *J. Mol. Struct. (THEOCHEM)*, **419**, 139 (1997). Vitamin C at 120 K: Experimental and Theoretical Study of the Charge Density.
127. S. Camus, K. D. M. Harris, and R. L. Johnson, *Chem. Phys. Lett.*, **276**, 186 (1997). Ab Initio Calculation of H-2 Quadrupole Coupling Constants in Molecular Crystals: Application to Polymorphs of Oxalic Acid Dihydrate.
128. G. L. Cárdenas-Jirón, A. Masunov, and J. J. Dannenberg, *J. Phys. Chem. A*, **103**, 7042 (1999). Molecular Orbital Study of Crystalline *p*-Benzoquinone.
129. I. Petrovic, A. Navrotsky, M. E. Davis, and S. I. Zones, *Chem. Mater.*, **5**, 1805 (1993). Thermochemical Study of the Stability of Frameworks in High-Silica Zeolites.
130. I. Petrovic, P. J. Heaney, and A. Navrotsky, *Phys. Chem. Miner.*, **23**, 119 (1996). Thermochemistry of the New Silica Polymorph Moganite.
131. S. K. Saxena, N. Chatterjee, Y. Fei, and G. Shen, *Thermodynamic Data on Oxides and Silicates*, Springer, Berlin, 1993.
132. P. M. Piccione, C. Laberty, S. Y. Yang, M. A. Camblor, A. Navrotsky, and M. E. Davis, *J. Phys. Chem. B*, **104**, 10001 (2000). Thermochemistry of Pure-Silica Zeolites.
133. B. Civalieri, C. M. Zicovich-Wilson, P. Ugliengo, V. R. Saunders, and R. Dovesi, *Chem. Phys. Lett.*, **292**, 394 (1998). A Periodic Ab-Initio Study of the Structure and Relative Stability of Silica Polymorphs.
134. M. Catti, B. Civalieri, and P. Ugliengo, *J. Phys. Chem.*, **B104**, 7259 (2000). Structure and Energetics of SiO₂ Polymorphs by Quantum-Mechanical and Semiclassical Approaches.
135. T. Demuth, Y. Jeanvoine, J. Hafner, and J. G. Ángyán, *J. Phys.-Condens. Matter*, **11**, 3833 (1999). Polymorphism in Silica Studied in the Local Density and Generalized-Gradient Approximations.
136. K. P. Schröder and J. Sauer, *J. Phys. Chem.*, **100**, 11043 (1996). Potential Functions for Silica and Zeolite Catalysts Based on Ab Initio Calculations. 3. A Shell Model Ion Pair Potential for Silica and Aluminosilicates.
137. M. Sierka and J. Sauer, *Faraday Discuss.*, **106**, 41 (1997). Structure and Reactivity of Silica and Zeolite Catalysts by Combined Quantum Mechanics Shell-Model Potential Approach Based on DFT.
138. R. Dovesi, F. Freyria-Fava, C. Roetti, and V. R. Saunders, *Faraday Discuss.*, **106**, 173 (1997). Structural, Electronic and Magnetic Properties of KMF₃ (M = Mn, Fe, Co, Ni).
139. N. M. Harrison, V. R. Saunders, R. Dovesi, and W. C. Mackrodt, *Philos. Trans. R. Soc. Lond., Ser. A*, **356**, 75 (1998). Transition Metal Materials: A First Principles Approach to the Electronic Structure of the Insulating Phase.
140. G. Mallia, R. Orlando, M. Llunell, and R. Dovesi, in *Computational Materials Science*, Vol. 187, C. R. A. Catlow and E. Kotomin, Eds., IOS Press, Amsterdam, NATO Science Series III, 2003, p. 102. On the Performance of Various Hamiltonians in the Study of Crystalline Compounds. The Case of Open Shell Systems.
141. M. D. Towler, N. L. Allan, N. M. Harrison, V. R. Saunders, W. C. Mackrodt, and E. Aprà, *Phys. Rev.*, **B50**, 5041 (1994). Ab Initio Study of MnO and NiO.
142. M. Catti, G. Valerio, and R. Dovesi, *Phys. Rev.*, **B51**, 7441 (1995). Theoretical Study of Electronic, Magnetic, and Structural Properties of α -Fe₂O₃ (Hematite).

143. M. Catti, G. Sandrone, G. Valerio, and R. Dovesi, *J. Phys. Chem. Solids*, **57**, 1735 (1996). Electronic, Magnetic and Crystal Structure of Cr_2O_3 by Theoretical Methods.
144. A. Chartier, P. D'Arco, R. Dovesi, and V. R. Saunders, *Phys. Rev.*, **B60**, 14042 (1999). An Ab Initio Hartree-Fock Investigation of the Structural, Electronic and Magnetic Properties of Mn_3O_4 -Hausmannite.
145. G. Valerio, M. Catti, R. Dovesi, and R. Orlando, *Phys. Rev.*, **B52**, 2422 (1995). Ab Initio Study of Antiferromagnetic Rutile-Type FeF_2 .
146. I. d. P. R. Moreira, R. Dovesi, C. Roetti, V. R. Saunders, and R. Orlando, *Phys. Rev.*, **B72**, 7816 (2000). Ab Initio Study of MF_2 ($M = \text{Mn, Fe, Co, Ni}$) Rutile-Type Compounds Using the Periodic UHF Approach.
147. P. Reinhardt, I. d. P. R. Moreira, R. Dovesi, C. de Graaf, and F. Illas, *Chem. Phys. Lett.*, **319**, 625 (2000). Detailed Ab-Initio Analysis of the Magnetic Coupling in CuF_2 .
148. I. d. P. R. Moreira and R. Dovesi, *Phys. Rev.*, **B67**, 134513 (2003). Ab Initio Periodic Approach to Electronic Structure and Magnetic Exchange in $\text{A}_2\text{CuO}_2\text{X}_2$ ($A = \text{Ca, Sr}$ and $X = \text{F, Cl}$) High- T_c Superconductor Parent Compounds.
149. L. J. De Jong and R. Block, *Physica B*, **79**, 568 (1975). On the Exchange Interactions in Some 3D-Metal Ionic Compounds.
150. O. Kahn, *Molecular Magnetism*, VCH, New York, 1993.
151. K. Yosida, *Theory of Magnetism*, Springer, Heidelberg, Germany, 1996.
152. B. Civalleri, A. M. Ferrari, M. Lluell, R. Orlando, M. Merawa, and P. Ugliengo, *Chem. Mater.*, **15**, 3996 (2003). Cation Selectivity in Alkali-Exchanged Chabazite: an Ab-Initio Periodic Study.
153. M. P. Habas, R. Dovesi, and A. Lichanot, *J. Phys.-Condens. Matter*, **10**, 6897 (1998). B1-B2 Phase Transition in Alkaline-earth Oxides: A Comparison of Ab Initio Hartree-Fock and Density Functional Calculations.
154. P. Richet, H. K. Mao, and P. M. Bell, *J. Geophys. Res.*, **93**, 15279 (1986). Static Compression and Equation of State of CaO to 1.35 Mbar.
155. R. Jeanloz, H. K. Ahrens, H. K. Mao, and P. M. Bell, *Science*, **206**, 829 (1979). B1-B2 Transition in Calcium Oxide from Shock-Wave and Diamond-Cell Experiments.
156. J. F. Mammone, H. K. Mao, and P. M. Bell, *Geophys. Res. Lett.*, **8**, 140 (1981). Equation of State of CaO Under Static Pressure Conditions.
157. J. Muscat, V. Swamy, and N. M. Harrison, *Phys. Rev.*, **B65**, 224112 (2002). First-Principles Calculations of the Phase Stability of TiO_2 .
158. L. S. Dubrovinsky, N. A. Dubrovinskaia, V. Swamy, J. Muscat, N. M. Harrison, R. Ahuja, B. Holm, and B. Johansson, *Nature*, **410**, 653 (2001). Cotunnite-Structured Titanium Dioxide: The Hardest Known Oxide.
159. J. F. Nye, *Physical Properties of Crystals*, Oxford University Press, London, 1957.
160. M. Born and J. R. Oppenheimer, *Ann. Phys. (Leipzig)*, **84**, 457 (1927). On the Quantum Theory of Molecules.
161. P. Giannozzi, S. de Gironcoli, P. Pavone, and S. Baroni, *Phys. Rev.*, **B43**, 7231 (1991). Ab Initio Calculation of Phonon Dispersions in Semiconductors.
162. S. Baroni, S. de Gironcoli, A. Dal Corso, and P. Giannozzi, *Rev. Mod. Phys.*, **73**, 515 (2001). Phonons and Related Crystal Properties from Density-Functional Perturbation Theory.
163. X. Gonze, J-M. Beuken, R. Caracas, F. Detraux, M. Fuchs, G-M. Rignanese, L. Sindic, M. Verstraete, G. Zerah, F. Jollet, M. Torrent, A. Roy, M. Mikami, P. Ghosez, J-Y. Raty, and D. C. Allan, *Computational Materials Science*, **25**, 478 (2002). First-Principles Computation of Material Properties: The ABINIT Software Project.
164. S. Y. Savrasov, *Phys. Rev.*, **B54**, 16470 (1996). Linear-Response Theory and Lattice Dynamics: A Muffin-Tin-Orbital Approach.

165. F. Pascale, C. M. Zicovich-Wilson, F. Lopez Gejo, B. Civalleri, R. Orlando, and R. Dovesi, *J. Comput. Chem.*, **25**, 888 (2004). The Calculation of the Vibrational Frequencies of the Crystalline Compounds and Its Implementation in the CRYSTAL Code.
166. X. Gonze, D. C. Allan, and M. P. Teter, *Phys. Rev. Lett.*, **68**, 3603 (1992). Interatomic Force-Constants from First Principles - The Case of Alpha-Quartz.
167. F. Gervais and B. Piriou, *Phys. Rev.*, **B11**, 3944 (1975). Temperature Dependence of Transverse and Longitudinal Optic Modes in the *alpha* and *beta* Phases of Quartz.
168. R. A. Evarestov and A. V. Bandura, *Int. J. Quantum Chem.*, **96**, 282 (2004). Hartree-Fock Calculations of Electronic Structure of (110)-Surface of Rutile TiO₂: Comparison of Single (2D) and Periodic (3D) Slab Models.
169. P. W. Tasker, *J. Phys. C*, **12**, 4977 (1979). The Stability of Ionic Crystal Surfaces.
170. S. Casassa, P. Ugliengo, and C. Pisani, *J. Chem. Phys.*, **106**, 8030 (1997). Proton-Ordered Models of Ordinary Ice for Quantum-Mechanical Studies.
171. K. Doll, N. M. Harrison, and V. R. Saunders, *J. Phys.-Condens. Matter*, **11**, 5007 (1999). A Density Functional Study of Lithium Bulk and Surfaces.
172. M. Causà, R. Dovesi, E. Kotomin, and C. Pisani, *J. Phys. C*, **20**, 4983 (1987). MgO (110) Surface and CO Adsorption Thereon. I. Clean (110) Surface.
173. L. G. M. Pettersson, M. Nyberg, J.-L. Pascual, and M. A. Nygren, in *Chemisorption and Reactivity on Supported Clusters and Thin Films*, Vol. 331, G. Pacchioni and R. M. Lambert, Eds., Kluwer Academic Press, Dordrecht, the Netherlands, 1997, p. 425. Theoretical Modeling of Chemisorption and Reactions at Metal-Oxide Surfaces.
174. P. W. Tasker, *Adv. Ceram.*, **10**, 176 (1984). Surface of Magnesia and Alumina.
175. G. Mallia, PhD thesis, Università di Torino, Torino, Italy, 2002.
176. W. C. Mackrodt, *Philos. Trans. R. Soc. Lond., Ser. A*, **341**, 301 (1992). Classical and Quantum Simulation of the Surface Properties of α -Al₂O₃.
177. A. D'Ercole, A. M. Ferrari, and C. Pisani, *J. Chem. Phys.*, **115**, 509 (2001). On the Role of Electrostatics in the Heterolytic Splitting of Covalent Bonds at Defective Oxide Surfaces.
178. M. Causà, R. Dovesi, and F. Ricca, *Surf. Sci.*, **280**, 1 (1993). Regular Adsorption of CO Molecules on LiF (001).
179. K. Hermansson and M. Alfredsson, *Surf. Sci.*, **411**, 23 (1998). N₂ and HF Vibrations on LiF(001): the Effect of Surface Coverage.
180. D. P. Taylor, W. P. Hess, and M. I. McCarthy, *J. Phys. Chem. B*, **101**, 7455 (1997). Structure and Energetics of the Water/NaCl(100) Interface.
181. A. V. Puchina, V. E. Puchin, M. Huisinga, R. Bennewitz, and M. Reichling, *Surf. Sci.*, **404**, 687 (1998). Theoretical Modelling of Steps and Surface Oxidation on CaF₂(111).
182. V. E. Puchin, A. V. Puchina, M. Huisinga, and M. Reichling, *J. Phys.-Condens. Matter*, **13**, 2081 (2001). Theoretical Modelling of Steps on the CaF₂(111) Surface.
183. C. Pisani, M. Causà, R. Dovesi, and C. Roetti, *Prog. Surf. Sci.*, **25**, 119 (1987). Hartree-Fock Ab Initio Characterization of Ionic Crystal Surfaces with a Slab Model. The (0001) Face of α -Al₂O₃.
184. M. Causà, R. Dovesi, C. Pisani, and C. Roetti, *Surf. Sci.*, **215**, 259 (1988). Ab Initio Characterization of the (0001) and (10-10) Crystal Faces of α -Alumina.
185. V. E. Puchin, J. D. Gale, A. L. Shluger, E. A. Kotomin, J. Gunster, M. Brause, and V. Kempter, *Surf. Sci.*, **370**, 190 (1997). Atomic and Electronic Structure of the Corundum (0001) Surface: Comparison with Surface Spectroscopies.
186. A. Wander, B. Searle, and N. M. Harrison, *Surf. Sci.*, **458**, 25 (2000). An Ab Initio Study of α -Al₂O₃ (0001): the Effects of Exchange and Correlation Functionals.
187. S. Gennard, F. Corà, and C. R. A. Catlow, *J. Phys. Chem. B*, **103**, 10158 (1999). Comparison of the Bulk and Surface Properties of Ceria and Zirconia by Ab Initio Investigations.
188. C. Rehbein, F. Michel, N. M. Harrison, and A. Wander, *Surf. Rev. Lett.*, **5**, 337 (1998). Ab Initio Total Energy Studies of the Alpha-Cr₂O₃ (0001) and (01-1)2 Surfaces.

189. T. Ouazzani, A. Lichanot, and C. Pisani, *J. Phys. Chem. Solids*, **56**, 915 (1995). Effect of the Quality of the Atomic Orbitals Basis Set about the Relaxation and Electronic Structure of the (110) Surface of Lithium Oxide.
190. M. Causà, R. Dovesi, C. Pisani, and C. Roetti, *Surf. Sci.*, **175**, 551 (1986). Ab initio Hartree-Fock Study of the MgO (001) Surface.
191. F. R. Sensato, R. Custodio, M. Calatayud, A. Beltrán, J. Andrés, J. R. Sambrano, and E. Longo, *Surf. Sci.*, **511**, 408 (2002). Periodic Study on the Structural and Electronic Properties of Bulk, Oxidized and Reduced SnO₂ (110) Surfaces and the Interaction with O²⁻.
192. J. Muscat, N. M. Harrison, and G. Thornton, *Phys. Rev.*, **B59**, 2320 (1999). Effects of Exchange, Correlation, and Numerical Approximations on the Computed Properties of the Rutile TiO₂ (100) Surface.
193. J. Muscat and N. M. Harrison, *Surf. Sci.*, **446**, 119 (2000). The Physical and Electronic Structure of the Rutile (001) Surface.
194. A. Wander and N. M. Harrison, *Surf. Sci.*, **457**, L342 (2000). Ab Initio Study of ZnO (10-10).
195. A. Wander and N. M. Harrison, *Surf. Sci.*, **468**, L851 (2000). Ab initio study of ZnO (11-20).
196. A. Beltrán, J. Andrés, M. Calatayud, and J. B. L. Martins, *Chem. Phys. Lett.*, **338**, 224 (2001). Theoretical Study of ZnO (10-10) and Cu/ZnO (10-10) Surfaces.
197. T. Ouazzani, A. Lichanot, C. Pisani, and C. Roetti, *J. Phys. Chem. Solids*, **54**, 1603 (1993). Relaxation and Electronic Structure of Surfaces in Lithium Sulphide: a Hartree-Fock Ab Initio Approach.
198. K. M. Rosso, U. Becker, and M. F. Hochella, *Am. Mineral.*, **84**, 1535 (1999). Atomically Resolved Electronic Structure of Pyrite (100) Surfaces: An Experimental and Theoretical Investigation with Implications for Reactivity.
199. J. Muscat and J. D. Gale, *Geochim. Cosmochim. Acta*, **67**, 799 (2003). First Principle Studies of the Surface of Galena PbS.
200. F. Frechard and P. Sautet, *Surf. Sci.*, **336**, 146 (1995). Hartree-Fock Ab-Initio Study of the Geometric and Electronic Structure of RuS₂ and its (100) and (111) Surfaces.
201. K. Doll and N. M. Harrison, *Chem. Phys. Lett.*, **317**, 282 (2000). Chlorine Adsorption on the Cu (111) Surface.
202. K. Doll, *Eur. Phys. J. B*, **22**, 389 (2001). Density Functional Study of the Adsorption of K on the Cu (111) Surface.
203. K. Doll and N. M. Harrison, *Phys. Rev.*, **B63**, 165410 (2001). Theoretical Study of Chlorine Adsorption on the Ag(111) Surface.
204. K. Doll, *Phys. Rev.*, **B66**, 155421 (2002). Density-Functional Study of the Adsorption of K on the Ag (111) Surface.
205. K. Doll, *Surf. Sci.*, **544**, 103 (2003). Density Functional Study of Ni Bulk, Surfaces and the Adsorbate Systems Ni (111)($\sqrt{3} \times \sqrt{3}$)R30 degrees-Cl, and Ni (111)(2 × 2)-K.
206. A. Kokalj and M. Causà, *J. Phys.-Condens. Matter*, **11**, 7463 (1999). Periodic Density Functional Theory Study of Pt (111): Surface Features of Slabs of Different Thickness.
207. L. Fu, E. Yaschenko, L. Resca, and R. Resta, *Phys. Rev.*, **B60**, 2697 (1999). Hartree-Fock Studies of Surface Properties of BaTiO₃.
208. R. A. Evarestov, E. Kotomin, E. Heifets, J. Maier, and G. Borstel, *Sol. St. Commun.*, **127**, 367 (2003). Ab Initio Hartree-Fock Calculations of LaMnO₃ (110) Surfaces.
209. E. Heifets, R. I. Eglitis, E. A. Kotomin, J. Maier, and G. Borstel, *Phys. Rev.*, **B64**, 235417 (2001). Ab Initio Modeling of Surface Structure for SrTiO₃ Perovskite.
210. E. Heifets, R. I. Eglitis, E. A. Kotomin, J. Maier, and G. Borstel, *Surf. Sci.*, **513**, 211 (2002). First-Principles Calculations for SrTiO₃ Surface Structure.
211. G. Bussolin, S. Casassa, C. Pisani, and P. Ugliengo, *J. Chem. Phys.*, **108**, 9516 (1998). Ab Initio of HCl and HF Interaction with Crystalline Ice. I. Physical Adsorption.

212. B. Civalleri, S. Casassa, E. Garrone, C. Pisani, and P. Ugliengo, *J. Phys. Chem. B*, **103**, 2165 (1999). Quantum Mechanical Ab Initio Characterization of a Simple Periodic Model of the Silica Surface.
213. A. Damin, R. Dovesi, A. Zecchina, and P. Ugliengo, *Surf. Sci.*, **479**, 253 (2001). CO/MgO (001) at Different CO Coverages: A Periodic Ab Initio Hartree-Fock and B3-LYP Study.
214. R. Wichtendahl, M. Rodriguez-Rodrigo, U. Härtel, H. Kuhlenbeck, and H. J. Freund, *Phys. Status Solidi A*, **173**, 93 (1999). Thermodesorption of CO and NO from Vacuum-Cleaved NiO (100) and MgO (100).
215. R. Wichtendahl, M. Rodriguez-Rodrigo, U. Härtel, H. Kuhlenbeck, and H. J. Freund, *Surf. Sci.*, **423**, 90 (1999). TDS Study of the Bonding of CO and NO to Vacuum-Cleaved NiO (100).
216. P. Ugliengo and A. Damin, *Chem. Phys. Lett.*, **366**, 683 (2002). Are Dispersive Forces Relevant for CO Adsorption on the MgO (001) Surface?
217. J. F. Sanz and C. M. Zicovich-Wilson, *Chem. Phys. Lett.*, **303**, 111 (1999). A Periodic Hartree-Fock Study of Na Adsorption on the TiO₂ (110) Rutile Surface.
218. J. Muscat and N. M. Harrison, *Phys. Rev.*, **B59**, 15457 (1999). First-Principles Study of Potassium Adsorption on TiO₂ Surfaces.
219. L. Giordano, G. Pacchioni, T. Bredow, and J. F. Sanz, *Surf. Sci.*, **471**, 21 (2001). Cu, Ag, and Au Atoms Adsorbed on TiO₂ (110): Cluster and Periodic Calculations.
220. M. Calatayud, J. Andrés, and A. Beltrán, *Surf. Sci.*, **430**, 213 (1999). A Theoretical Analysis of Adsorption and Dissociation of CH₃OH on the Stoichiometric SnO₂ Surface.
221. M. Melle-Franco and G. Pacchioni, *Surf. Sci.*, **461**, 54 (2000). CO Adsorption on the SnO₂ (110): Cluster and Periodic Ab Initio Calculations.
222. M. Melle-Franco, G. Pacchioni, and A. V. Chadwick, *Surf. Sci.*, **478**, 25 (2001). Cluster and Periodic Ab Initio Calculations on the Adsorption of CO₂ on the SnO₂ (110) Surface.
223. T. Bredow and G. Pacchioni, *Surf. Sci.*, **373**, 21 (1997). Comparative Periodic and Cluster Ab Initio Study on Cu₂O (111)/CO.
224. P. Persson and L. Ojamäe, *Chem. Phys. Lett.*, **321**, 302 (2000). Periodic Hartree-Fock Study of the Adsorption of Formic Acid on ZnO (10-10).
225. A. Wander and N. M. Harrison, *J. Phys. Chem. B*, **105**, 6191 (2001). Ab Initio Study of Hydrogen Adsorption on ZnO (10-10).
226. K. M. Rosso, U. Becker, and M. F. Hochella, *Am. Mineral.*, **84**, 1549 (1999). The Interaction of Pyrite (100) Surfaces with O₂ and H₂O: Fundamental Oxidation Mechanisms.
227. B. Civalleri and P. Ugliengo, *J. Phys. Chem. B*, **104**, 9491 (2000). First Principle Calculations of the Adsorption of NH₃ on a Periodic Model of Silica Surface.
228. J. R. B. Gomes, F. Illas, N. Cruz Hernandez, J. F. Sanz, A. Wander, and N. M. Harrison, *J. Chem. Phys.*, **116**, 1684 (2002). Surface Model and Exchange-Correlation Functional Effects on the Description of Pd/ α -Al₂O₃ (0001).
229. M. Sgroi, C. Pisani, and M. Busso, *Thin Solid Films*, **400**, 64 (2001). Ab Initio Density Functional Simulation of Structural and Electronic Properties of MgO Ultra-Thin Adlayers on the (001) Ag Surface.
230. C. Giovanardi, A. di Bona, T. S. Moia, S. Valeri, C. Pisani, M. Sgroi, and M. Busso, *Surf. Sci. Lett.*, **505**, L209 (2002). Experimental and Theoretical Study of the MgO/Ag (001) Interface.
231. E. Heifets, E. A. Kotomin, and R. Orlando, *J. Phys.-Condens. Matter*, **8**, 6577 (1996). Periodic Hartree-Fock Simulation of the Ag/MgO Interface Structure.
232. E. Heifets, Y. F. Zhukovskii, E. A. Kotomin, and M. Causà, *Chem. Phys. Lett.*, **238**, 395 (1998). The Adhesion Nature of the Ag/MgO (100) Interface: An Ab Initio Study.
233. Y. F. Zhukovskii, E. A. Kotomin, P. W. M. Jacobs, A. M. Stoneham, and J. H. Harding, *Surf. Sci.*, **441**, 373 (1999). Comparative Theoretical Study of the Ag-MgO (100) and (110) Interfaces.

234. Y. F. Zhukovskii, E. A. Kotomin, D. Fuks, S. Dorfman, and A. Gordon, *Surf. Sci.*, **482**, 66 (2001). Hartree-Fock Study of Adhesion and Charge Redistribution on the Ag/MgO (001) Interface.
235. E. Kotomin, J. Maier, Y. F. Zhukovskii, D. Fuks, and S. Dorfman, *Mater. Sci. Eng. C*, **23**, 247 (2003). Ab Initio Modelling of Silver Adhesion on the Corundum (0001) Surface.
236. S. Casassa, A. M. Ferrari, M. Busso, and C. Pisani, *J. Phys. Chem. B*, **106**, 12978 (2002). Structural, Electronic and Magnetic Properties of the NiO Monolayer Epitaxially Grown on the (001) Ag Surface: an Ab-Initio Density Functional Study.
237. M. D. Towler, N. M. Harrison, and M. I. McCarthy, *Phys. Rev.*, **B52**, 5375 (1995). Ab Initio Study of the Surface and Interfacial Properties of a Layered MgO/NiO Film.
238. W. C. Mackrodt, C. Noguera, and N. L. Allan, *Faraday Discuss.*, **114**, 105 (1999). A Study of the Electronic, Magnetic, Structural and Dynamic Properties of Low-Dimensional NiO on MgO (100) Surfaces.
239. B. Henderson, *Defects in Crystalline Solids*, Arnold, London, 1972.
240. W. Haynes and A. M. Stoneham, *Defects and Defect Processes in Non Metallic Solids*, Wiley, New York, 1984.
241. G. Pacchioni, P. S. Bagus, and F. Parmigiani, Eds., *Cluster Models for Surface and Bulk Phenomena*, Vol. 283, Plenum Press, New York, 1992.
242. F. Maseras and K. Morokuma, *J. Comput. Chem.*, **16**, 1170 (1995). IMOMM: A New Integrated Ab Initio + Molecular Mechanics Geometry Optimization Scheme of Equilibrium Structures and Transition States.
243. S. Dapprich, I. Komáromi, K. S. Byun, K. Morokuma, and M. J. Frisch, *J. Mol. Struct. (THEOCHEM)*, **462**, 1 (1999). A New ONIOM Implementation in Gaussian98. Part I. The Calculation of Energies, Gradients, Vibrational Frequencies and Electric Field Derivatives.
244. T. Vreven and K. Morokuma, *J. Comput. Chem.*, **21**, 1419 (2000). On the Application of the IMOMO (Integrated Molecular Orbital Plus Molecular Orbital) Method.
245. U. Eichler, C. M. Kölmel, and J. Sauer, *J. Comput. Chem.*, **18**, 463 (1997). Combining Ab-Initio Techniques with Analytical Potential Functions for Structure Predictions of Large Systems: Method and Applications to Crystalline Silica Polymorphs.
246. J. R. Shoemaker, L. W. Burggraf, and M. S. Gordon, *J. Phys. Chem. A*, **103**, 3245 (1999). SIMOMM: An Integrated Molecular Orbital / Molecular Mechanics Optimization Scheme for Surfaces.
247. C. Pisani, R. Dovesi, C. Roetti, M. Causà, R. Orlando, S. Casassa, and V. R. Saunders, *Int. J. Quantum Chem.*, **77**, 1032 (2000). CRYSTAL and EMBED, Two Computational Tools for the Ab Initio Study of the Electronic Properties of Crystals.
248. C. Pisani, *J. Mol. Struct. (THEOCHEM)*, **621**, 141 (2003). Local Techniques for the Ab-Initio Quantum Mechanical Treatment of the Chemical Properties of Crystalline Materials.
249. C. Pisani, in *Handbook of Molecular Physics and Quantum Chemistry*, Vol. 3, S. Wilson, Ed., Wiley: Chichester, United Kingdom, 2003, p. 339. Molecules at Crystalline Surfaces and in Crystal Cages.
250. M. Leslie and M. J. Gillan, *J. Phys. C*, **18**, 973 (1985). The Energy and Elastic Dipole Tensor of Defects in Ionic Crystals Calculated by the Supercell Method.
251. G. Makov and M. C. Payne, *Phys. Rev.*, **B51**, 4014 (1995). Periodic Boundary-Conditions in Ab-Initio Calculations.
252. U. Gerstmann, P. Deák, R. Rurali, B. Aradi, T. Frauenheim, and H. Overhof, *Phys. Rev. Lett.*, submitted (2004). Accurate Treatment of Charged Defects within Periodic Boundary Conditions.
253. G. Mallia, R. Orlando, C. Roetti, P. Ugliengo, and R. Dovesi, *Phys. Rev.*, **B63**, 235102 (2001). F Center in LiF: A Quantum Mechanical Ab Initio Investigation of the Hyperfine Interaction Between the Unpaired Electron and the Vacancy and its First Seven Neighbors.
254. H. Seidel and H. C. Wolf, *The Physics of Colour Centers*, Fowler, New York, 1968.

255. W. C. Holton and H. Blum, *Phys. Rev.*, **125**, 89 (1962). Paramagnetic Resonance of F Centers in Alkali Halides.
256. A. Lichanot, C. Larrieu, R. Orlando, and R. Dovesi, *J. Phys. Chem. Solids*, **59**, 7 (1998). Lithium Trapped-Hole Centre in Magnesium Oxide. An Ab-Initio Supercell Study.
257. A. Lichanot, C. Larrieu, C. M. Zicovich-Wilson, C. Roetti, R. Orlando, and R. Dovesi, *J. Phys. Chem. Solids*, **59**, 1119 (1998). Trapped-Hole Centres Containing Lithium and Sodium in MgO, CaO and SrO. An Ab Initio Supercell Study.
258. A. Lichanot, R. Orlando, G. Mallia, M. Merawa, and R. Dovesi, *Chem. Phys. Lett.*, **318**, 240 (2000). V_{OH} Center in Magnesium Oxide: An Ab Initio Supercell Study.
259. A. Lichanot, P. Baranek, M. Merawa, R. Orlando, and R. Dovesi, *Phys. Rev.*, **B62**, 12812 (2000). V_{OH} and V_{OD} Centers in Alkaline-Earth Oxides: An Ab Initio Supercell Study.
260. M. M. Abraham, W. P. Unruh, and Y. Chen, *Phys. Rev.*, **B10**, 3540 (1974). Electron-Nuclear-Double-Resonance Investigations of $[Li]^0$ and $[Na]^0$ Centers in MgO, CaO, and SrO.
261. Y. Chen and M. M. Abraham, *J. Phys. Chem. Solids*, **51**, 747 (1990). Trapped-Hole Centers in Alkaline-Earth Oxides.
262. O. F. Schirmer, *J. Phys. Chem. Solids*, **29**, 1407 (1968). The Structure of the Paramagnetic Lithium Center in Zinc Oxide and Beryllium Oxide.
263. R. Orlando, R. Dovesi, P. Azavant, N. M. Harrison, and V. R. Saunders, *J. Phys.-Condens. Matter*, **6**, 8573 (1994). A Super-Cell Approach for the Study of Localized Defects in Solids: Carbon Substitution in Bulk Silicon.
264. R. Orlando, P. Azavant, M. D. Towler, R. Dovesi, and C. Roetti, *J. Phys.-Condens. Matter*, **8**, 1123 (1996). Cluster and Supercell Calculations for Carbon-doped Silicon.
265. C. Freyria-Fava, R. Dovesi, V. R. Saunders, M. Leslie, and C. Roetti, *J. Phys.-Condens. Matter*, **5**, 4793 (1993). Ca and Be Substitution in Bulk MgO: Ab Initio Hartree-Fock and Ionic Model Supercell Calculation.
266. A. V. Puchina, V. E. Puchin, E. A. Kotomin, and M. Reichling, *Solid State Commun.*, **106**, 285 (1998). Ab Initio Study of the F Centers in CaF_2 : Calculations of the Optical Absorption, Diffusion and Binding Energies.
267. W. C. Mackrodt, *Ber. Bunsenges. Phys. Chem.*, **101**, 169 (1997). The Nature of Valence Band Holes in Pure and Fe-Doped NiO: An Ab Initio Hartree-Fock Study.
268. W. C. Mackrodt, N. M. Harrison, V. R. Saunders, N. L. Allan, and M. D. Towler, *Chem. Phys. Lett.*, **250**, 66 (1996). Direct Evidence of O(P) Holes in Li-Doped NiO from Hartree-Fock Calculations.
269. R. A. Evarestov and V. P. Smirnov, *Phys. St. Sol.*, **B215**, 949 (1999). Supercell Model of V-Doped TiO_2 : Unrestricted Hartree-Fock Calculations.
270. C. M. Zicovich-Wilson and R. Dovesi, *J. Phys. Chem.*, **102**, 1411 (1998). Titanium Containing Zeolites. A Periodic Ab-Initio Hartree Fock Characterization.
271. A. Damin, S. Bordiga, A. Zecchina, K. Doll, and C. Lamberti, *J. Chem. Phys.*, **118**, 10183 (2003). Ti-Chabazite as a Model System of Ti(IV) in Ti-Zeolites: A Periodic Approach.
272. R. Orlando, F. Corà, R. Millini, G. Perego, and R. Dovesi, *J. Chem. Phys.*, **105**, 8937 (1996). Hydrogen Abstraction from Methane by Li Doped MgO: A Periodic Quantum Mechanical Study.
273. D. M. Gruen, P. C. Redfern, D. A. Horner, P. Zapol, and L. A. Curtiss, *J. Phys. Chem. B*, **103**, 5459 (1999). Theoretical Studies on Nanocrystalline Diamond: Nucleation by Dicarbon and Electronic Structure of Planar Defects.
274. R. Orlando, R. Dovesi, C. Roetti, and V. R. Saunders, *Chem. Phys. Lett.*, **228**, 225 (1994). Convergence Properties of the Cluster Model in the Study of Local Perturbations in Ionic Systems. The Case of Bulk Defects in MgO.
275. M. D. Segall, P. J. D. Lindan, M. J. Probert, C. J. Pickard, P. J. Hasnip, S. J. Clark, and M. C. Payne, *J. Phys.-Condens. Matter*, **14**, 2717 (2002). First-Principles Simulation: Ideas, Illustrations and the CASTEP Code.

276. W. Andreoni and A. Curioni, *Parallel Computing*, **26**, 819 (2000). New Advances in Chemistry and Material Science with CPMD and Parallel Computing.
277. M. Bockstedte, A. Kley, J. Neugebauer, and M. Scheffler, *Comput. Phys. Commun.*, **107**, 187 (1997). Density-Functional Theory Calculations for Polyatomic Systems: Electronic Structure, Static and Elastic Properties and Ab Initio Molecular Dynamics.
278. B. G. Pfrommer, J. Demmel, and H. Simon, *J. Comput. Phys.*, **150**, 287 (1999). Unconstrained Energy Functionals for Electronic Structure Calculations.
279. S. Baroni, A. Dal Corso, S. de Gironcoli, and P. Giannozzi. PWSCFV.2.1, 2004. Available: <http://www.pwscf.org>.
280. G. Y. Sun, J. Kurti, P. Rajczy, M. Kertesz, J. Hafner, and G. Kresse, *J. Mol. Struct. (THEOCHEM)*, **624**, 37 (2003). Performance of the Vienna Ab Initio Simulation Package (VASP) in Chemical Applications.
281. P. E. Blöchl, C. J. Först, and J. Schimpl, *Bull. Mater. Sci.*, **26**, 33 (2003). Projector Augmented Wave Method: Ab-Initio Molecular Dynamics with Full Wave Functions.
282. A. R. Tackett, N. A. W. Holzwarth, and G. E. Matthews, *Comput. Phys. Commun.*, **135**, 329 (2001). A Projector Augmented Wave (PAW) Code for Electronic Structure Calculations, Part I: Atom paw for Generating Atom-Centered Functions.
283. A. R. Tackett, N. A. W. Holzwarth, and G. E. Matthews, *Comput. Phys. Commun.*, **135**, 348 (2001). A Projector Augmented Wave (PAW) Code for Electronic Structure Calculations, Part II: Pwpaw for Periodic Solids in a Plane Wave Basis.
284. G. Lippert, J. Hutter, and M. Parrinello, *Mol. Phys.*, **92**, 477 (1997). A Hybrid Gaussian and Plane Wave Density Functional Scheme.
285. J. M. Soler, E. Artacho, J. D. Gale, A. García, J. Junquera, P. Ordejón, and D. Sánchez-Portal, *J. Phys.-Condens. Matter*, **14**, 2745 (2002). The Siesta Method for Ab Initio Order-N Materials Simulation.
286. B. Delley, *J. Chem. Phys.*, **113**, 7756 (2000). From Molecules to Solids with the DMol3 Approach.
287. G. Bihlmayer and S. Blügel, *Comput. Phys. Commun.*, in press (2005). FLEUR: a Parallelized Electronic Structure Code for Surfaces and Bulk.
288. K. Schwarz and P. Blaha, *Comput. Mat. Sci.*, **28**, 259 (2003). Solid State Calculations Using WIEN2k.
289. G. te Velde, F. M. Bickelhaupt, E. J. Baerends, C. Fonseca Guerra, S. J. A. van Gisbergen, J. G. Snijders, and T. Ziegler, *J. Comput. Chem.*, **22**, 931 (2001). Chemistry with ADF.
290. K. N. Kudin and G. E. Scuseria, *Phys. Rev.*, **B61**, 16440 (2000). Linear-Scaling Density-Functional Theory with Gaussian Orbitals and Periodic Boundary Conditions: Efficient Evaluation of Energy and Forces via the Fast Multipole Method.
291. S. Swaminathan, B. N. Craven, and R. K. McMullan, *Acta Crystallogr. Sec. B*, **40**, 300 (1984). The Crystal Structure and Molecular Thermal Motion of Urea at 12, 60 and 123 K from Neutron Diffraction.
292. I. J. Bush, *Capability Computing*, **1**, 10 (2003). CRYSTAL on HPCx: Ab Initio Study of Proteins.

